DEUTERON BREAK-UP BY PROTONS AT 100 MEV

BY

PI-JUNG PAN

DEUTERON BREAK-UP BY PROTONS AT 100 MEV

by

Pi-jung Pan

A thesis submitted to the Faculty of Graduate Studies and Research of McGill University in partial fulfilment of the requirements for the degree of Doctor of Philosophy.

Foster Radiation Laboratory,
McGill University,
Montreal.

July, 1968.

TABLE OF CONTENTS

ABSTRACT

Inelastic scattering of protons by deuterons has been investigated at 100 MeV incident proton energy. Experiments were carried out by the technique of detecting the two outgoing protons in coincidence, and energy data were collected with a two-parameter pulse-height analyzer. Attention was paid to those angular configurations of detectors where the mean energies of the undetected neutrons were small, and where final state interactions between two of the three final-state nucleons were expected. The spectator model is able to reproduce the shape and describe qualitatively those spectra which correspond to small mean neutron energies. For those spectra in which peaks due to the formation of the virtual (singlet) deuteron state were observed, predictions based on the use of the generalized density-of-states function were less successful.

ACKNOWLEDGEMENTS

It is a great pleasure to express the author's gratitude to Dr. J. E. Crawford, her research supervisor, for his constant help, encouragement, and patience throughout the whole course of the work. The guidance generously given by Dr. S. K. Mark during the two-month absence of the supervisor, and some discussions are deeply appreciated. Thanks are due to Dr. T. Y. Li for valuable discussions in computer programming.

The author would like to thank Dr. R. E. Bell and Dr. W. M. Telford for their supervision in constructing the stretcher of the McGill cyclotron pulsed-beam, and to Mr. F. Sannes for his great effort in its realization and maintenance. The author is also indebted to the staff of the Foster Radiation Laboratory machine shop and to Mr. J. Annecou for their aid in construction of the mechanical experimental set-up.

Finally the author would like to acknowledge the financial aid provided by the Shell-Canada Fellowship, and the David Stewart Memorial Fellowship, and that provided by the laboratory on behalf of the Atomic Energy Control Board of Canada during the summer months.

CHAPTER 1. INTRODUCTION

The scattering reaction between a deuteron and a nucleon has long been a subject of interest because it is the simplest reaction involving three nucleons. In the last few years new experimental techniques have made possible more detailed studies of few-nucleon systems. The three-nucleon system has received special attention; it is hoped that a more complete study of its structure, and the interactions of its components may shed more light on the behaviour of the simpler two-nucleon system. Since no free neutron target exists, our knowledge of the neutron-neutron system is scanty. Because monochromatic neutron beams of high intensity are difficult to produce, even the neutron-proton system is harder to study experimentally than the proton-proton system. Because of these difficulties, physicists have searched for alternative indirect methods. The deuteron is a simple system with its two nucleons only loosely bound to each other; one might hope that the presence of one of the two could be ignored so that the nucleon-nucleon system could be investigated through nucleon-deuteron reaction experiments.

In the past, most of the experiments done on the deuteron-nucleon system have involved only single counter measurements. The interpretation of the experimental results were difficult, because for a system with three particles in the final state the kinematic variables associated with the system cannot be completely determined by knowing only the momentum - vector of the particle detected. (See

section IV-1). Furthermore the extraction of the necessary experimental data from the background caused by both nucleon-deuteron elastic scattering, and nucleon-nucleon elastic scattering due to the impurity of the targets used in some of these experiments was painfully difficult, and estimates were then introduced (e.g. KS-60). Two parameter multichannel analyzers have only recently been available, and have been used in a few nucleon-deuteron scattering experiments. With this facility, we are able to detect two outgoing particles in coincidence and can completely determine - more exactly, over-determine - the kinematics of the nucleon-deuteron reaction, and so avoid the complications caused by elastic scattering except in a few cases.

In the theoretical work on nucleon-deuteron scattering, many approximations have been proposed. In the early stages, the modified Born approximation (GB-51, WA-48) was used, but could not reproduce spectra for 46 MeV incident proton energy. (SVR-66). Frank and Gammel (FG-54) proposed the zero-range approximation for nuclear forces and adopted the impulse approximation (C-50) to deal with the inelastic scattering. Even though it accurately predicted the reaction yield at low incident energies, the shape of the neutron energy spectra at small angles could not be reproduced by the theory (CS-59). A refined method taking into account the interaction between a pair of three final state particles (HM-58) gave the correct shape and position of part of the energy spectra observed, but gave incorrect absolute cross-sections (WA-59) for incident proton energies below 15 MeV. Komarov and Popava (KP-60) performed a calculation

of neutron spectra for the d + p $\longrightarrow$ 2p + n reaction by taking account of nuclear pair interactions, and included the interaction between the pair and the third particle by the Born approximation. This calculation reproduced the shape of the whole neutron spectrum at 0^{o} satisfactorily (VK-60).

In treating a nucleon in a deuteron as free, Kuckes et al. proposed the spectator model (KWC-61) based on the simple impulse approximation. They considered the neutron of the deuteron as an innocent bystander whose presence under some experimental conditions during the collision is negligible from kinematic considerations, and compared the results of the quasi-elastic p-p scattering with those of free p-p scattering at 145 MeV. Their results agreed well with the predictions, and an extrapolation procedure suggested by Chew and Low (CH-59) (to be described more completely in section V-1) can relate their experimental results. However other similar experiments performed at intermediate beam energies yield contradictory results. Those at 50 MeV (GK-64), and 31 MeV (BKF-65) failed to agree with the Chew-Low extrapolation procedure and the spectator model, while an experiment at 40 MeV (Ca-65) agreed with them.

In this situation we felt the need to study the D(p,2p)n reaction at 100 MeV incident proton energy in the hope of clarifying the relation between quasi-elastic p-p scattering and free p-p scattering, and to search for effects due to the final state interaction of nucleon pairs at high energy. The experiment was done by detecting the two outgoing protons by two NaI(Tl) scintillators. One of the

two counters was fixed at a chosen angle, and the other was movable in order to record spectra corresponding to different mean recoil neutron energy, and to carry out a search for final state interaction peaks. The results agreed with the Chew-Low extrapolation procedure within the experimental uncertainty. Peaks due to the formation of the virtual singlet deuteron state were observed.

CHAPTER II INSTRUMENTATION

II-1. MECHANICAL PART

II - 1a. Scattering Chamber.

A cylindrical scattering chamber (Fig. 1) was made to house two NaI(Tl) detectors and their photomultipliers. The axis of the chamber is horizontal, and the scattering plane is vertical. The proton beam enters and leaves the chamber through 2" diameter holes cut on opposite sides of the cylinder. Beam alignment is checked by means of two fluorescent screens, one in the chamber, and another in an exit screen compartment. They are viewed through lucite windows.

The detectors are mounted on opposite lids of the chamber, with each lid free to rotate to any desired angle. Angular graduations are engraved in degrees on the circumference of each lid; detectors can be located at desired angles within $\pm$ 0.2 degree. A target holder centered on one cover is a rectangular frame which slides axially in the proton beam. The fluorescent screen mentioned previously is mounted at an angle of 45^{o} at the end of the target holder.

II - 1b. Detector Assembly

(i) E detector assembly.

The two detectors used are Harshaw NaI(Tl) standard integral line scintillation crystals. Cylindrical clamps were designed to fix the photomultipliers and their detectors with respect to the lids of the chamber.

FIGURE 1

FIGURE 1

A section of the scattering chamber. There is only one of the two detector holder assemblies shown on the diagram; the detector holder assembly attached to lid 2 is not shown here.

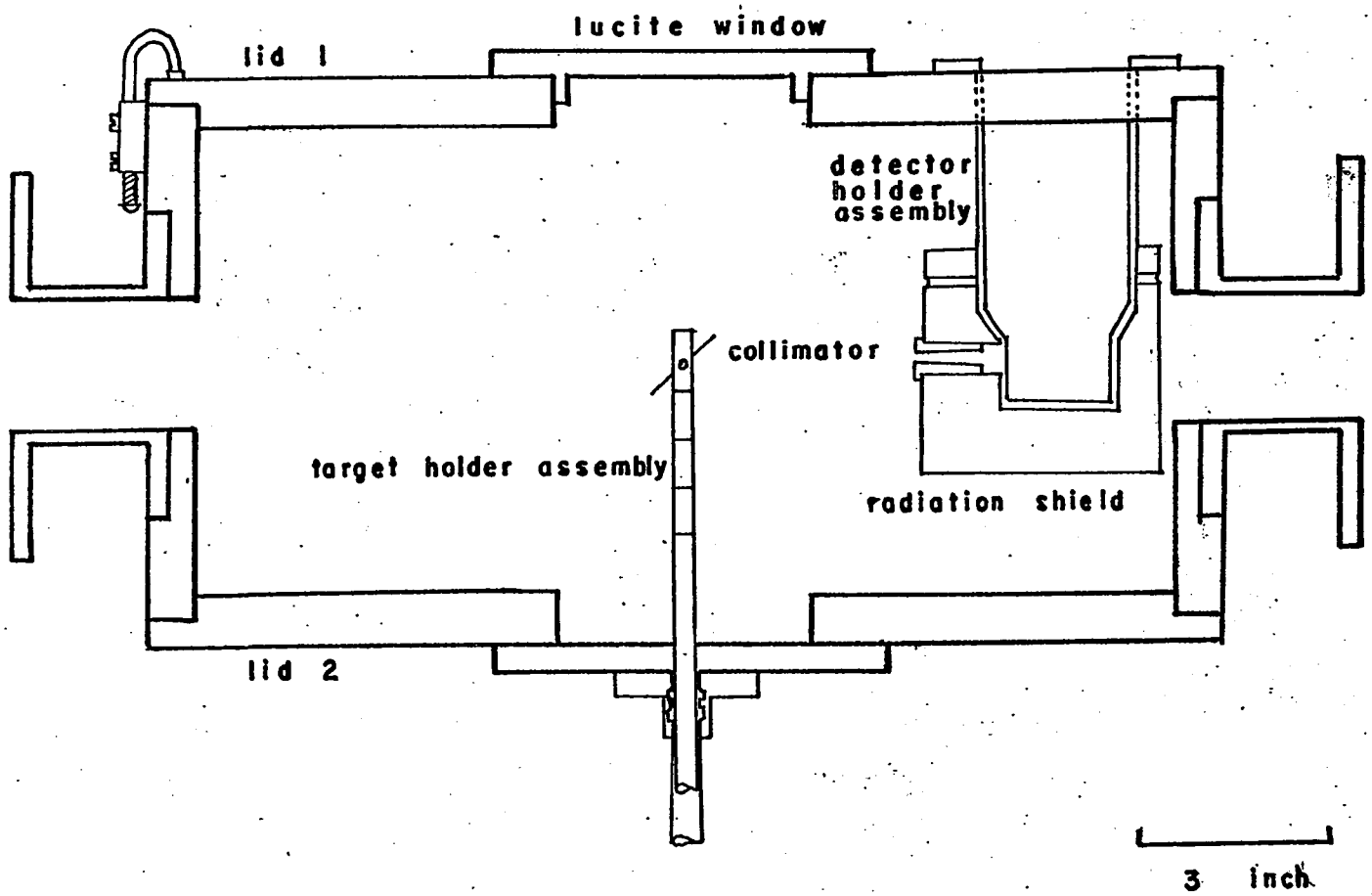
lucite window
lid 1
detector holder assembly
collimator
target holder assembly
radiation shield
lid 2
3 inch

Each detector with its photomultiplier slides into a steel can-shaped detector-holder; this holder projects into the chamber, and is bolted to the lid. At one side of the can a 0.5" diameter hole was drilled through the steel, and a circular piece of 0.003" thick copper was soft soldered on the can as an entry for protons. A well-type lead radiation shield surrounds the detector holder. A 0.5" diameter hole was drilled through the part of the lead shield which faces the copper window to provide a socket for installation of a brass collimator.

The brass collimator has a tapered hole along its axis which defines the solid angle accepted by the detector. The holes at the front ends of the collimators, i.e. the solid angle defining apertures, are 0.253" $\pm$ 0.002" in diameter. When the collimators are inserted into the sockets of the lead radiation shields in the chamber, the distances between the center of the chamber and the centers of the solid angle defining apertures were 4.0" ($\pm$ 2%). The solid angles subtended by these two collimators are then 3.34 ($\pm$ 5.6%) millisteradian, and the angular openings are 1.89 ($\pm$ 2.6%) degrees.

(ii) ΔE detector assembly.

A Simtec totally depleted silicon ΔE detector was used. This has a 100 mm^2 active area with a 200 micron depletion depth. The front and back windows have thicknesses of 75 and 125 micrograms/cm^2 respectively. The detector was used at room temperature.

A ΔE detector holder consisting of a collimator and adapting

ring was designed so that it could be mounted in front of one of the two E detectors whenever it was needed to reduce the ratio of chance to true coincidences. The front window of the detector was about 1 cm in front of the solid angle defining aperture of the collimator for the E detector.

II - 1c. Faraday Cup

Two Faraday cups were used for reaction cross-section measurements. A cup designed by W.T. Link (G-67) was the main one. Another cup was used to check the beam monitor calibration for every run. It was calibrated against the main cup by comparing proton-proton elastic scattering cross-sections obtained by use of these two cups at the same scattering angles. They agreed within 2%.

The second monitor cup was much the same as the main one in design except that it does not contain magnets. There is no entrance window, and it could be connected directly to the scattering chamber behind the exit-screen compartment. The cup was partially filled with epoxy to suppress back scattering of particles.

II - 2. ELECTRONICS

The normally pulsed cyclotron beam and its newly furnished debunched beam were used in this experiment. The electronic system described below was that used with the debunched beam. Some modifications for pulsed beam counting are also described.

II - 2a. Double Coincidence Circuit.

For studying the D(p,2p)n reaction at different pairs of detector angles, a double coincidence method was used to accumulate energy spectra. In one case a triple coincidence circuit was required. A block diagram of the electronic circuits of the double coincidence method for experiments using the debunched proton beam is shown in Fig. 2.

Energy pulses were taken from the seventh dynodes of the NaI(Tl) detectors, and sent via conventional White cathode followers to the input terminals of two identical Ortec multimode amplifiers (Model 410) in the cyclotron control room. These input signals to the amplifiers have rise-times of about 300 nanoseconds, and decay-times of about 150 microseconds. The output double-delay-line-clipped pulses from each amplifier were fed into the two sections of a dual linear gate (Sturrup Model 1450), which had been modified to reject intense pile-up spikes present in the debunched beam. A more complete description of the spike-rejecting system will be given later. The output signals from the two gates were fed into Cosmic coincidence circuit units 1 and 2 for selecting all coincident events, and they were also fed in parallel to Cosmic circuit units 3 and 4 for selecting only chance coincident events. The chance coincident output pulses were registered by a scaler, while the coincident output of units 1 and 2 were branched into two paths. One was used to turn on a second dual linear gate. Another was registered by a scaler as a check on the

FIGURE 2

FIGURE 2

Double coincidence circuitry.

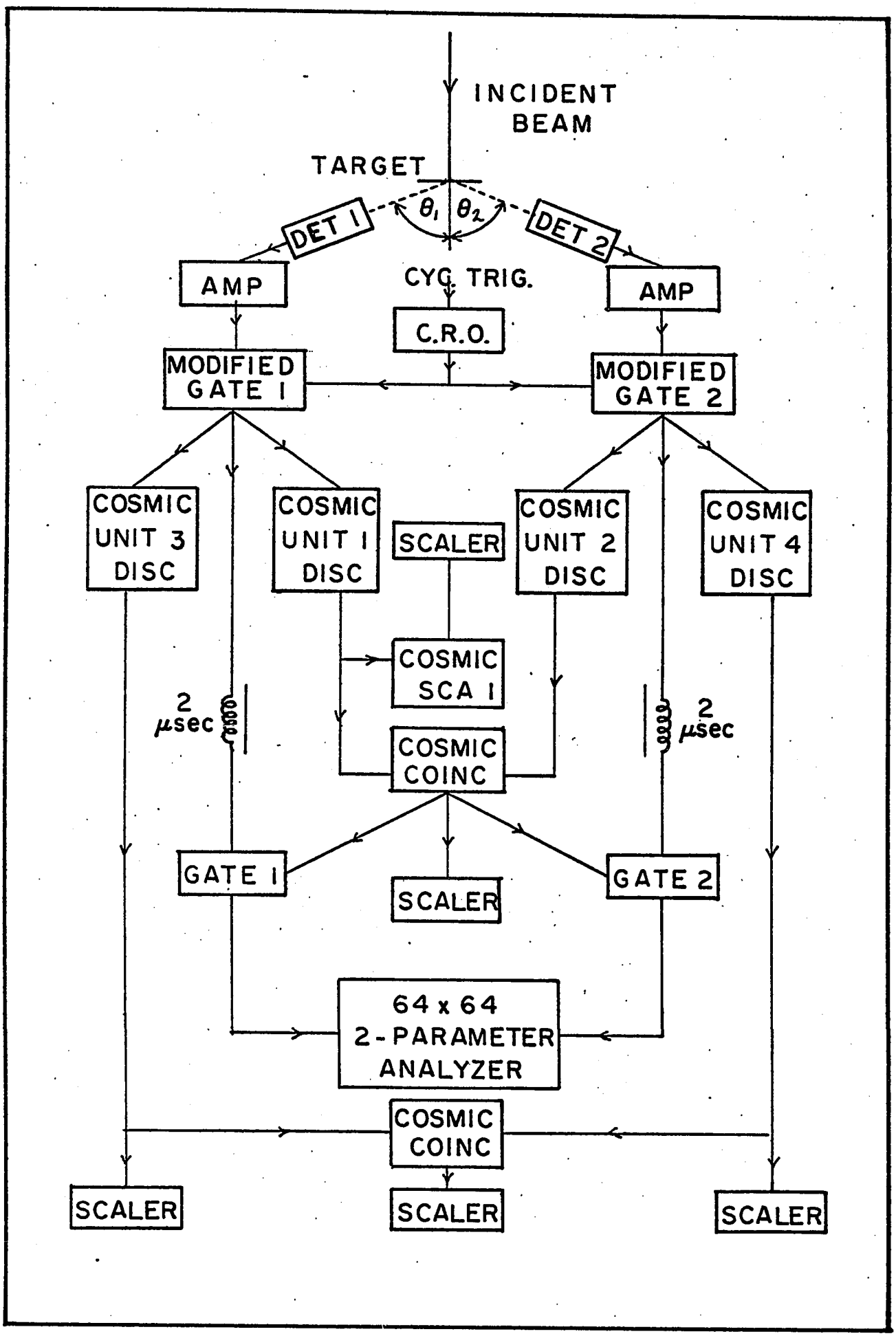
INCIDENT BEAM
TARGET
θ1
θ2
DET 1
DET 2
AMP
CYC. TRIG.
AMP
C.R.O.
MODIFIED GATE 1
MODIFIED GATE 2
COSMIC UNIT 3 DISC
COSMIC UNIT 1 DISC
SCALER
COSMIC UNIT 2 DISC
COSMIC UNIT 4 DISC
COSMIC SCA 1
2 μsec
2 μsec
COSMIC COINC
GATE 1
SCALER
GATE 2
64 x 64 2-PARAMETER ANALYZER
COSMIC COINC
SCALER
SCALER
SCALER

total number of counts stored in the pulse-height analyser mentioned below. This dual linear gate also accepted input pulses from the output of the modified dual linear gate, but after they had been delayed by about 2 microseconds to match the arrival time of the gating pulses. This gate was operated in its coincidence mode so that only coincident pulses from the two NaI detectors could pass through and be stored in a 64 x 64 channel two-parameter pulse-height analyzer. Output signals from Cosmic discriminator unit 1 were fed through its corresponding SCA into a scaler; this provided a means for monitoring beam current. The trailing edge mode of operation was used for the Cosmic coincidence units for reasons given in Chapter III.

The cyclotron beam was not perfectly debunched. Pulses could not be stored in a pulse-height analyzer during the period when the intense beam spike preceding each debunched beam burst was present. The modified linear gate accepted signals from the gating output of a type 547 oscilloscope. The gate width was controlled by the duration of the oscilloscope signals. The "Main Time Base (B)" of the oscilloscope was triggered by the ion source trigger pulse from the cyclotron trigger unit. The output gating pulse from the oscilloscope could be controlled in length and observed on the screen. Signal pulses appearing during the spike were rejected by these gates set in their "anti-coincidence" gating mode. To see the rejected portion of the beam, the pulses from a beam monitor were displayed on one input channel of the C.R.O. One could then adjust a Delay-Time Multiplier knob on

the oscilloscope to make the duration of the gate signal cover the spike of the beam monitor spectrum displayed.

II - 2b. Triple Coincidence Circuit

A block diagram of the electronic circuit for the triple coincidence method is shown in Fig. 3. It is essentially the same as that of Fig. 2 except that a ΔE detector and its associated electronics have been added.

Signals from the ΔE detector were sent through a low noise preamplifier (Tennelec Model 100) into a selectable active filter amplifier (Ortec Model 440). The pulses appearing at the 2 microsecond delay bipolar output terminal possessed almost the same pulse width ($\sim$ 1 microsecond) and roughly the same pulse-height range as those of the E pulses from the Ortec multimode amplifiers. The modified dual linear gates now accepted signals of the ΔE detector and detector E_1. Triple coincidences were obtained by feeding pulses of the ΔE detector and the E_1 and E_2 pulses into discriminators 1, 2, and 3, of the Cosmic unit. Chance coincidence pulses were selected by Cosmic units 4 and 5. The rest of the system was just the same as that shown in Fig. 2.

II - 2c. Current Integrator

The Faraday cup current was measured by a picoammeter. The voltage drop across the feedback resistors of the electrometer circuit was the input for a voltage-to-frequency converter, whose output was then scaled. Whenever the scaler overflowed, it sent out a pulse to

FIGURE 3

FIGURE 3

Triple coincidence circuitry.

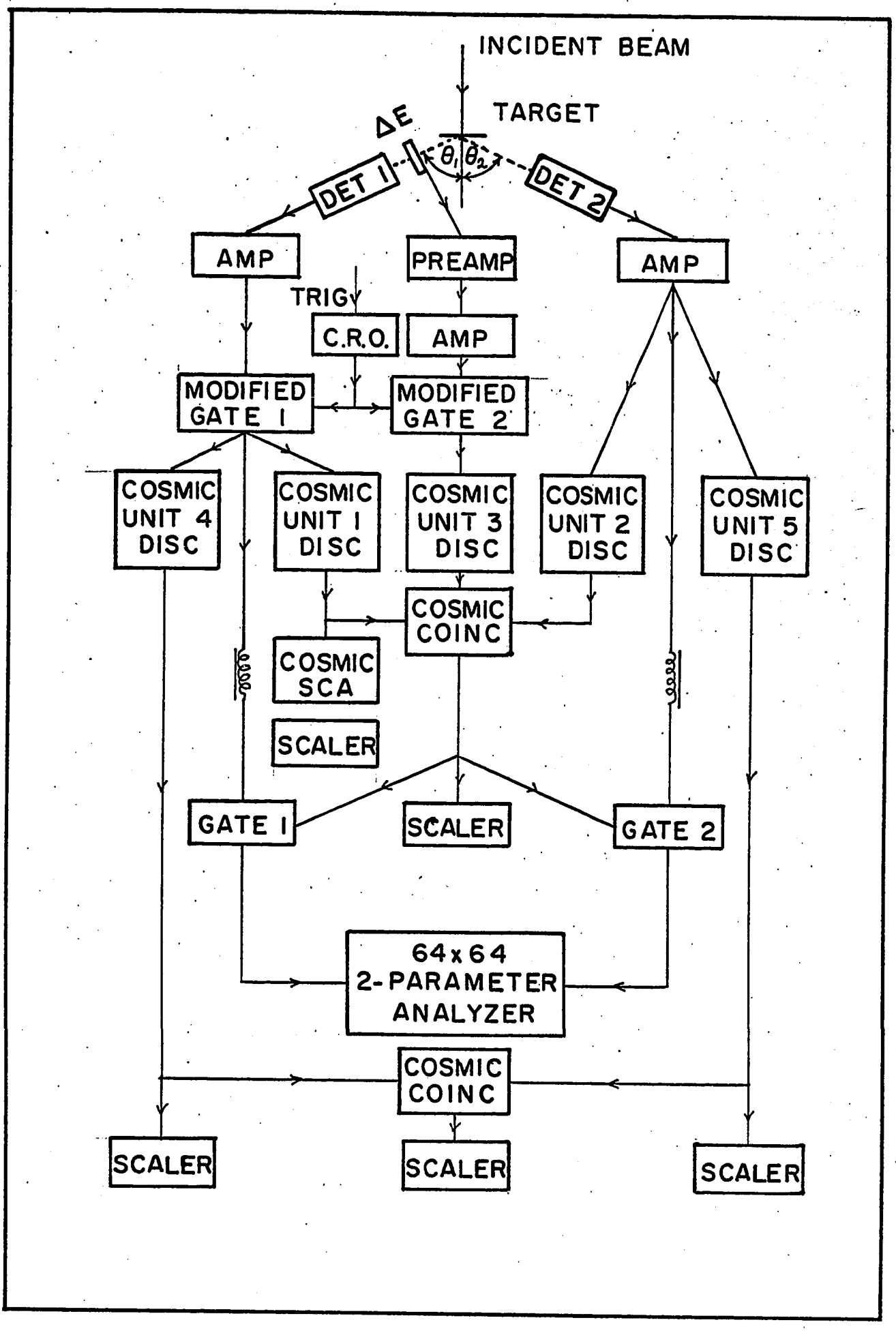
INCIDENT BEAM
TARGET
ΔE
θ1
θ2
DET 1
DET 2
AMP
PREAMP
AMP
TRIG
C.R.O.
AMP
MODIFIED GATE 1
MODIFIED GATE 2
COSMIC UNIT 4 DISC
COSMIC UNIT 1 DISC
COSMIC UNIT 3 DISC
COSMIC UNIT 2 DISC
COSMIC UNIT 5 DISC
COSMIC COINC
COSMIC SCA
SCALER
GATE 1
SCALER
GATE 2
64x64 2-PARAMETER ANALYZER
COSMIC COINC
SCALER
SCALER
SCALER

a mechanical register. The total incident proton charge was thus recorded.

II - 3. TARGET

Two kinds of deuterated hydrocarbons and their corresponding hydrogen compounds were used as target material for the experiment. They were deuterated polyethylene $(CD_2)_n$, and deuterated dotriacontane $(C_{32}D_{66})_n$, and the corresponding hydrogen compounds $(CH_2)_n$ and $(C_{32}H_{66})_n$. As their physical properties differ slightly, different techniques were used to make suitable targets. For calibration of the scattering chamber, commercial polyethylene foil was used.

II - 3a. Polyethylene

The polyethylene powder was molded into targets in a heated die under pressure. A steel die for producing 3/4" diameter circular foils was designed. It was a cylinder of 3.75" height and 2" diameter, enclosing two 3/4" diameter pistons with the powder between them. Four rod type immersion heaters were placed in holes drilled parallel to the axis close to the wall of the cylinder. Power was available from a Variac, which controlled the rate of heating of the die. A thermistor probe could be placed in an opening near the target material to measure temperature. A hydraulic press applied pressure to the upper piston during heating, and the die could be cooled by compressed air circulation.

The temperature chosen depended on the pressure and the target thickness required. If the pressure was kept at 1000 lb/in^2,

for a target about 30 mil thick, the optimum equilibrium temperature was found to be 115°C. For the experiment targets about 0.040" thick were used and their unevenness was less than 1.5%. The quantity needed for a certain thickness of powder was pre-calculated. The densities of ordinary and deuterated polyethylene were taken as 0.963 g/cm^3 and 0.975 g/cm^3, respectively. The main isotopic contamination in C_2D_4 is C_2D_3H; estimates of the amount of this contamination by the supplier agreed roughly with a mass analysis done by a pyrolysis method. The hydrogen contamination was approximately 3%.

II - 3b. Dotriacontane

Dotriacontane is a soap-like crystal ($CH_3(CH_2)_{30}CH_3 \rightarrow C_{32}H_{66}$) with a melting point of about 75°C. The deuterated sample used consisted of 83.8% $C_{32}D_{66}$ and 16.2% $C_{32}D_{65}H$, so the hydrogen contamination was 0.25%. The density of $C_{32}H_{66}$ was 0.755 g/cm^3, and that of the deuterated sample was 0.888 g/cm^3.

An aluminum ring with an inner diameter of 3/4" and height about 0.030" was made as a moulding frame. It was placed on a clean glass plate in an oven. Ordinary or deuterated dotriacontane was put in a 1 c.c. beaker in the oven, which was then warmed to a few degrees above the melting point of dotriacontane. This was then poured onto the glass plate inside the ring. Another thin glass plate pre-heated in the oven was placed on the ring as a cover to flatten the upper surface of the melted dotriacontane. Care was taken to ensure that no air was trapped between these glass plates. The target thickness was accurate to within 0.5%.

CHAPTER III. EXPERIMENTAL METHOD AND PROCEDURE

III-1. CHAMBER ALIGNMENT

III - 1a. Preliminary Alignment

A telescope was used to locate the intersection of the beam axis of the chamber with the fluorescent screens. Two lucite plates each marked with a cross indicated the centres of the entrance and exit holes of the chamber. With the fluorescent screen on the target frame out of the way, the chamber position was adjusted until the centres of these crosses were aligned with the telescope cross-hair. The target-screen and the exit-screen were then pushed into place to be marked at the point which coincided with the centres of the three crosses.

The positions of the collimators for the E detectors were aligned in the same way. With each detector at its zero angle, the lead radiation shield was moved horizontally until the centre of the collimator was observed at the cross-hair. Such a method is capable of 0.5 mm. accuracy in alignment.

III - 1b. Proton Beam Alignment

So that the chamber could be aligned with the proton beam, it was attached to the external beam pipe. The proton beam was deflected in the desired direction by the steering magnets of the external beam transport system, and passed through the centres of the two quadrupole-magnet sets into the scattering chamber. The height of

the chamber and its azimuth were adjusted until the beam hit the marked points of the target-screen and the exit-screen.

For every run the beam was focused at the marked point of the target-screen and its direction was checked by observing its position on the exit-screen. When reaction events were accumulating, the beam position could be checked by the use of screens in the view boxes of the beam transport system and the exit-screen, so that no disturbance to the experiment was introduced.

III - 2. E AND ΔE SINGLE COUNTER SPECTRA

III- 2a. E Single Counter Spectra

(i) Energy and Angular Resolution of Counter System

The operating voltage and the bias of the focusing electrodes for the phototubes were determined by detecting particles scattered from $(CH_2)_n$ at 30^o. The pulse height of protons scattered elastically from carbon was plotted against the anode voltage to determine the region of this curve where saturation began. The best peak to valley ratio and the smallest full-width-half-maximum of the ^{12}C elastic scattering peak determined the optimum setting of the focusing electrode.

In order to check the energy resolution of a counter system, any kinematic broadening effect on an energy spectrum should be avoided. The cyclotron delivers a few protons per second with its ion source switched off, and this beam was run directly into each of the two NaI detectors set at 0^o. The full-width-half-maximum of this 100 MeV

proton pulse height distribution indicated 0.8% (~800 keV) energy resolution for one of the counter systems, and 0.84% for the other. The energy resolution thus measured consisted of the energy spread of the incident protons, uncertainty in the energy loss due to the copper windows and the aluminum housings of the detector assemblies, spread due to scintillators and phototubes (NB-65), and the pulse height spread of the associated electronic systems. It did not, however, include the energy spread due to target thickness. A typical spectrum at 30° is shown in Fig. 4.

In order to measure the angular resolution of the counter systems, one detector was fixed at 40°, and the other detector was moved in the angular range around 48° on the other side of the beam direction. A profile of the coincident counts versus the angular position of the movable detector was plotted for a $(CH_2)_n$ target. The full-width-half-maximum of the profile was 3.5°.

(ii) Energy Calibration

No attempt was made to linearize the input pulse height to a pulse-height analyzer with respect to particle energy. The energy scale for the spectrum of a counter system was calibrated by the proton-proton elastic scattering peak and the protons elastically scattered from carbon at a number of suitable angles. Two body kinematics provides accurate values for energies of these proton peaks.

Results indicated slight deviation from linearity. Since Eby and Jentschke observed that the fluorescent response of NaI varies

FIGURE 4

FIGURE 4

Energy spectrum at 30^{o} from a $(CH_2)_n$ target. The 97.7 MeV peak is due to elastically scattered protons from ^{12}C, and the 74.0 MeV peak is that from ^{1}H. Peaks lying between these two indicate the excited states of ^{12}C. Their excitation energies are indicated on the diagram.

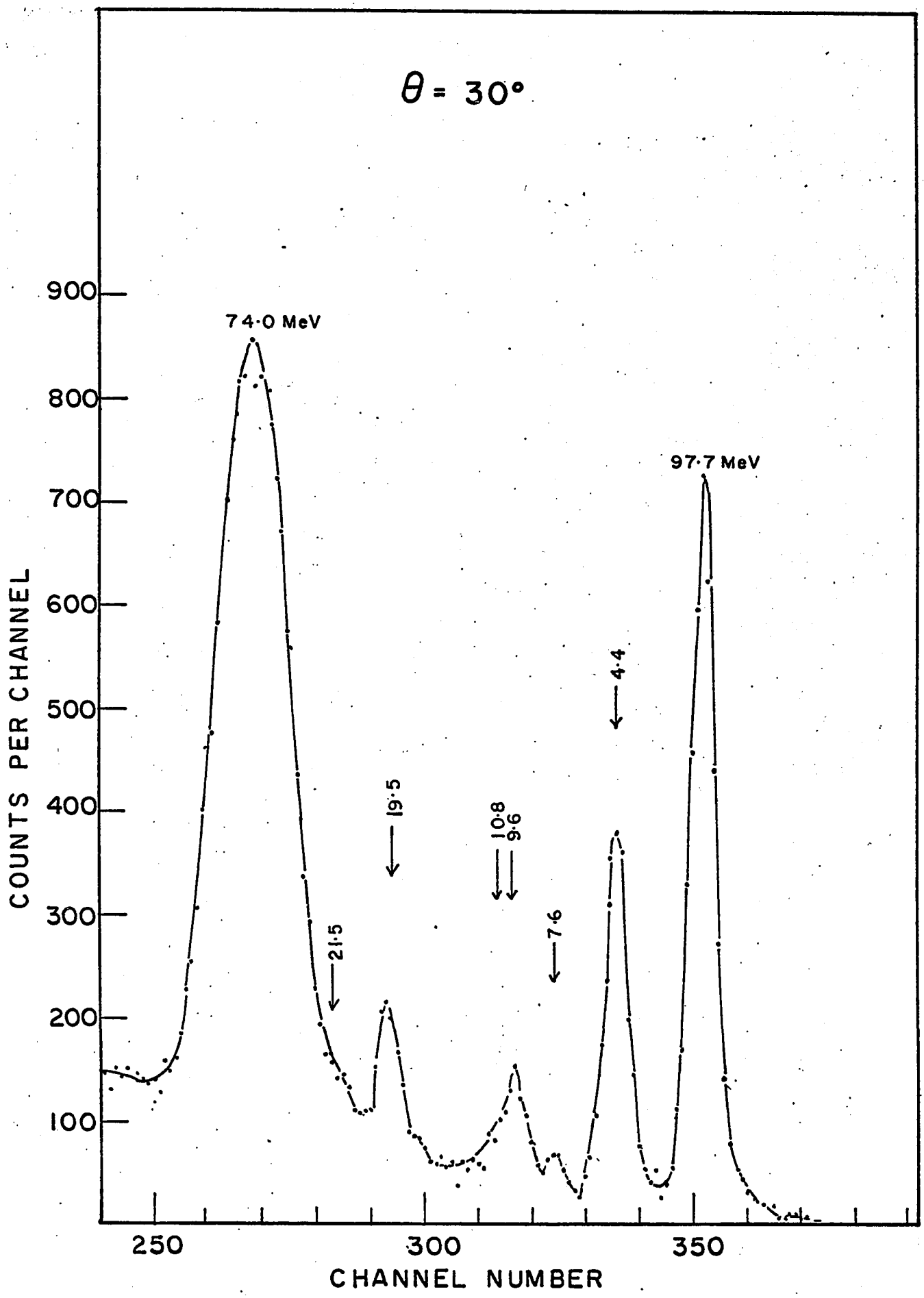
θ = 30°
74·0 MeV
97·7 MeV
21·5
19·5
10·8
9·6
7·6
4·4
COUNTS PER CHANNEL
900
800
700
600
500
400
300
200
100
250
300
350
CHANNEL NUMBER

linearly with proton and deuteron energies up to 18 MeV (EJ-54), the associated electronics systems and the effect of window absorption should account for the deviation.

(iii) Scattering Angle Calibration

As the zero degree of the angular graduation for a detector need not exactly coincide with the actual zero degree of scattering, a scattering angle calibration was carried out by determining the actual zero angles of the two detectors separately. The principle of the method used is the comparison of yields of a detector at positive angles with those at the corresponding negative angles.

A graphite target (82.69 mg/cm^2) with less than 0.1% impurity was used to obtain clean spectra. At forward angles the elastic scattering peak contributes the largest part of the total yield; hence the angular region where the elastic scattering cross section changes most rapidly with angle is desired. Proton scattering experiments at 100 MeV (Ma-65) indicate that the range from 20° to 30° in the centre-of-mass system is favorable, corresponding to 21.8° to 32.6° in the laboratory system. A typical result using detector 1 is shown in Fig. 5. The mean horizontal difference between the two curves is $2\Delta\theta = 0.95^\circ \pm 0.10^\circ$. The actual zero scattering angle is then + $(0.48^\circ \pm 0.05^\circ)$ of nominal angle, for the positive angles have a higher yield than the negative angles at the corresponding absolute nominal angles. A similar result was obtained for detector 2, whose zero angle setting is $+(0.46 \pm 0.05^\circ)$. Brief checks on yields of two positive

FIGURE 5

FIGURE 5

Zero scattering angle calibration curve of detector 1. $\Delta\theta$ is the difference between the nominal angle and the actual angle. The purely statistical error bars are not larger than the size of the experimental points.

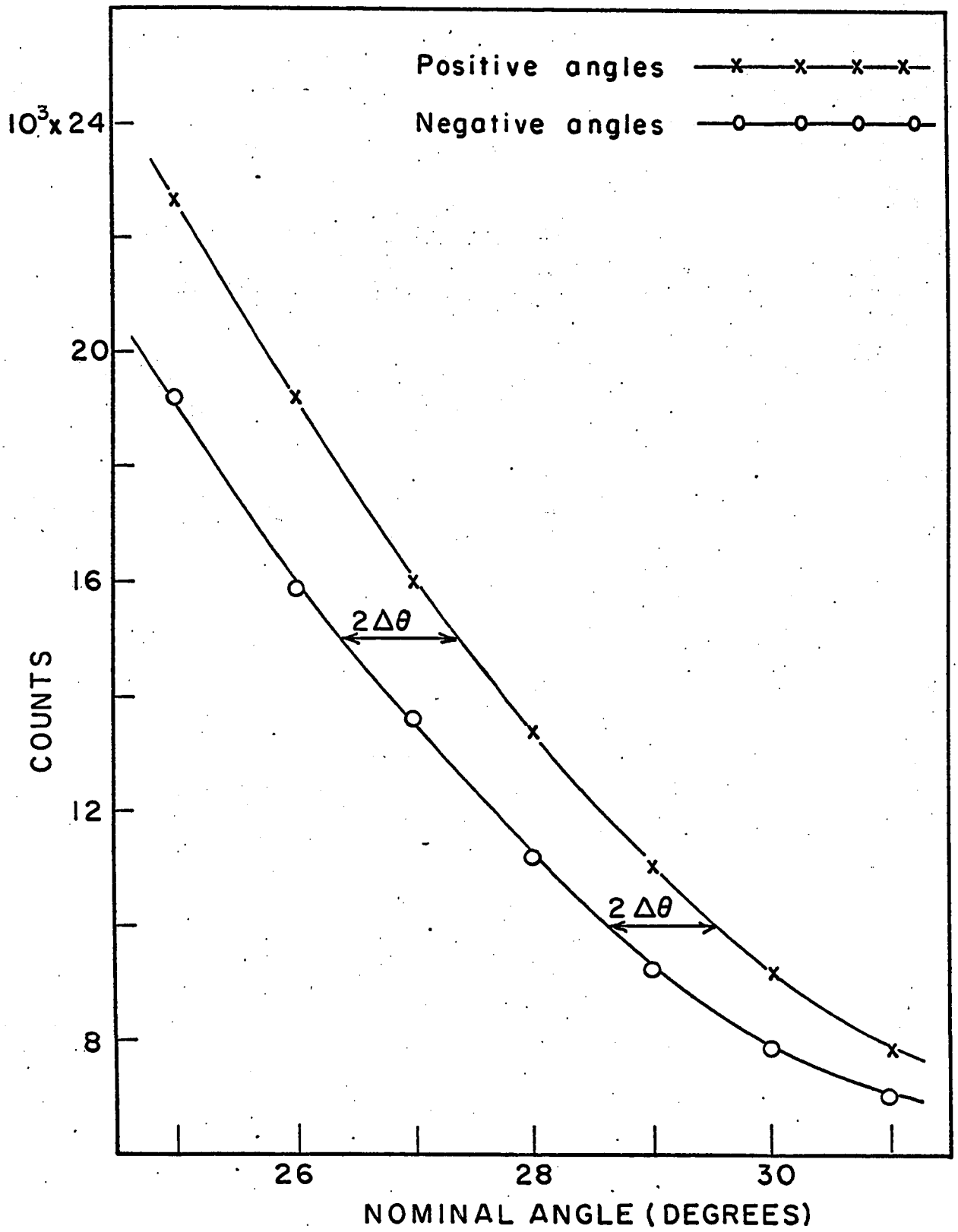
Positive angles
Negative angles
$10^3 \times 24$
20
16
12
8
COUNTS
$2\Delta\theta$
$2\Delta\theta$
26
28
30
NOMINAL ANGLE (DEGREES)

angles and one negative angle show that they differed from run to run within $\pm$ 0.10° indicating a change in the vertical position of the proton beam. The small variation of zero angle is due to the fact that the scattering plane of the chamber is vertical, and as long as the incident beam passes through the centres of the quadrupole magnets of the beam transport system, current drifts in the switching and bending magnets have little effect on the vertical position of the beam.

III - 2b. ΔE Spectra

The operating detector bias of the ΔE detector was determined by the pulse-height distribution of the output of the active filter amplifier for an alpha source. The source was located about 1 cm in front of the ΔE detector in the scattering chamber under vacuum. Optimum bias settings between +60 to +70 volts produced preamplifier output pulses of 100 nanoseconds rise time and 5.5 microseconds decay time.

As the ΔE detector was needed in triple coincidence with the E_1 and E_2 detectors, the coincident spectrum of the ΔE and E_1 detectors should reproduce essentially the same spectrum as observed by the E_1 detector alone, with only the low energy part affected. Diagrams of a ΔE v.s. E_1 coincidence spectrum and part of the energy distribution of the E_1 detector alone (which is in coincidence with the ΔE spectrum,) from a $(CH_2)_n$ target are shown on Figure 6a and 6b. The high energy portion of Fig. 6a shows slightly worse energy resolution due to the

FIGURES 6a AND 6b

FIGURE 6a

A spectrum of ΔE v.s. E_1. The ΔE axis points toward the right, and the E_1 axis runs downward to provide a convenient view of the spectrum. The most prominent curve is due to protons, the middle one is due to deuterons, and the barely visible locus belongs to tritons.

FIGURE 6b

The high energy part of the spectrum in figure 6b integrated over the ΔE axis at 35^{o}.

6 a

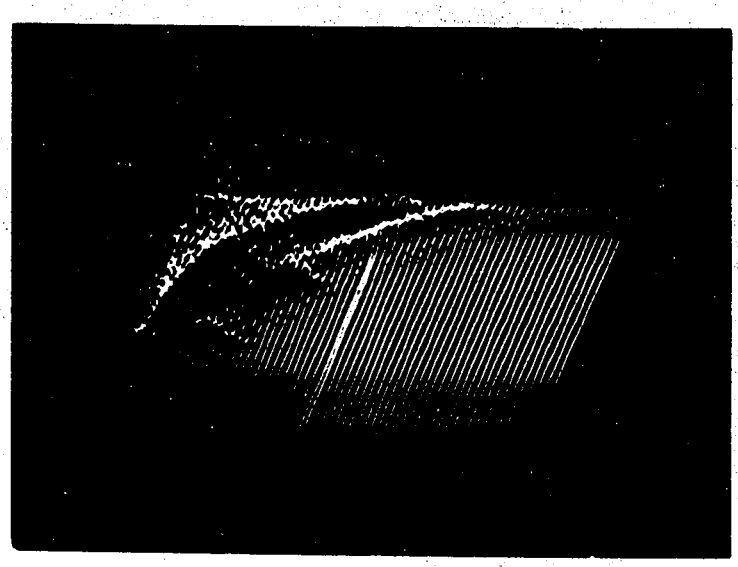

6 b

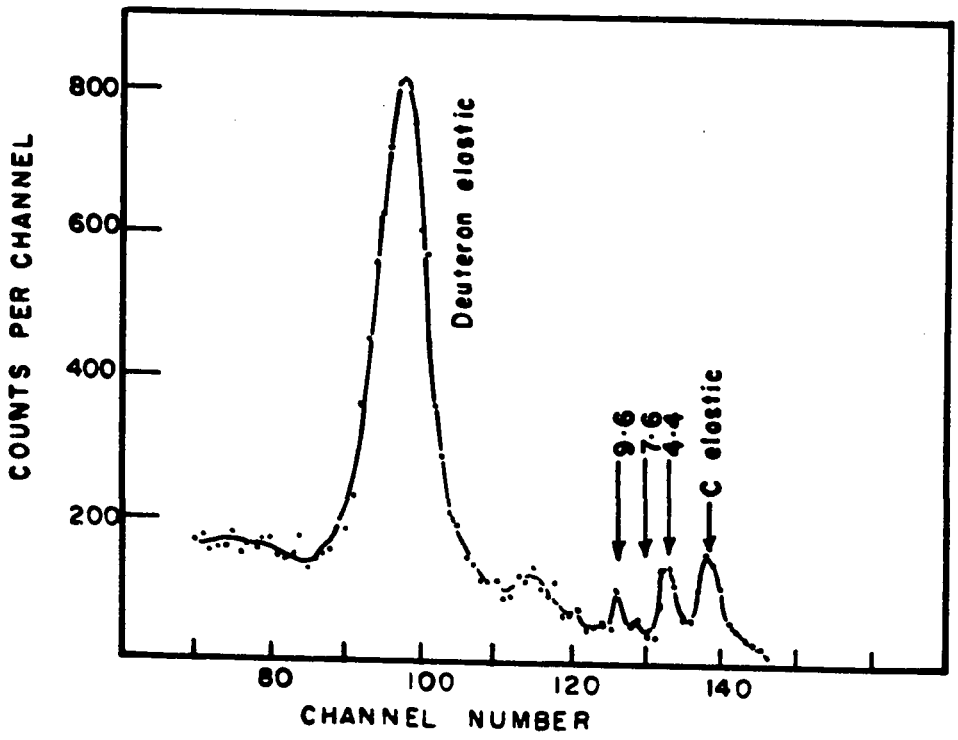
COUNTS PER CHANNEL
800
600
400
200
Deuteron elastic
9·6
7·6
4·4
C elastic
80
100
120
140
CHANNEL NUMBER

straggling effect of the ΔE detector. This effect is more clearly shown on the ΔE energy spread of Fig. 6a.

III-3. CALIBRATION OF APPARATUS AND TREATMENT OF DATA

The complete experimental system was calibrated by measuring proton-proton elastic scattering cross sections at different scattering angles and comparing them with published data of incident proton energy close to 100 MeV. The experimental results, data reduction and discussion of errors are presented in the following sections. The experiment was carried out with the pulsed proton beam.

III - 3a. Experimental Procedure

(i) Angular Range

The measurement was done by detecting the scattered protons and recoil protons in coincidence. For 100 MeV incident protons, because of the relativistic effect, the angle between the momenta of two outgoing particles of equal mass undergoing an elastic collision is ~88.5° instead of 90° in the laboratory system as predicted by non-relativistic mechanics. More specifically, this angle varies from 90° to 88.51° as the scattering angle in the centre of mass system changes from 0° to 90°. The minimum detector angle in the laboratory system which could be reached without blocking the exit beam path by the radiation shield was about 25°; this restricted the range of usable angle of scattered protons for a coincidence experiment. Another limitation was introduced by the maximum acceptance solid angle of a

detector. In the coincidence experiment one detector must be able to accept all the recoil protons whose associated scattered protons were collected by the other detector. Taking these three factors into consideration the usable angles for detecting scattered protons ranged from 31^{o} to 65^{o}.

(ii) Total Coincidence

A double coincidence circuit sends out a signal whenever two input pulses arrive within the resolving time of the circuit. The variable delays of the coincidence circuit must be properly adjusted to compensate for different lengths of the two signal cables. In the actual experiment, i.e. D(p,2p)n, the proton energies measured ranged from the low energy cutoff caused by material between the target and detector to the maximum energy allowed by three-body kinematics. The leading edge triggering mode of the coincidence circuit cannot handle such a wide energy range without losing pulses; therefore the trailing edge triggering mode was used. Under these conditions inferior resolving time could not be avoided (B-66). The apparatus was calibrated under the same experimental conditions. In order to determine the required resolving time and the relative variable delay settings, the detectors were set at suitable angles for accepting two elastically scattered protons. The discriminator of Cosmic unit 1 (Fig. 2) was set to reject low energy gamma rays. With the resolving time set at the minimum and delay 1 set at the middle of its range, a plot of the ratio of coincident counting rate to the counting rate of

discriminator 1 against the setting of delay 2 is shown in Fig. 7a. The full-width-half-maximum of the plateau shows a resolving time of 24.6 nanoseconds. The same procedure was then repeated for increasing resolving time until the height of the plateau stayed constant, indicating no coincidence loss due to too short a resolving time. The final result is shown in Fig. 7b. The delay 2 knob was therefore set at the centre of the plateau whose full-width-half-maximum revealed a resolving time of 58.5 nanoseconds.

Because the range of particle energies changed with detector angle, the procedure above was carried out for each pair of angles. The circuit shown in Fig. 2 was employed for these runs except that the gate mode switches of the modified dual linear gate were flipped to "gate out" positions because the normal pulsed beam was used. This produced no observable change in pulse height.

(iii) Chance Coincidence

The debunched beam structure is diffuse, and when it was used chance coincidences were monitored simply by inserting either of the fixed 400 nanosecond delay lines of units 3 and 4 (Fig. 2). However, with the normal pulsed beam a variable delay setting corresponding to 2 R.F. cycles was switched in.

The pulsed beam has a duty cycle of $\sim$250 with a pulse length of about 10 microseconds for each beam burst. Within a beam burst the R.F. fine structure is periodic with a 47 nanosecond interval. The variable delays of Cosmic units 3 and 4 were first adjusted to accept

FIGURES 7a. AND 7b.

FIGURES 7a. AND 7b.

Delay curves for delay 1 set at the center of its range for p-p elastic scattering. In 7a the resolving time is 24.6 nanoseconds, and in 7b its value is 58.5 nanoseconds.

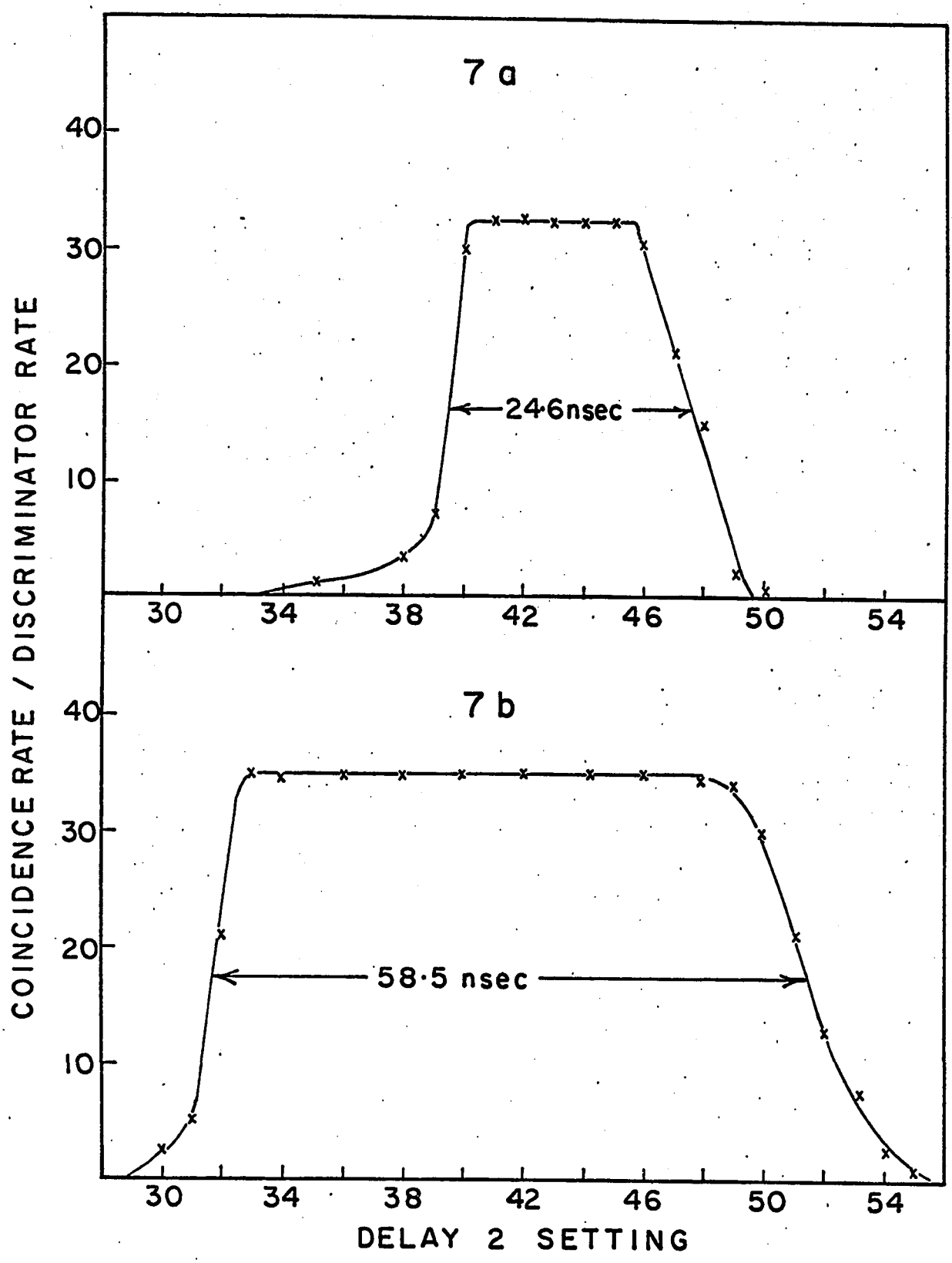
7 a
40
30
20
10
24·6nsec
30
34
38
42
46
50
54
7 b
40
30
20
10
58·5 nsec
30
34
38
42
46
50
54
COINCIDENCE RATE / DISCRIMINATOR RATE
DELAY 2 SETTING

mainly true coincident events; then an extra delay time of about 2 x 47 nanoseconds was added to one unit with respect to the other.

(iv) Current Integrator Calibration

The Faraday cup current was integrated by the picoammeter which was usually calibrated by a picoampere source. The current source was in turn calibrated by generating a known current $I = C \frac{dV}{dt}$ by means of a standard capacitor and a linearly rising voltage ramp. Details of the calibration have been described by Portner (P-67).

III - 3b. Data Reduction and Error Assignment

The equation used to calculate the experimental p-p elastic scattering cross-section is

$$\frac{d\sigma}{d\Omega} = \frac{N \cos\theta}{n N_T d\Omega} \qquad (1)$$

where N = Total number of coincidence events after correction.

θ = The angle between the normal to the target and the incident beam direction.

n = Total number of incident protons.

N_T = Number of target nuclei per unit area.

$d\Omega$ = Solid angle subtended by the collimator.

In the following paragraphs, the errors in each of these quantities and their corrections are discussed.

(i) Correction for N

It is necessary to correct for dead time losses in the Cosmic

discriminator, Cosmic coincidence unit, and the kicksorter itself. The results indicated that the dead time of the Cosmic unit restricted the counting rate of each detector, and that the dead time losses of the kicksorter (TMC400) were negligible. In fact the total number of coincident events stored in a fast scaler was the same as that in the kicksorter.

The analytical correction of dead time loss is based essentially on that given by Cormack (C-62) for counting with pulsed beams. However, since the intensity distribution within one beam burst duration resembles a triangle (O-64), a constant "k" was introduced to take account of this intensity distribution. The value of k was determined empirically.

For a fixed collected charge from the incident beam the total coincident counts of p-p elastic scattering events were plotted against the coincident counting rate and extrapolated to zero counting rate. This extrapolated number of coincidences $N_{extr.}$ represented the actual coincident counts with no dead time loss. The value of $N_{extr.}$ was inserted into the following equation for the determination of the value of k (Cr-66).

$$N_{extv.} = \frac{N_{obs.}}{\left[1 - k n_c \tau_c \left(1 - \frac{\tau_c}{2T}\right)\right]\left[1 - k (n_1 + n_2) \tau_s \left(1 - \frac{\tau_s}{2T}\right)\right]} \qquad (2)$$

where $N_{obs.}$ = The observed total number of coincidences at a certain coincidence rate after chance coincidences were subtracted.

n_c = The corresponding coincidence rate.

n_1, n_2 = The instantaneous counting rates of discriminators 1, 2, respectively.

T = 10 μsec. i.e. the duration of one beam burst.

τ_s, τ_c = Dead time of the discriminators and coincidence unit, respectively.

The averaged value of k for a set of $N_{obs.}$ was 1.67. It is close to 1.33 for the distribution of an isosceles triangle.

The chance coincidences recorded by a fast scaler were subtracted directly from the raw coincidence counts. Counts due to pile up were negligible when only runs with dead time corrections of about 5% or less were accepted. Some of the particles detected underwent nuclear interaction in the target, in the detector itself, or in passing through the material between the target and the detector. Although these particles appeared as a tail of the elastic scattering peak, they caused no problem, since the whole coincidence spectrum was taken into account for the cross-section calculation.

The formula derived by Willmes (W-66) was used to correct N for the effect of the finite sizes of target, detector, and the angular spread of the incident beam. As the beam angular spread was always less than 1° and for $\theta = 0^\circ$, this correction is less than 0.5% for all the detector angles involved.

(ii) Correction for θ

In this experiment θ was always set to 0°. Allowing an error of $\pm 10^\circ$ to θ, the error of $\cos\theta$ was then $\pm$ 1.57%.

(iii) Correction for n

In every run the Faraday cup reading was normalized by the picoampere source. The error associated with n was then that associated with the calibration of the current source, which was 1.4%. Furthermore the zero drift of the electrometer caused less than 2% error. The r.m.s. error was then 2.4%.

(iv) Correction for N_T

The $(CH_2)_n$ targets were weighed to determine their thickness. The result was checked by a micrometer which measured down to 0.0001 inch. Weighing gave the average thickness as 4.30×10^{-3} inch ($\pm$ 2.0%). Only the measurement of the target area contributed to the $\pm$ 2% error, for the error associated with weighing by an electronic balance was 0.056%, which was negligible. The micrometer also gave a value of 4.3×10^{-3} inch ($\pm$ 2.3%).

(v) Correction for $d\Omega$

The solid angle was measured to be 3.34×10^{-3} steradian with a $\pm$ 5.6% error. See Section II-1b.

III - 3c. Conclusion

The final error for each variable of equation (1) was taken as the r.m.s. value of all the errors associated with the variable. The total error for the cross-section equals the sum of all these r.m.s. values. Table III-1 gives the r.m.s. values and Table III-2(i) lists differential cross-sections for various angles at 100 MeV. These values were first compared with those by Taylor et al. (TWB-60) at

98 MeV proton energy which are listed in Table III-2(ii). Values of differential cross-sections at various angles for p-p elastic scattering at 98.8 MeV have very recently been published (WB-68) and some of them, which fall into the angular range of those of the present work at 100 MeV, are given in Table III-2(iii). The results at 98 MeV are in general smaller than those at 98.8 MeV. The smallness of the results of Taylor et al. have also been pointed out by Palmieri et al. (PC-58) who made measurements at 95 MeV incident proton energy.

In Table III-2(i) the last column lists the relative uncertainty, which is the sum of the statistical uncertainty, the uncertainty of N and those of Cos Ⓗ and n. The relative uncertainty therefore refers to the uncertainty in differential cross-section caused by factors which can change from run to run with the same experimental set-up.

TABLE III - 1

Summary of systematic uncertainties of differential cross-section in %.

N	0.5
Cos Ⓗ	1.57
n	2.4
N_T	2.3
$d\Omega$	5.6

Total uncertainty = $\pm$ 12.4%

TABLE III - 2

(i) Summary of differential cross-sections at 100 MeV proton energy

Lab. angle (degree)	$\frac{d\sigma}{d\Omega}$ (Lab)(mb sr^{-1})	Uncertainty due to counting statistics (±%)	Relative uncert-ainty (±%)
35.5	14.86	1.06	5.53
40.5	13.84	1.10	5.57
45.5	12.76	1.16	5.63
50.5	11.68	1.23	5.70
55.5	10.04	1.33	5.80
60.5	8.56	1.43	5.90

(ii) Summary of differential cross-sections at 98 MeV proton energy

Lab. angle (degree)	$\frac{d\sigma}{d\Omega}$ (Lab.)(mb sr^{-1})*a*b
35.0	14.87
40.0	13.56
45.0*c	12.41
50.0*c	11.18
55.0*c	10.05
60.0*c	8.67

*a The systematic uncertainty of ± 5% is not included.

*b The solid angle transformation is described in Appendix A.

*c These values are taken by assuming that the angular distribution of $\frac{d\sigma}{d\Omega}$ in C.M. system is symmetric with respect to 90^{o}.

TABLE III-2

(iii) Summary of differential cross-sections at 98.8 MeV proton energy.

Lab. angle (degree)	$\frac{d\sigma}{d\Omega}$ (Lab.)(mb sr^{-1})
35.0	15.28
37.5	14.64
40.0	13.97
42.5	13.50
45.0	12.85
47.5	12.31

The contents of Tables III-2(i) and III-2(iii) are plotted in Fig. 8 It is evident that our experimental values and those of Wigan et al. (WB-68) are in excellent agreement. We therefore felt confident of the performance of the apparatus.

III- 4. EXPERIMENTAL PROCEDURE FOR THE D(p,2p)n REACTION AND TREATMENT OF DATA.

III - 4a. Experimental Procedure

The procedure for the D(p,2p)n reaction does not differ much from that for p-p elastic scattering. The following will describe the part that is different.

(i) SCA monitor calibration

The debunched proton beam was used for the actual spectrum accumulation. Since the beam spike was rejected during counting (see section III-2a), the Faraday cup could not be used as a direct monitor

FIGURE 8

FIGURE 8

Proton-proton differential elastic scattering cross section at various laboratory angles for proton beam energies of 98.8 MeV and 100 MeV. The 98.8 MeV data is taken from reference (WB-68). The error bars associated with the experimental points represent the relative uncertainties in Table III-2(i) and those reported in (WB-68).

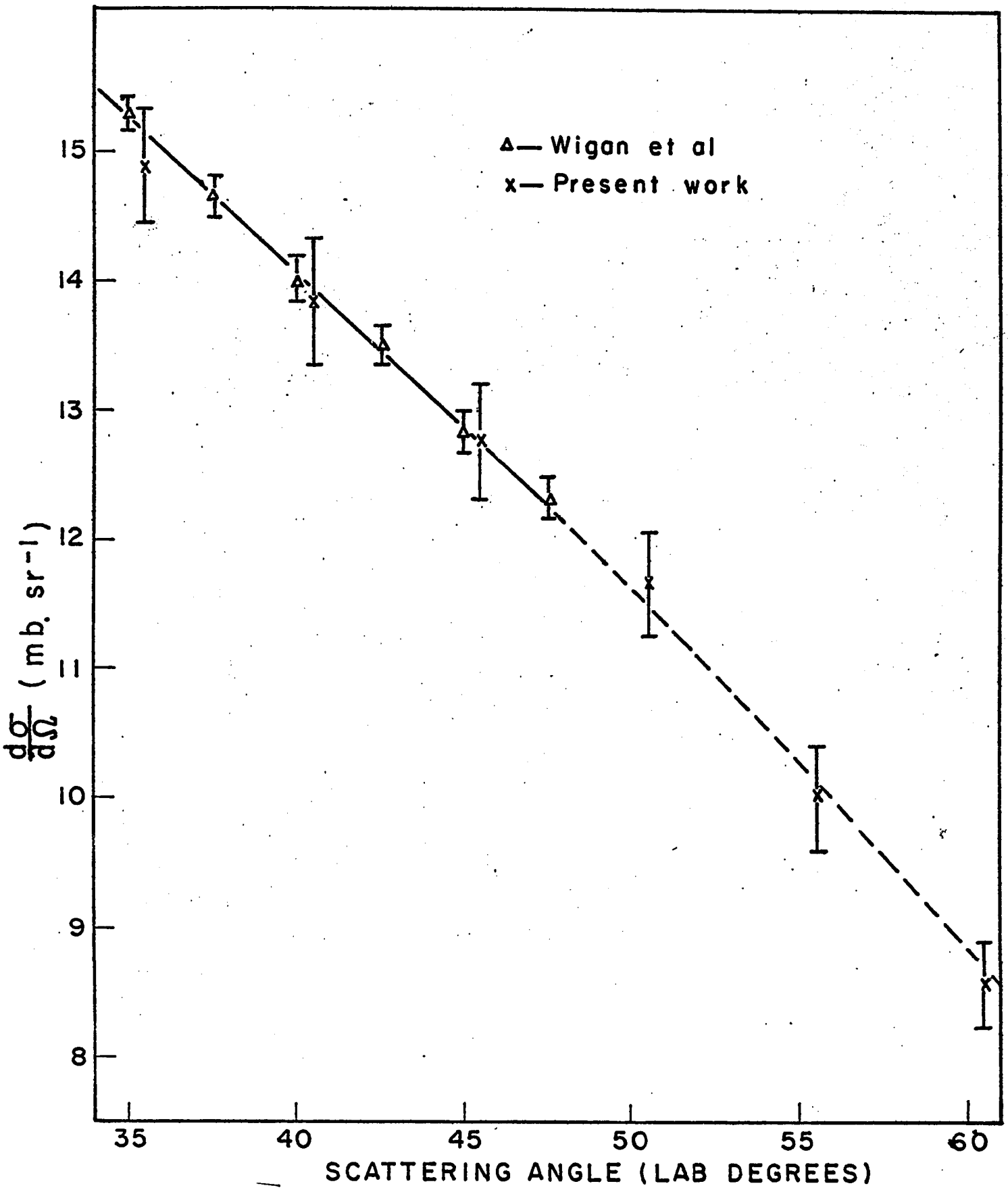
Δ— Wigan et al
x— Present work
15
14
13
12
11
10
9
8
dσ/dΩ (m.b. sr⁻¹)
35
40
45
50
55
60
SCATTERING ANGLE (LAB DEGREES)

of incident proton charge. A single channel analyzer receiving output pulses from the spike-rejection gate (Fig.2) was used as a debunched beam monitor. It was calibrated by the Faraday cup integrator using the pulsed beam with current low enough to eliminate dead time error.

The SCA accepted all pulses with heights larger than the discriminator setting. The total number of counts was recorded for a certain incident proton charge registered by the Faraday cup. The same procedure was repeated at least five times for the same incident charge, so that the average charge per monitor count was determined. The cup was then removed and the debunched beam experiment took place. The effective incident beam charge was then monitored by the SCA monitor.

(ii) Energy Calibration

The 64 x 64 two-parameter kicksorter stored coincident energy spectra from the two detectors. Their energy scales were calibrated by detecting the scattered and recoil protons of p-p elastic scattering at suitable angles. One of the typical calibration curves is shown in Fig. 9.

Since the photomultiplier gain depends on the counting rate (GV-67), the counting rate of each detector was made approximately equal to the average counting rates for the D(p,2p)n reaction when energy calibrations were performed.

FIGURE 9

FIGURE 9

Typical energy calibration curves for the 64 x 64 channel two parameter pulse height analyzer.

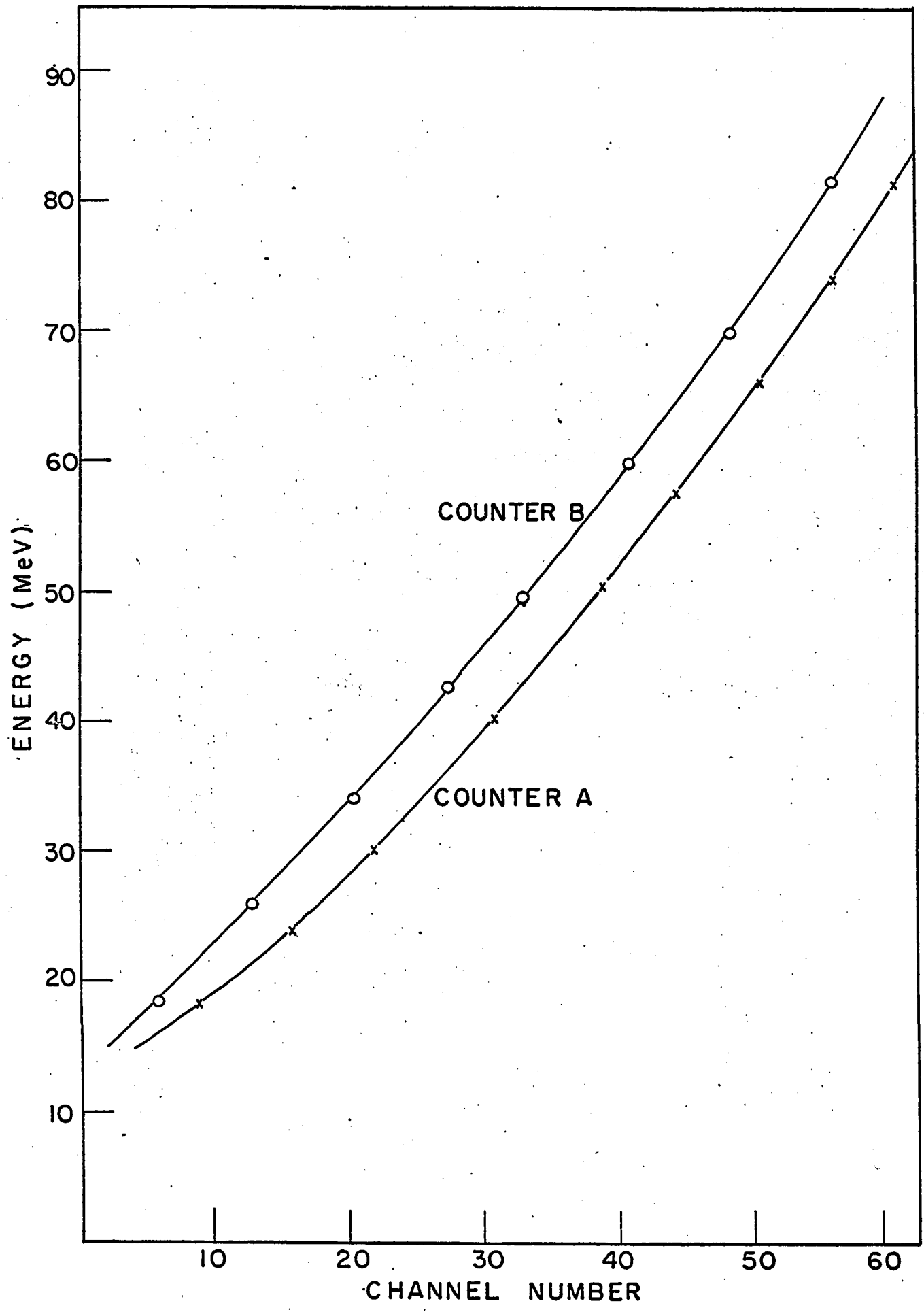
90
80
70
60
50
40
30
20
10
ENERGY (MeV)
COUNTER B
COUNTER A
10
20
30
40
50
60
CHANNEL NUMBER

(iii) Double and Triple Coincidence Circuits

The electronic set-ups are those shown in Figs. 2 and 3. The method of arranging the delay settings and resolving time resembles that described in Sec. III-3. However for the chance coincidence unit, the built in 400 nanosecond fixed delay was used instead of the variable delay.

(iv) Hydrogen Contamination Subtraction

The deuterated dotriacontane target is not 100% free from hydrogen contamination. At a pair of detector angles whose sum is close to 90^{o}, the elastic scattering events introduced by the hydrogen contamination contributes to the two-parameter energy spectrum. Because the exact quantity of the contamination is known, a subtraction of its contribution is possible. To do this a spectrum was run with normal dotriacontane ($C_{32}H_{66}$) under the same experimental conditions as in the run with a $C_{32}D_{66}$ target; it was especially important to match the counting rate of each detector with those of the $C_{32}D_{66}$ run to avoid any shift in photomultiplier gain. Section III-4b. will present details of the subtraction.

III-4b. Data Reduction and Error Assignment

The 64 x 64 channel kicksorter displays spectra of T_1 v.s. T_2. Each channel of the 64 x 64 format stores events with energies from T_1 to $T_1 + dT_1$ and T_2 to $T_2 + dT_2$. In order to compare these spectra with the theoretical predictions (which are expressed in terms

of $\frac{d^3\sigma}{d\Omega_1 d\Omega_2 dT_1}$), the spectra have to be integrated along the T_2 axis. The differential cross section formula for the integrated spectrum is

$$\frac{d^3\sigma}{d\Omega_1 d\Omega_2 dT_1} = \frac{N \cos\theta}{n N_T d\Omega_1 d\Omega_2 dT_1} \qquad (3)$$

where N = Integrated number of counts which correspond to events with kinetic energies between T_1 and $T_1 + dT_1$.

θ = The angle between the normal to the target and the incident beam direction.

n = Incident proton number.

N_T = Number of effective target nuclei per unit area.

$d\Omega_1, d\Omega_2$ = Solid angle subtended by detector 1, 2, respectively

dT_1 = Energy interval of each channel along the T_1 axis.

In the following sections, the errors and corrections involved will be discussed separately.

(i) Reduction of N

Only those counts falling on the kinematic locus of the D(p,2p)n reaction for a given pair of angles were taken into account. Chance counts were subtracted for each slice of channels parallel to the T_2 axis from the total counts by extrapolating the background through the locus. The chance to total coincidence ratio ranged from 5% to $\sim$ 14% for all pairs of angles except the pair of 40.5° - 63.5°, 40.5° - 72.5°, and 35.5° - 72.5°. The ratios for these three pairs of angles were 18.6%, 25.0%, and 35.0% respectively, due to considerably smaller differential cross sections. An uncertainty of 2% is assigned

to the method of chance coincidence subtraction for those spectra with less than 14% chance to total coincidence rate; 2.5%, 3.3%, and 4.7% are assigned to those with 18.6%, 25.0%, and 35.0% chance to total coincidence rate, respectively.

Because of nuclear interactions in the sodium iodide scintillators, some particles detected lose energy during the interaction and are "lost" from their normal channel in the kicksorter. The 64 x 64 channel kicksorter accumulates coincident events in the two detectors, so if either of the two outgoing protons from the D(p,2p)n reaction loses part of its energy through NaI interaction, the coincident signal can no longer appear on the kinematic locus. This loss has to be corrected, as its magnitude (~5%) is significant. Since the correction is energy dependent, each of the two signals has its own correction factor and the r.m.s. value of these factors is responsible for the correction to the coincident counts on the locus.

Measday has measured and calculated the tail to peak ratio in NaI crystals for protons with energies as high as 160 MeV (M-65). The calculated values were smaller than the measured ones due to the approximation applied. Felvinci's measurement (F-65) gave a result which is slightly lower than Measday's calculated curve from 60 MeV up. A check at 100 MeV was then performed by swinging a detector to the zero degree position to be bombarded directly by 100 MeV protons of greatly reduced intensity. The tail to peak ratio thus obtained was $(11.13 \pm 0.66)\%$, which fell on Measday's experimental curve and was higher than Felvinci's value of 9.2%. More precisely, the combined

interactions in the 68.05 mg/cm^2 copper window, in the 109.69 mg/cm^2 aluminum detector housing, and in the scintillator itself caused the 11.13% ratio. Since the contribution from the copper window and the aluminum housing was small in comparison with the total ratio, Measday's experimental curve was used for data correction and an uncertainty of 2% is assigned to it. In working out the correction, energy dispersion due to the finite size of the detector aperture, etc., was neglected, and this introduced a maximum uncertainty of 0.5%.

For the sake of convenience, the 40.5° - 48.1° and the 35.5° - 53.1° spectra will be called spectrum 1 and 7, respectively, according to Table IV-1 in Sec. IV-2. In these spectra, yields due to hydrogen contamination of the $C_{32}H_{66}$ target were subtracted. The $C_{32}H_{66}$ run was normalized to the same total incident proton charge and the same target thickness as the actual $C_{32}D_{66}$ run (See section III-4a.), and then 0.25% of the yield in each channel of the $C_{32}H_{66}$ two parameter spectrum was subtracted from the yield of the corresponding channel of the $C_{32}D_{66}$ run. A cross-section which will be introduced later (Section V-1) in the analysis of results is $\frac{d^2\sigma}{d\Omega_1 d\Omega_2}$. This involves only the total number of counts, so only the uncertainty in the total number of counts of a D(p,2p)n spectrum will be discussed. Due to the uncertainty of 1.4% for each of the two incident charge measurements, 0.5% for the two target thicknesses, and 4% for the percentage contamination determination, there is a total error of 7.8% to the normalization factor for both spectra. However the ratio

of the total number of counts actually subtracted to the total number of counts of the spectra were 11.6% and 11.7% for spectrum 1, and 7, respectively, giving final errors of 0.90% and 0.91% respectively.

No correction was applied to the spectrum of 35.5^{o} - 84.5^{o}, as the dead time correction to the ΔE detector was unknown. The dead time correction to the Cosmic unit for all other spectra was negligible. This is true because any deadtime loss of discriminator 1 was compensated by the SCA monitor, and the counting rate of counter 2 was kept below 600 counts per second, which was free from any dead time correction for the debunched beam. Besides this, the coincidence rate was low enough (< 180 counts/minute), to make coincidence losses negligible.

In short, the overall r.m.s. uncertainty in the determination of the total number of events on the kinematic locus is 2.9% except for spectra 1 and 2, and spectra 12, 13, and 14. An uncertainty of 3.0% should be allowed for spectra 1, and 2, and 3.2%, 3.9% and 5.1% allowed for spectra 12, 13, and 14, respectively.

(ii) Corrections to n, N_T, and $\cos\theta$

During the SCA monitor calibration, the electrometer zero drift caused less than 1% error over short counting periods. Many effects such as electrometer drifting, the drifting of beam position, and the presence of high energy γ-rays can affect the monitor calibration. Combining all kinds of effects the monitor calibration could be reproduced within 2%. Together with the 1.4% uncertainty due to the

picoampere source calibration, the r.m.s. error in "n" was 2.4%.

A 0.0310" $C_{32}D_{66}$ target and a 0.0416" CD_2 target were used, so the uncertainties of their corresponding N_T were $\pm$ 0.4% and $\pm$ 1.5% respectively (See section II-3).

For almost all the spectra, Φ was set to zero with 1.6% uncertainty of $\cos\Phi$ (See section III-3b.). The exceptional cases were spectra 13 and 14, for which $\Phi \simeq 20^{\circ}$ with about 7% uncertainty.

(iii) Values of $d\Omega_1$, $d\Omega_2$, and dT_1

The solid angles subtended by the two brass collimators are identical to 0.2%, and are quoted as 3.34×10^{-3} steradians with 5.6% uncertainty. (See section III-3b.).

The value of dT_1 and its uncertainty are functions of particle energy. However for the part of the spectrum with the highest yield, a 2% inaccuracy was typical, except for those spectra in which low energy protons detected by detector 1 predominated. For those three spectra 5% had to be allowed.

III - 4c. Conclusion

Since the cross-section equation in section III-4b. is energy dependent, a review of the systematic uncertainties presented in the last section will only apply to $\frac{d^2\sigma}{d\Omega_1 d\Omega_2}$ which is in fact the quantity needed for a Chew-Low plot. They are listed in Table III-3 for those spectra involved in the Chew-Low plot, i.e. spectra 1-12.

TABLE III-3

Summary of systematic uncertainties in % of

N	2.9 (3.0)*a
$\cos\Theta$	1.6
n	2.4
N_T	0.4 (1.5)*b
$d\Omega_1$	5.6
$d\Omega_2$	5.6
	18.5

*a The 3.0% is for spectra 1 and 7 only.

*b For spectra 2-6, 1.5% is appropriate; for spectra 7-11 and 1 0.4% should be quoted.

CHAPTER IV. REACTION MECHANISM AND EXPERIMENTAL DATA

IV - 1 REACTION MECHANISM

A nuclear reaction is characterized by the reaction mechanism through which it takes place and its dynamic properties. For three-body reactions there have been experiments indicating enhanced reaction cross-sections at particular internal energies or certain values of momentum transfer variables. Typically the former is due to the sequential process of the reaction, and the latter is seen in quasi-free processes. For the D(p,2p)n reaction one expects the following possible reaction channels:

$$p + D \longrightarrow p + D \qquad (1)$$

$$\longrightarrow p + p + n \qquad (2)$$

$$\longrightarrow p + {}^{2}H^{*} \longrightarrow p + p + n \qquad (3)$$

$$\longrightarrow n + {}^{2}He \longrightarrow p + p + n \qquad (4)$$

Equation (1) represents elastic scattering, and equation (2) the simultaneous break-up of a deuteron by a proton. Equations (3) and (4) take place via a virtual deuteron state, and a di-proton state, respectively. It is the purpose of this section to investigate the kinematics of the reaction channels with three particles in the final state.

IV - 1a. Simultaneous Break-up

There are nine degrees of freedom associated with an isolated

system of three particles. Fortunately not all of them are independent variables. The laws of momentum conservation and energy conservation provide four equations relating the variables, so that five of them are independent. In the laboratory system it is convenient to choose the polar and azimuthal angles of two of the three particles and the energy of one of these two as the independent variables, and constraints are then imposed on them. However, mathematically there are two possible solutions for the dependent variables from the given values of the five independent ones. This will be described in more detail in the following section. In order to clarify this situation an extra variable, the energy of the other particle, was also measured in the experiments.

The non-relativistic three body kinematics has been well documented (e.g. DKZ-64, AGK-66). Though the relativistic case is more complicated, it is straightforward. Applying the conservation of momentum and energy

$$\vec{P}_0 + \vec{P}_T = \sum_{i=1}^{3} \vec{P}_i \qquad (5)$$

$$E_0 + E_T = \sum_{i=1}^{3} E_i$$

where $\vec{P}_0(p_o, \theta_o, \varphi_o)$ and E_0 are the momentum and total energy respectively of the incident particle, $\vec{P}_T(p_T, \theta_T, \varphi_T)$ and E_T are for the target nucleus, and $\vec{P}_i$, E_i are those of the outgoing i^{th} particle, one can solve for the dependent variables. For a coplanar reaction the solu-

tion of E_2 is given below in terms of Fortran notation; the incident beam direction is the Z axis.

$$E_2^{\pm} = \frac{-G \pm \sqrt{G^2 - 4FH}}{2F} \qquad (6)$$

$$F = 4A^2 - D^2, \quad G = -2CD, \text{ and } H = -(4A^2M_2^2 + C^2)$$

$$A = -P_o \cos\theta_2 + P_1 \cos(\theta_1 + \theta_2)$$

$$B = P_o^2 + P_1^2 + M_3^2 - 2P_oP_1 \cos\theta_1$$

$$C = M_2^2 + (M_T + E_o - E_1)^2 - B$$

$$D = -2(M_T + E_o - E_1)$$

The velocity of light, c, has been taken as unity in the equations above. The values of P_3, θ_3 and φ_3 can then be obtained by substituting eq. (6) into (5). It is obvious from (6) that there are two possible solutions. Only those values which satisfy the law of energy conservation are acceptable. The unacceptable values of E_2 come from negative values of momentum along the same direction as that of the positive ones.

In the laboratory two detectors are set at a pair of angles to detect two of the three outgoing particles. If one plots the energy spectrum of a detector vs. that of the other detector, there will be six loci on the graph when all three particles have different masses. If two of the three are particles of equal mass, there will be two loci, and if all particles are of the same mass, there will be only one locus even if the outgoing neutron could be detected. Fig. 10 shows the loci for different proton energies in the D(p,2p)n and the $^{12}C(p,2p)^{11}B$

FIGURE 10

FIGURE 10

Kinematic loci for the reactions D(p,2p)n, and $^{12}C(p,2p)^{11}B$ for different incident proton energies. T_1 and T_2 are the proton energies detected by two detectors set at 40° with respect to the beam direction.

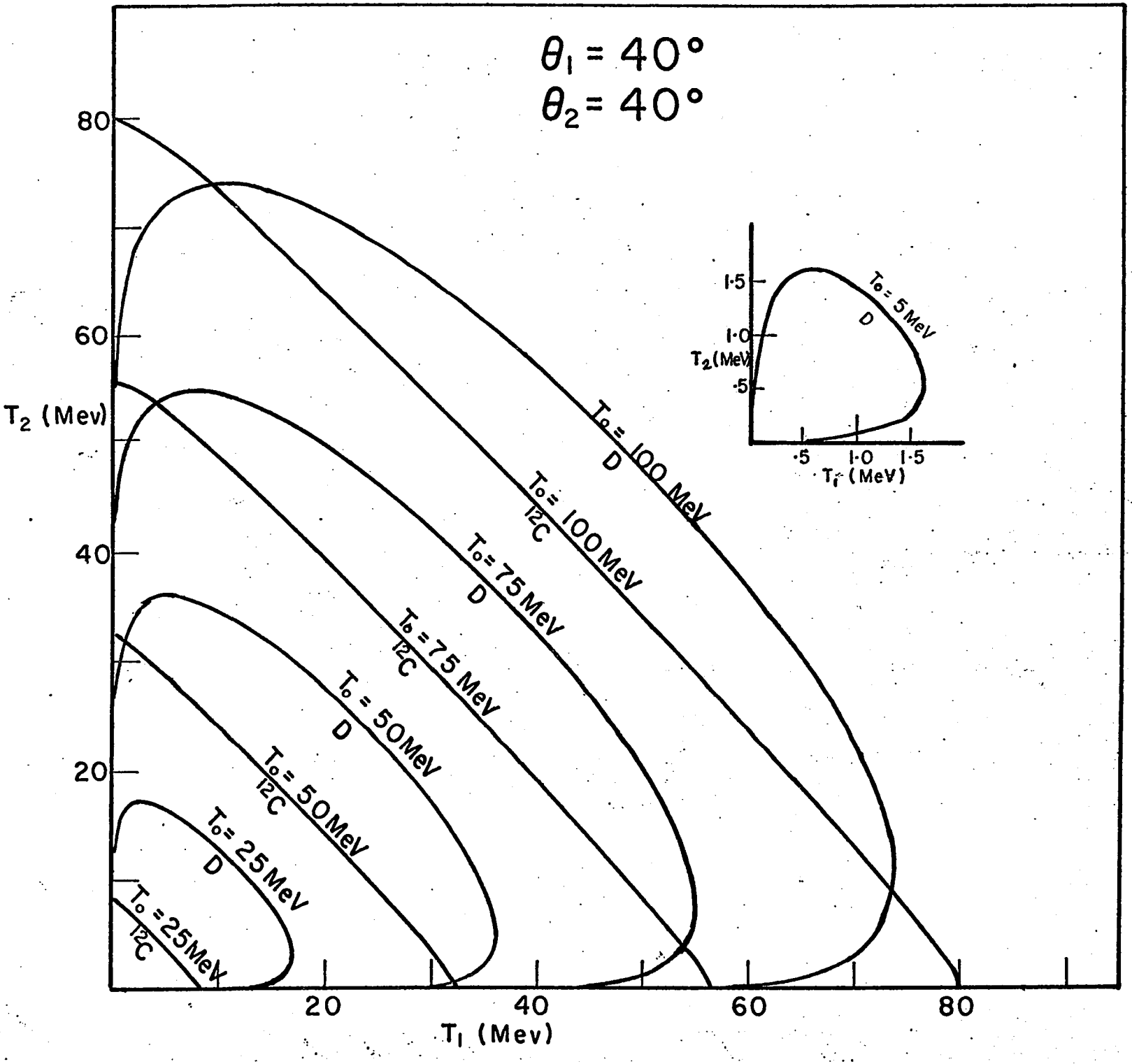
θ1 = 40°
θ2 = 40°
T2 (Mev)
T1 (Mev)
80
60
40
20
20
40
60
80
To = 100 MeV
D
To = 100 MeV
12C
To = 75 MeV
D
To = 75 MeV
12C
To = 50 MeV
D
To = 50 MeV
12C
To = 25 MeV
D
To = 25 MeV
12C
To = 5 MeV
D
1·5
1·0
·5
T2 (MeV)
·5
1·0
1·5
T1 (MeV)

reactions.

IV - 1b. Sequential Break-up

Reaction (3) and (4) on page 45 are two step reaction channels; nevertheless the momenta and energies of the outgoing particles of these channels are still the same as those of the simultaneous break-up. When the reaction takes place through one of these channels, there will be an enhanced yield on a particular portion of the kinematic locus which corresponds to the appropriate internal energy of the two particles which are left behind to form a short-lived intermediate state, such as $^{2}H^{*}$ of the reaction channel (3).

The analytical relations between the internal energies of various intermediate states and the basic kinematic variables could be found from the conservation of energy and momentum. Consider a break-up process which proceeds through two steps such as

$$a + b \longrightarrow i + (jk) \qquad (7a)$$

$$i + (jk) \longrightarrow i + j + k \qquad (7b)$$

where the values of i, j, and k are any permutation of 1, 2, and 3. For example if i = 1, j = 2, and k = 3, (7) indicates that the particle detected by detector 1 is the first outgoing particle, and the particle detected by detector 2 and the undetected particle (which is labelled as 3) are left to interact for a longer time. Eq. (7b) represents the decay of the composite system. In the D(p,2p)n reaction, the outgoing neutron will not be detected. From the laws of

momentum and energy conservation,

$$\begin{aligned} \vec{P}_o + \vec{P}_T &= \vec{P}_i + \vec{P}_{jk} \\ E_o + E_T &= E_i + E_{jk} + E^I_{jk} \end{aligned} \tag{8}$$

one can easily write down the analytical form of the internal energy of the (jk) system, E^I_{jk}, for coplanar reactions,

$$E^I_{jk} = E_o - E_i - \sqrt{P_i^2 + P_o^2 - 2P_oP_i \cos\theta_i + M_{jk}^2} + M_T \tag{9}$$

In this notation $\vec{P}_{jk}$ (P_{jk}, θ_{jk}, φ_{jk}) and E_{jk} represent the momentum and the total energy excluding E^I_{jk} of the composite system (jk), respectively, and M_{jk}, M_T are the masses of (jk) and the target. Because of the two solutions discussed in section IV-1a., E^I_{13} and E^I_{12} will be double-valued, while E^I_{23} is single valued. From eq. (9) it is also clear that every point on a kinematic locus corresponds to certain values of the internal energies for different composite systems.

If one knows the internal energy of a certain composite system, one can predict through eq. (9) the kinematic conditions under which the composite system can be observed most conveniently if the reaction does take place via the reaction channel of this composite system. It is expected, for example, that the internal energy of a virtual deuteron is about 50 keV. To examine an experiment in which one of the two detectors is set at a fixed angular position, and the other detector is set at various angles on the (coplanar) reaction plane, a curve of T_f, the particle energy detected by the fixed detector, versus θ_m,

the movable counter angle for a definite internal energy of the virtual deuteron can be plotted. On such a graph, T_f will be constant when the first outgoing particle enters the fixed detector; otherwise T_f varies with θ_m. In Figs. 11 and 12 such graphs are shown for the reaction D(p,2p)n at T_o = 100 MeV and θ_f = 40.5 ° and 35.5°, respectively.

IV - 2. EXPERIMENTAL DATA

The experimental results are divided into two categories. One of them includes D(p,2p)n reactions with small mean neutron energies; the other contains spectra of low internal energies of the singlet (n,p) system.

The first category consists of two sets of data. In the first set are six coincidence spectra taken with one detector angle fixed at 40.5° and the other detector set to various angles between 30° to 50° on the other side of the beam axis. In the second are five coincidence spectra taken with one detector angle fixed at 35.5° while the opposite detector was moved from about 35° to 55°. The angles between the two detectors were thus always less than 90°, so that the p-D elastic scattering did not contribute to the spectra and yet for every pair of detector angles the mean energy of the undetected neutrons was close to zero, as desired. Both detectors have a low energy cut-off because of the materials which particles have to pass through in order to reach the sodium iodide. These cut off energies affect only the two spectra with detectors at 40.5° - 30.5°, and 40.5° - 32.5°. The portion of these spectra which corresponds to low energy protons detected by the fixed detector and high energy protons by the movable

detector is still distinguishable from the background, and the spectra are chopped off at about 15 MeV in agreement with a calculation based on the range-energy relation (RM-54). Series of these two-parameter spectra are shown in Figs. 13 and 14 with corresponding energy curves for the undetected neutron. It is apparent that the D(p,2p)n reaction proceeds preferentially at small momentum transfer to the neutron, at least for those angular configurations shown.

In order to predict kinematic conditions favouring the formation of a virtual deuteron one has to consult Figs. 11 and 12 for $\theta_f = 40.5^o$ and 35.5^o respectively. Fig. 11 shows that $\theta_m \simeq 60^o$ and the angular range $66^o < \theta_m < 72^o$ should be kinematically favourable for observation. However, due to the finite apertures of the detectors it is unfortunately not possible to separate the low energy tail of the p-D elastic peak and part of the 3-body kinematic locus for the deuteron break-up reaction, and the part of the locus obscured by the tail due to NaI interactions in the detector is just where one expects the singlet (np) system to be observed. Moreover on account of the angular resolution of 3.5^o at FWHM, only spectra at $\theta_m = 63.5^o$ and $\theta_m = 75.5^o$ were taken for $\theta_f = 40.5^o$. The situation for $\theta_f = 35.5^o$ is the same; spectra at $\theta_m = 72.5^o$, $\theta_m = 84.5^o$ were accumulated. They are shown on Figs. 15a, b, c, d, which include the internal energy curves as well as the energy curves of the outgoing neutron.

All the spectra of Fig. 15 have a general feature: each is composed of two peaks, one centering around the portion of the locus where the (n,p) intermediate system with low internal energy is

FIGURES 11 AND 12

FIGURES 11 AND 12

These are plots showing the regions of interest in the study of the D(p,2p)n reaction at 100 MeV. The curves labelled $T_M(MAX)$, $T_f(MAX)$ show the maximum proton energies allowed by the 3-body kinematics in the movable detector and the fixed detector, respectively. The marked points in the diagrams are the locations of two body elastic scattering.

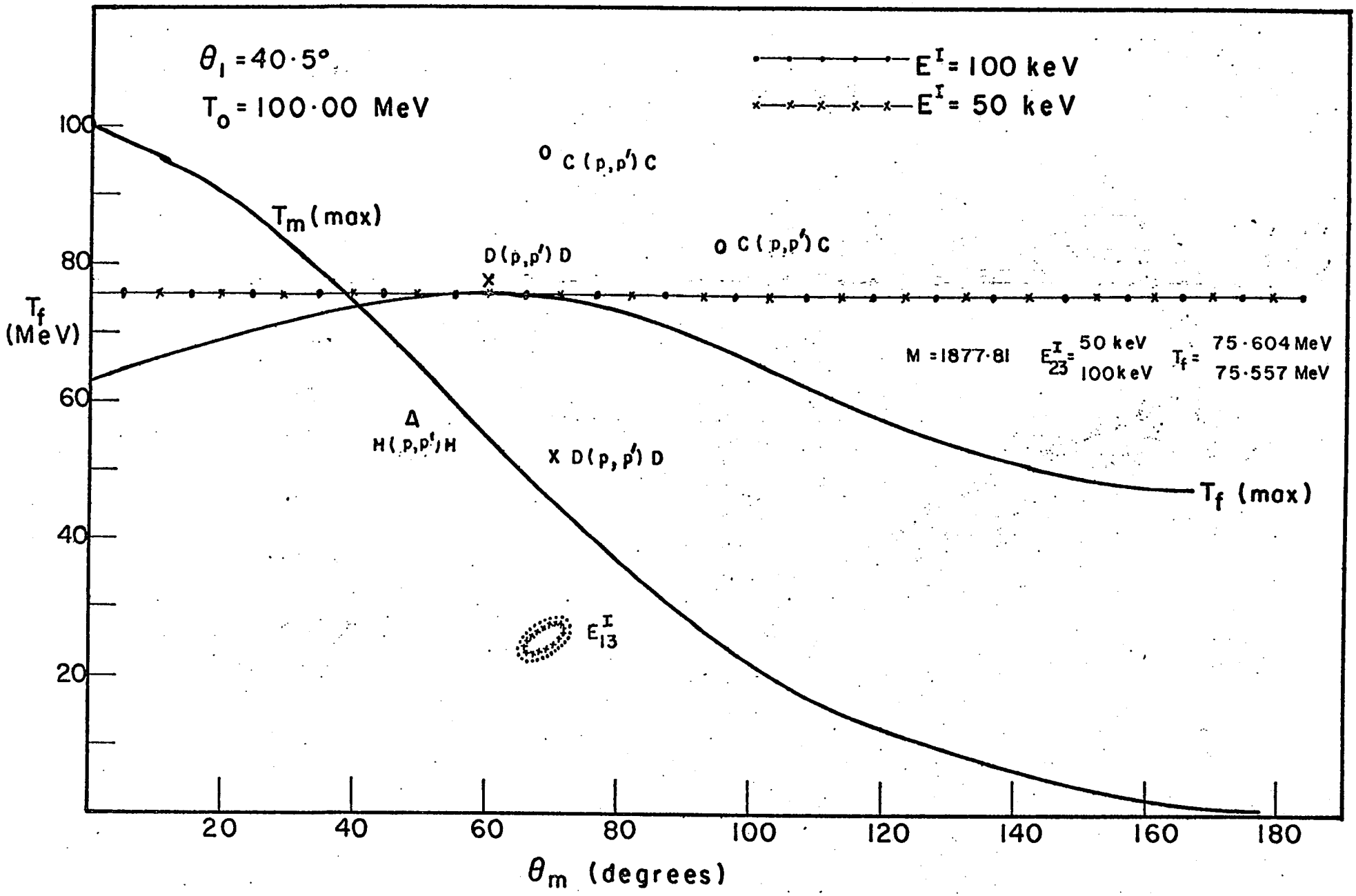
θ1 = 40·5°
T0 = 100·00 MeV
E^I = 100 keV
E^I = 50 keV
O C (p,p') C
Tm (max)
D (p,p') D
O C (p,p') C
Tf (MeV)
M = 1877·81
E^I_23 = 50 keV
100 keV
Tf = 75·604 MeV
75·557 MeV
Δ
H (p,p') H
X D (p,p') D
Tf (max)
E^I_13
100
80
60
40
20
20
40
60
80
100
120
140
160
180
θm (degrees)

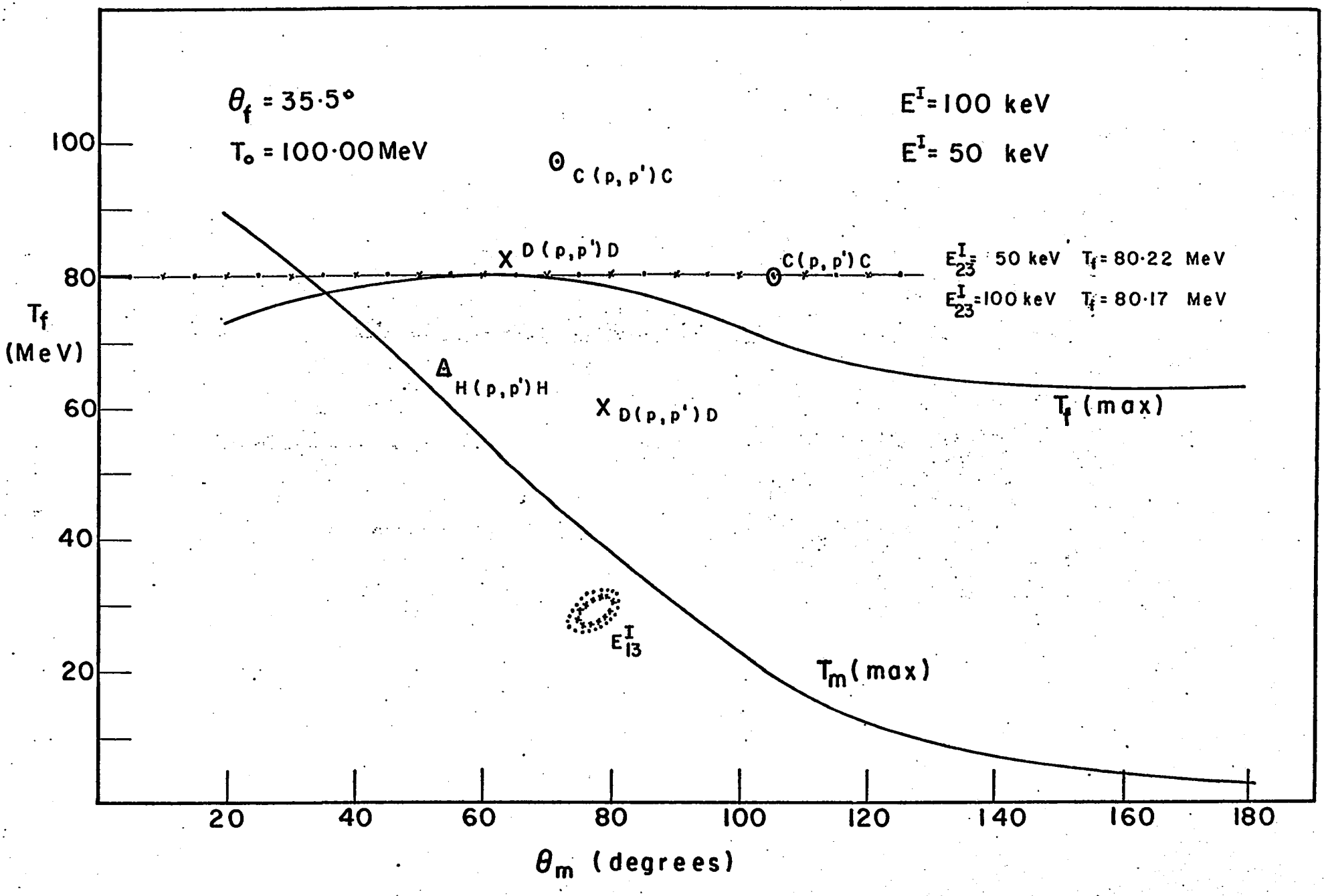
θ_f = 35·5°
T_o = 100·00 MeV
E^I = 100 keV
E^I = 50 keV
C (p, p') C
D (p, p') D
C(p, p') C
E^I_{23} = 50 keV T_f = 80·22 MeV
E^I_{23} = 100 keV T_f = 80·17 MeV
H (p, p') H
D(p, p') D
T_f (max)
T_m (max)
E^I_{13}
T_f (MeV)
100
80
60
40
20
20
40
60
80
100
120
140
160
180
θ_m (degrees)

expected, and the other part has an enhanced cross-section associated with small neutron energy.

In Table IV-1 all the spectra are listed and a reference number is assigned to each.

TABLE IV - 1

Spectrum Number	Detector Angle 1	Detector Angle 2
1	40.5°	48.1°
2	40.5°	42.5°
3	40.5°	39.5°
4	40.5°	36.5°
5	40.5°	32.5°
6	40.5°	30.5°
7	35.5°	53.1°
8	35.5°	48.5°
9	35.5°	44.5°
10	35.5°	39.5°
11	35.5°	34.5°
12	40.5°	63.5°
13	40.5°	75.5°
14	35.5°	72.5°
15	35.5°	84.5°

FIGURE 13 (a,b,c,d,e,f)

FIGURE 13 (a,b,c,d,e,f)

Two parameter spectra for the D(p,2p)n reaction at 100 MeV with detector 1 fixed at 40.5°. The curves labelled E_3 represent the kinetic energy of the undetected particle, (neutron), vs. E_1 which is the kinetic energy of a proton detected by the fixed detector 1.

The solid curves passing through the loci are calculated from 3-body kinematics.

(a)

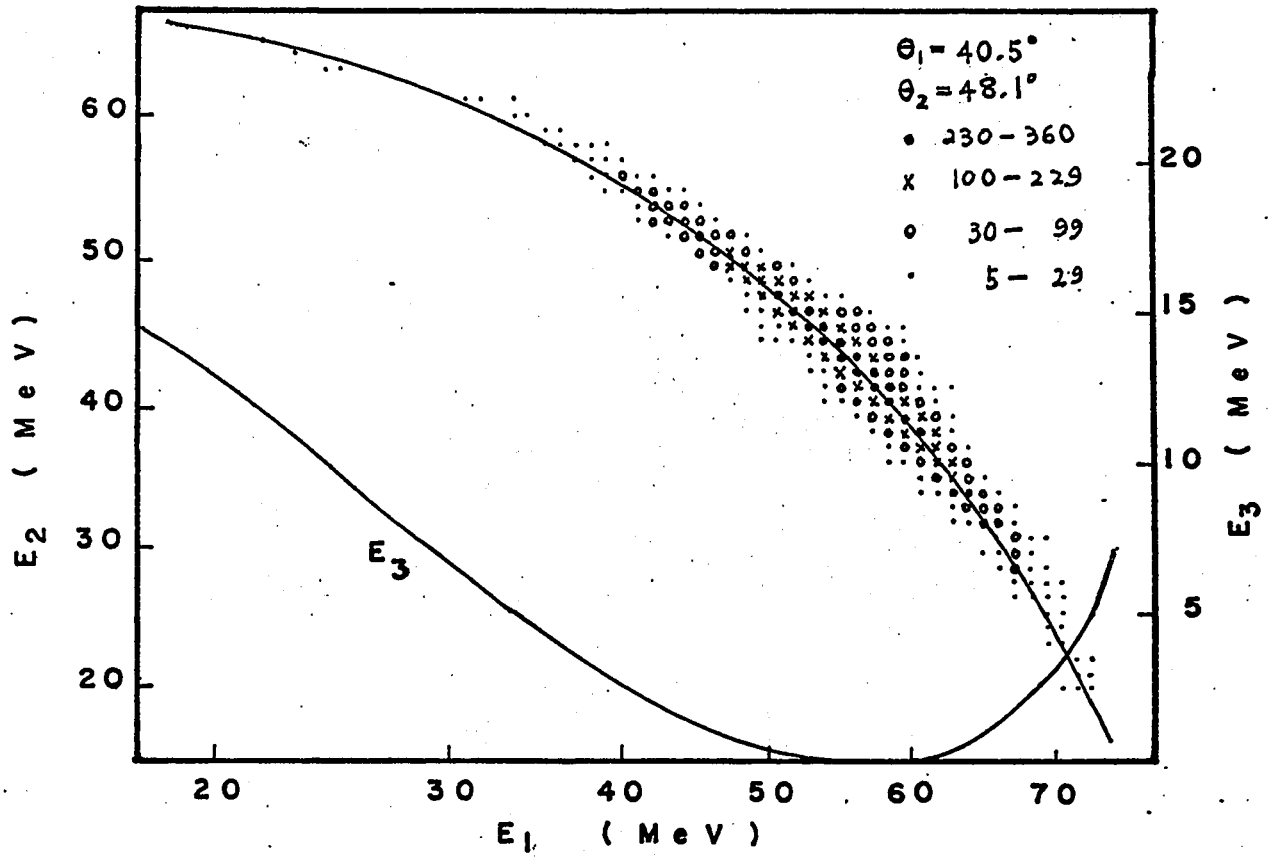
θ1 = 40.5°
θ2 = 48.1°
• 230 - 360
x 100 - 229
o 30 - 99
· 5 - 29
E3
E2 (MeV)
E3 (MeV)
E1 (MeV)
20
30
40
50
60
70
5
10
15
20

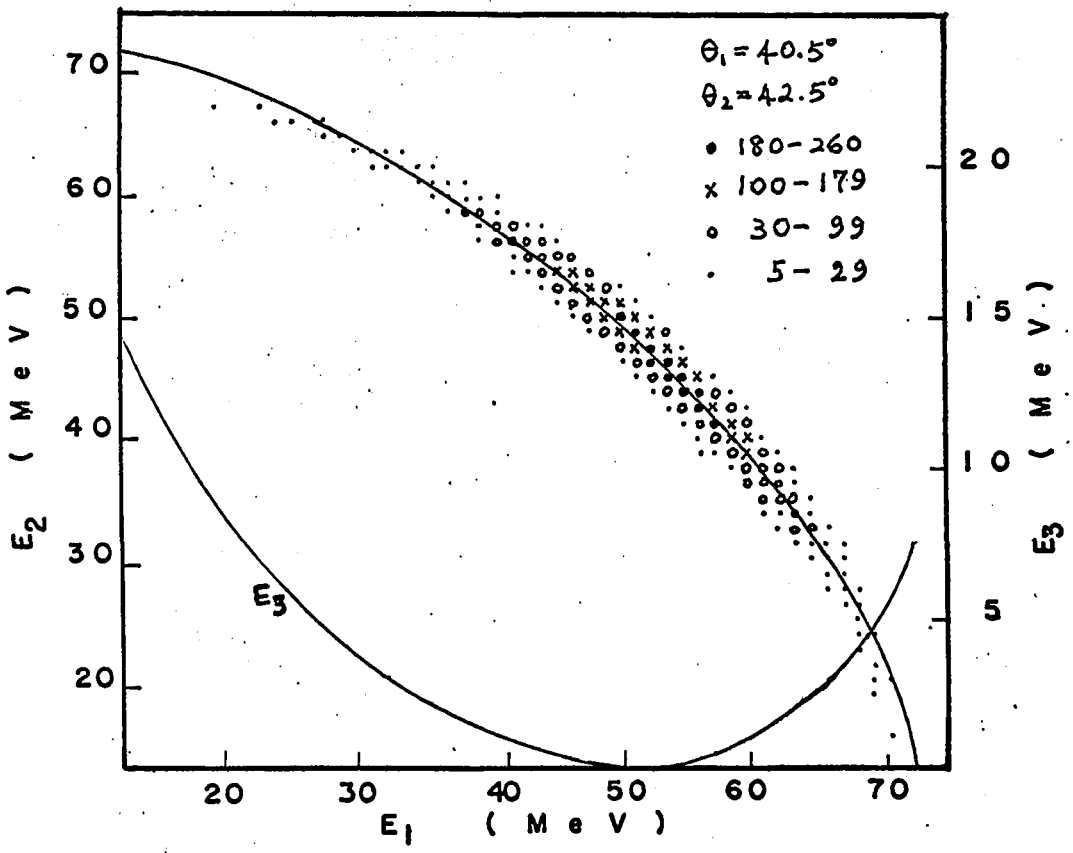
θ1 = 40.5°
θ2 = 42.5°
• 180 - 260
x 100 - 179
o 30 - 99
· 5 - 29
E3
E2 (MeV)
E3 (MeV)
E1 (MeV)
20
30
40
50
60
70
5
10
15
20

(b)

(c)

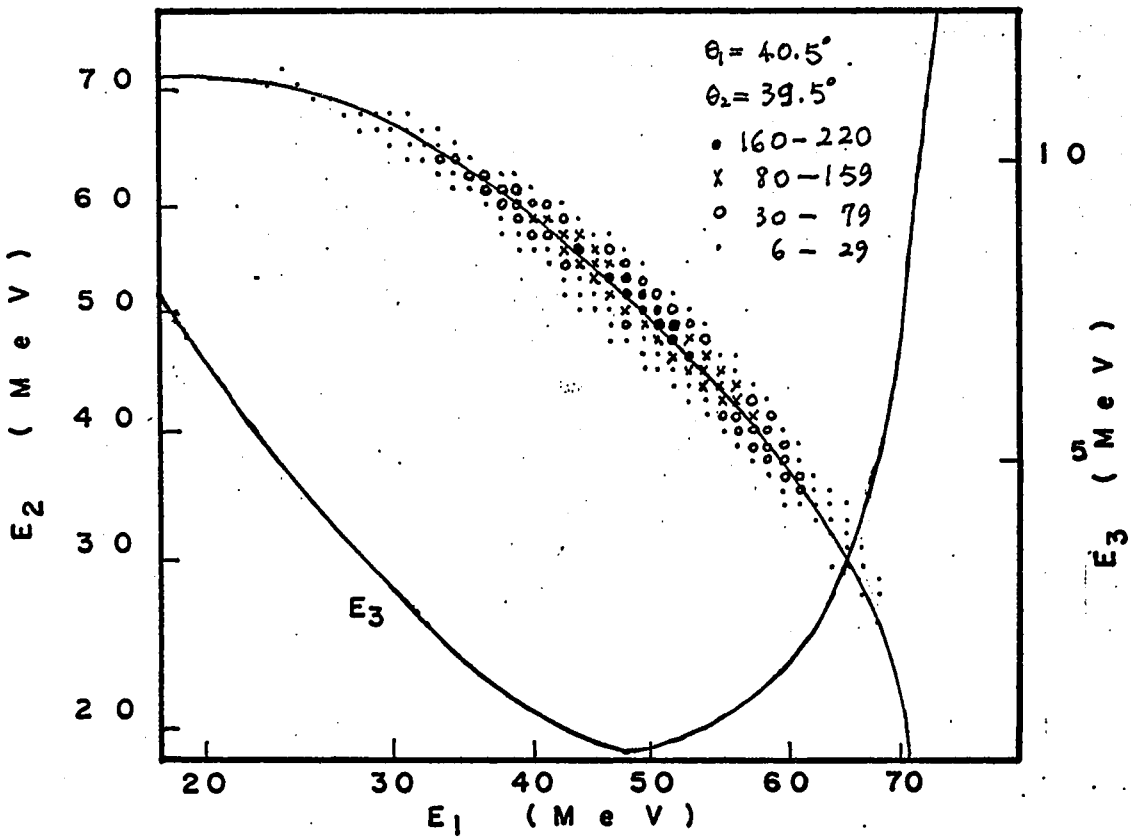
θ1 = 40.5°
θ2 = 39.5°
• 160-220
x 80-159
o 30-79
· 6-29
E3
E2 (MeV)
E3 (MeV)
E1 (MeV)
70
60
50
40
30
20
10
5
20
30
40
50
60
70

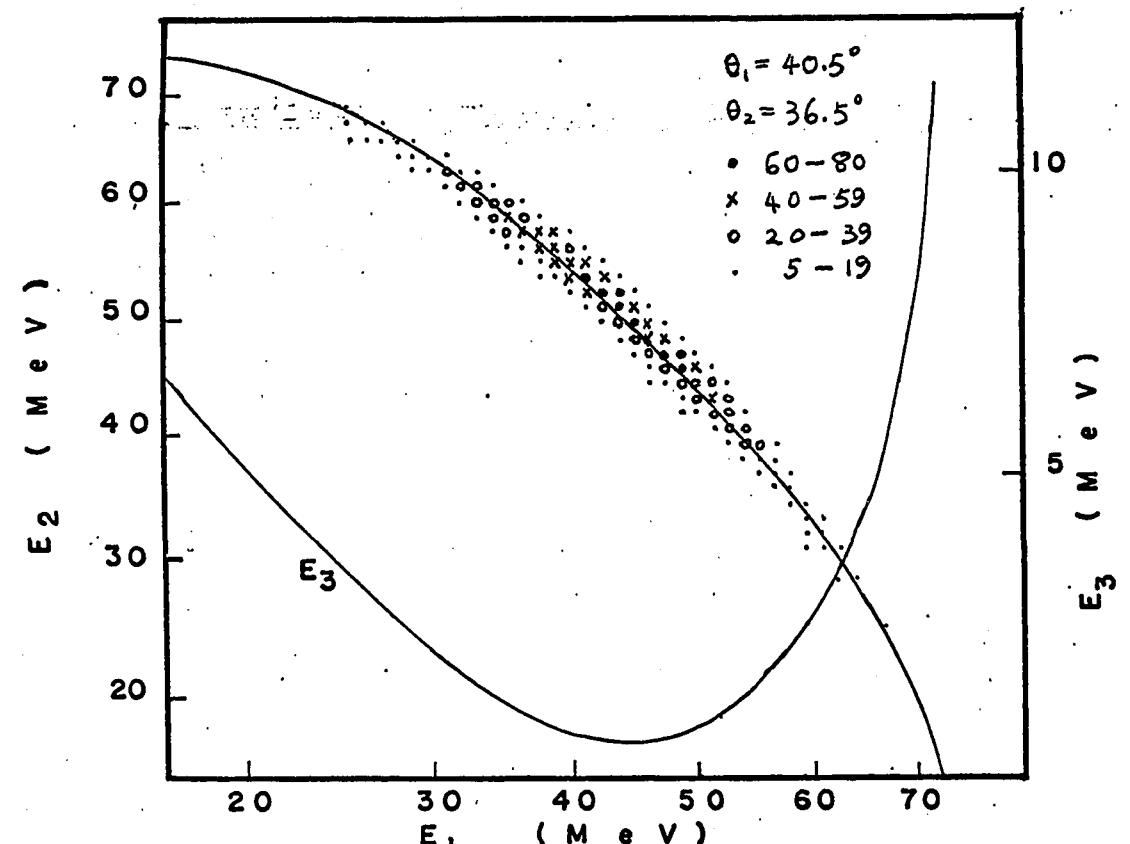
θ1 = 40.5°
θ2 = 36.5°
• 60-80
x 40-59
o 20-39
· 5-19
E3
E2 (MeV)
E3 (MeV)
E1 (MeV)
70
60
50
40
30
20
10
5
20
30
40
50
60
70

(d)

(e)

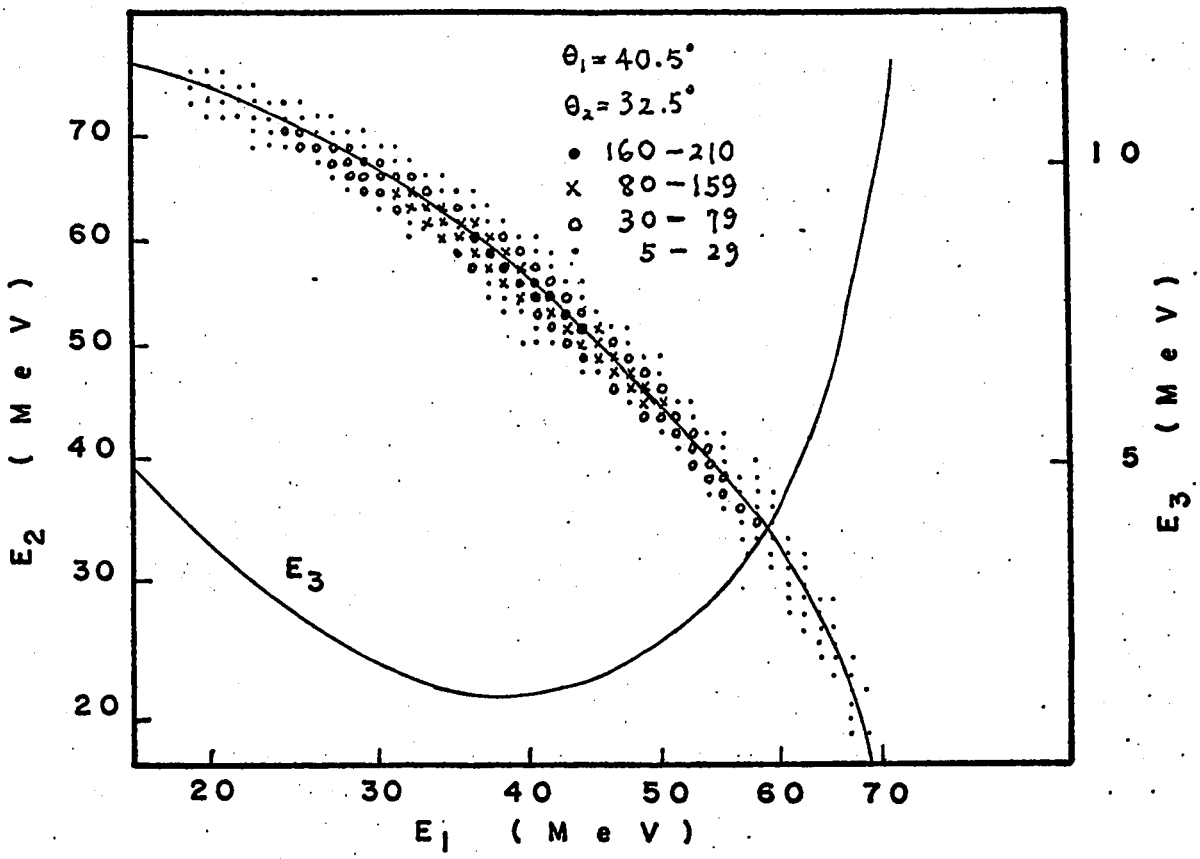
θ1 = 40.5°
θ2 = 32.5°
• 160 – 210
× 80 – 159
o 30 – 79
· 5 – 29
E3
E2 (MeV)
E3 (MeV)
E1 (MeV)
20
30
40
50
60
70
5
10

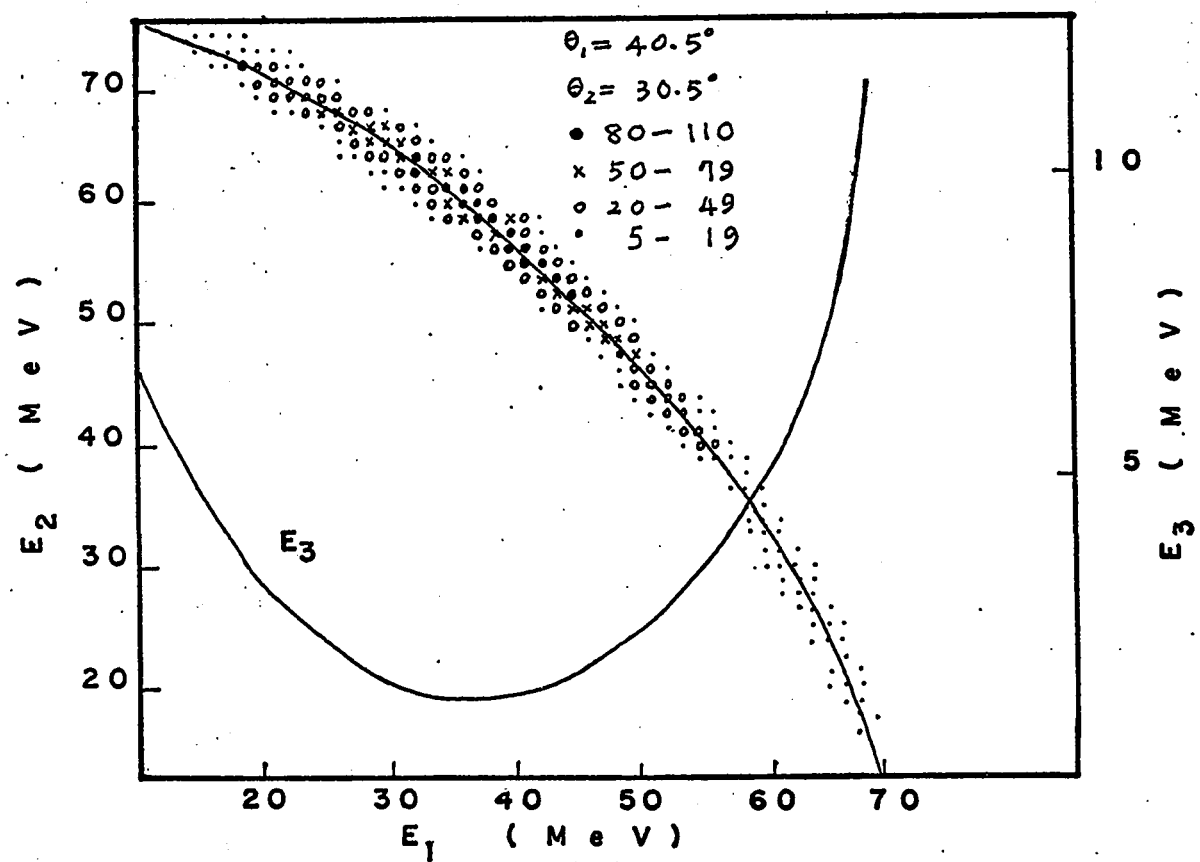
θ1 = 40.5°
θ2 = 30.5°
• 80 – 110
× 50 – 79
o 20 – 49
· 5 – 19
E3
E2 (MeV)
E3 (MeV)
E1 (MeV)
20
30
40
50
60
70
5
10

(f)

FIGURE 14 (a,b,c,d,e)

FIGURE 14 (a,b,c,d,e)

Plots similar to those of Figure 13, but with detector 1 fixed at 35.5^{o}. See the caption of Figure 13.

(a)

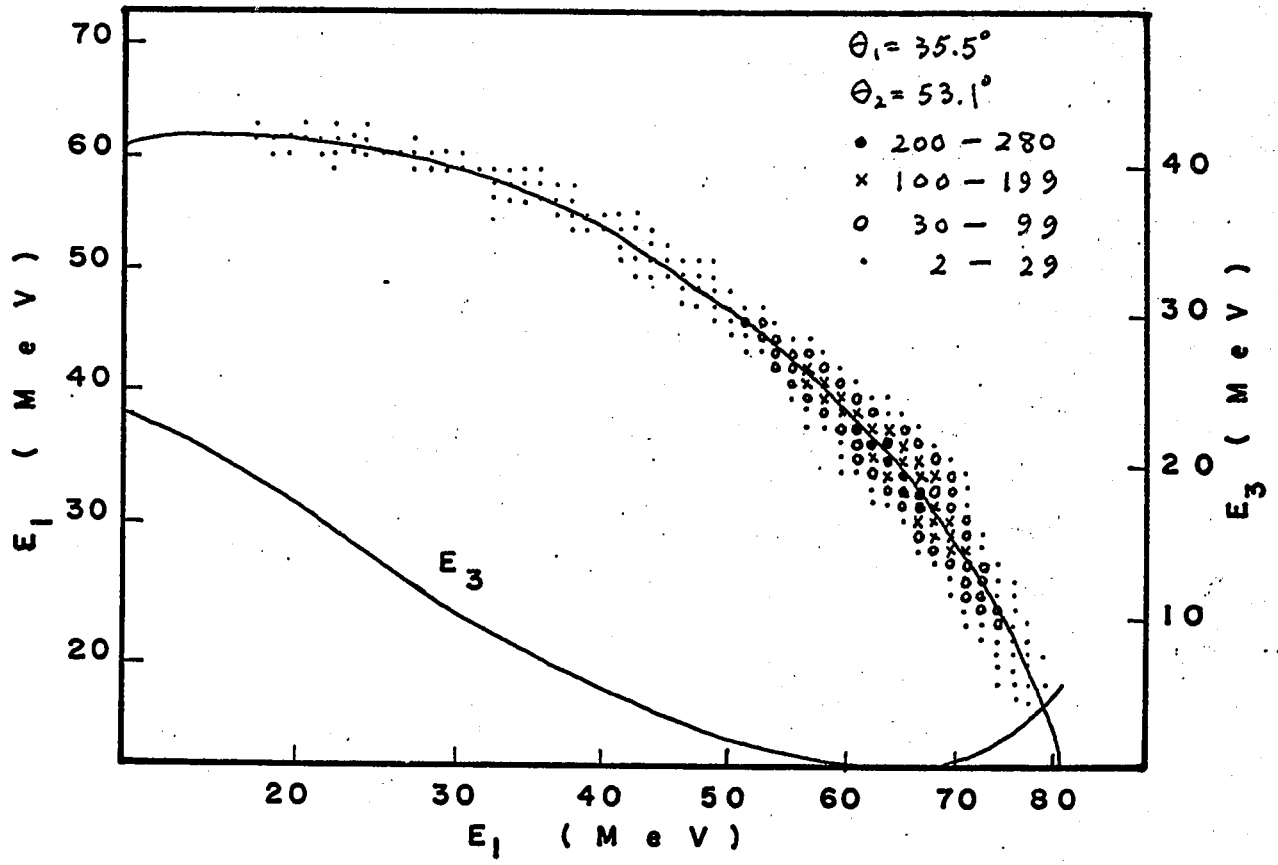
θ1 = 35.5°
θ2 = 53.1°
• 200 – 280
× 100 – 199
o 30 – 99
· 2 – 29
E3
E1 (MeV)
E3 (MeV)
70
60
50
40
30
20
40
30
20
10
20
30
40
50
60
70
80

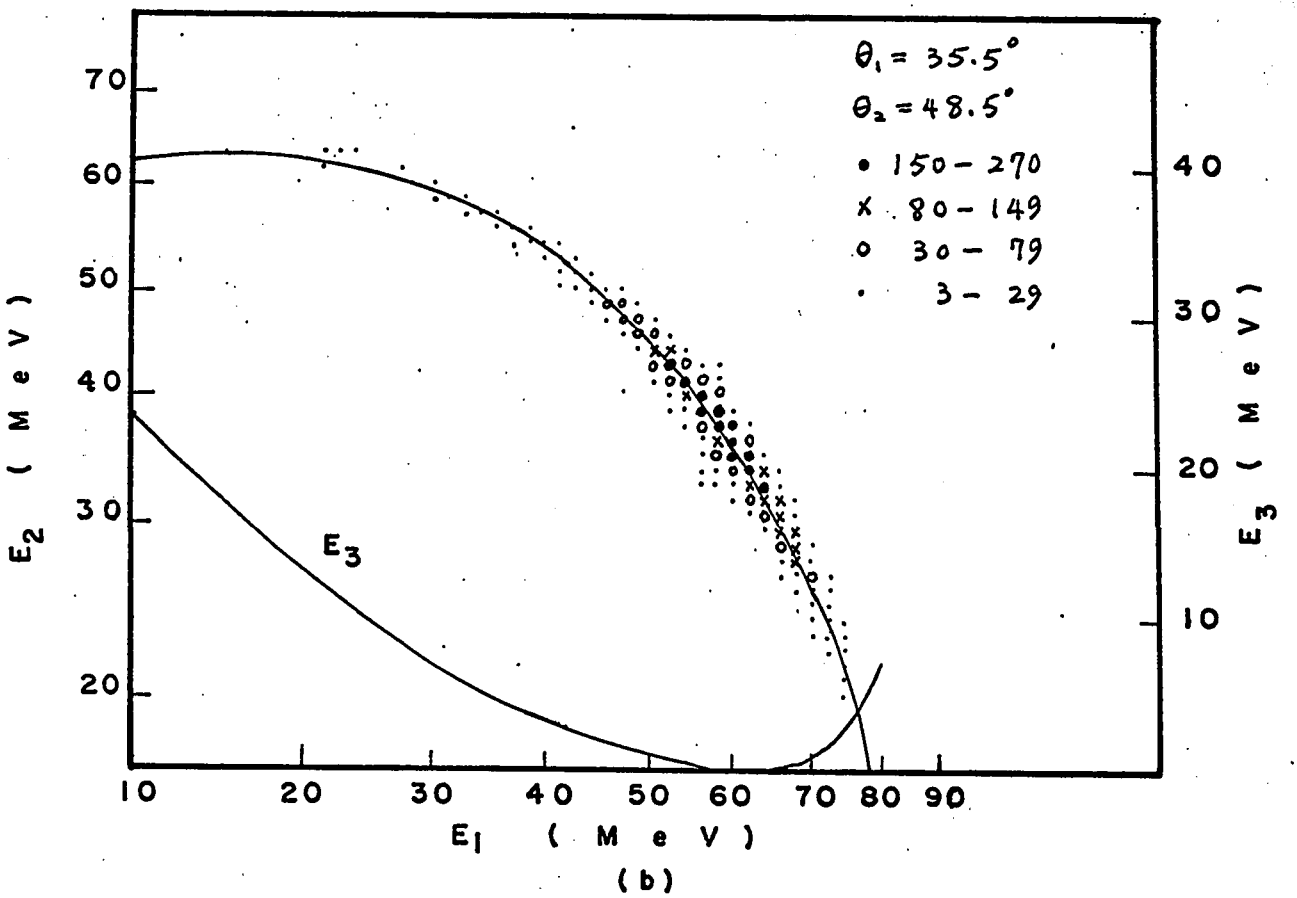
θ1 = 35.5°
θ2 = 48.5°
• 150 – 270
× 80 – 149
o 30 – 79
· 3 – 29
E3
E2 (MeV)
E3 (MeV)
70
60
50
40
30
20
40
30
20
10
10
20
30
40
50
60
70
80
90
E1 (MeV)

(b)

(c)

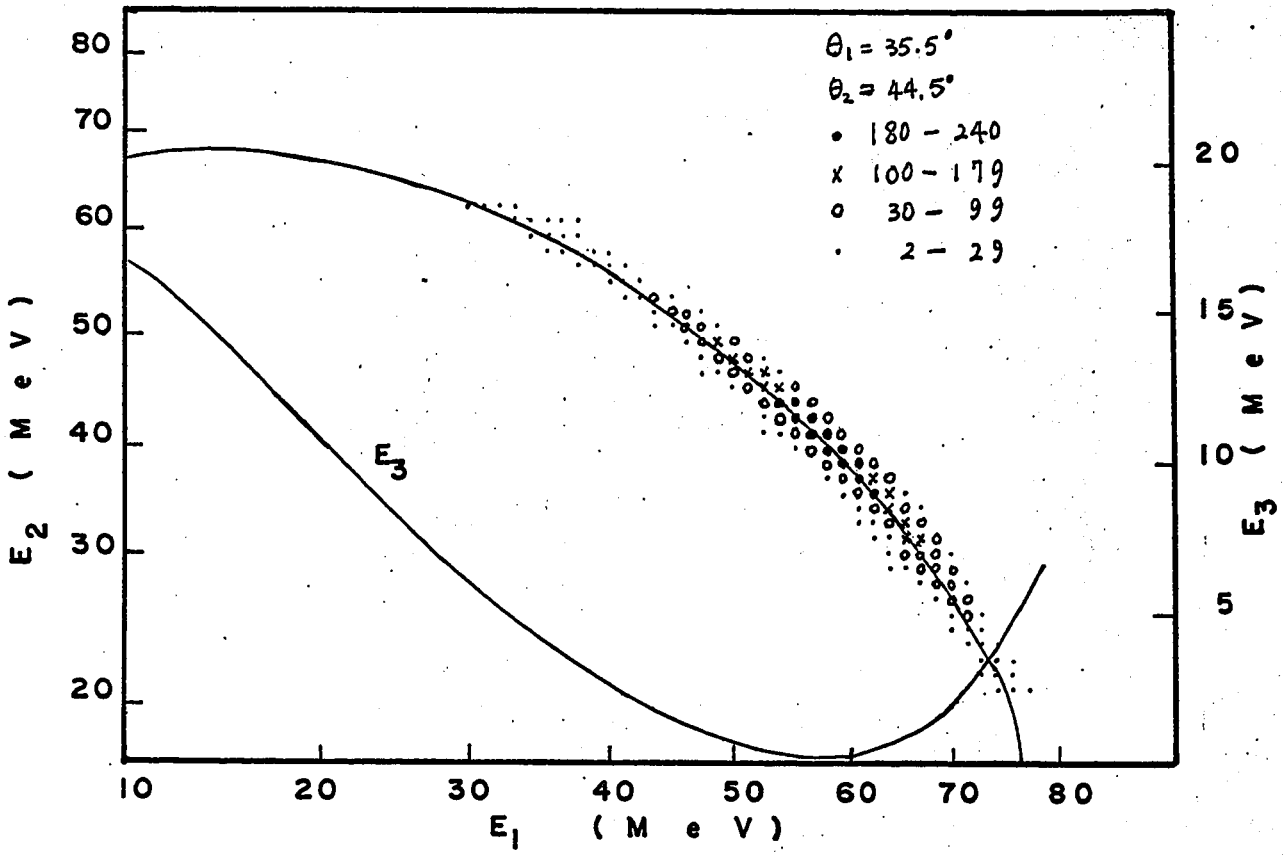
θ1 = 35.5°
θ2 = 44.5°
• 180 – 240
x 100 – 179
o 30 – 99
· 2 – 29
E3
E2 (MeV)
E3 (MeV)
E1 (MeV)
80
70
60
50
40
30
20
10
20
30
40
50
60
70
80
5
15

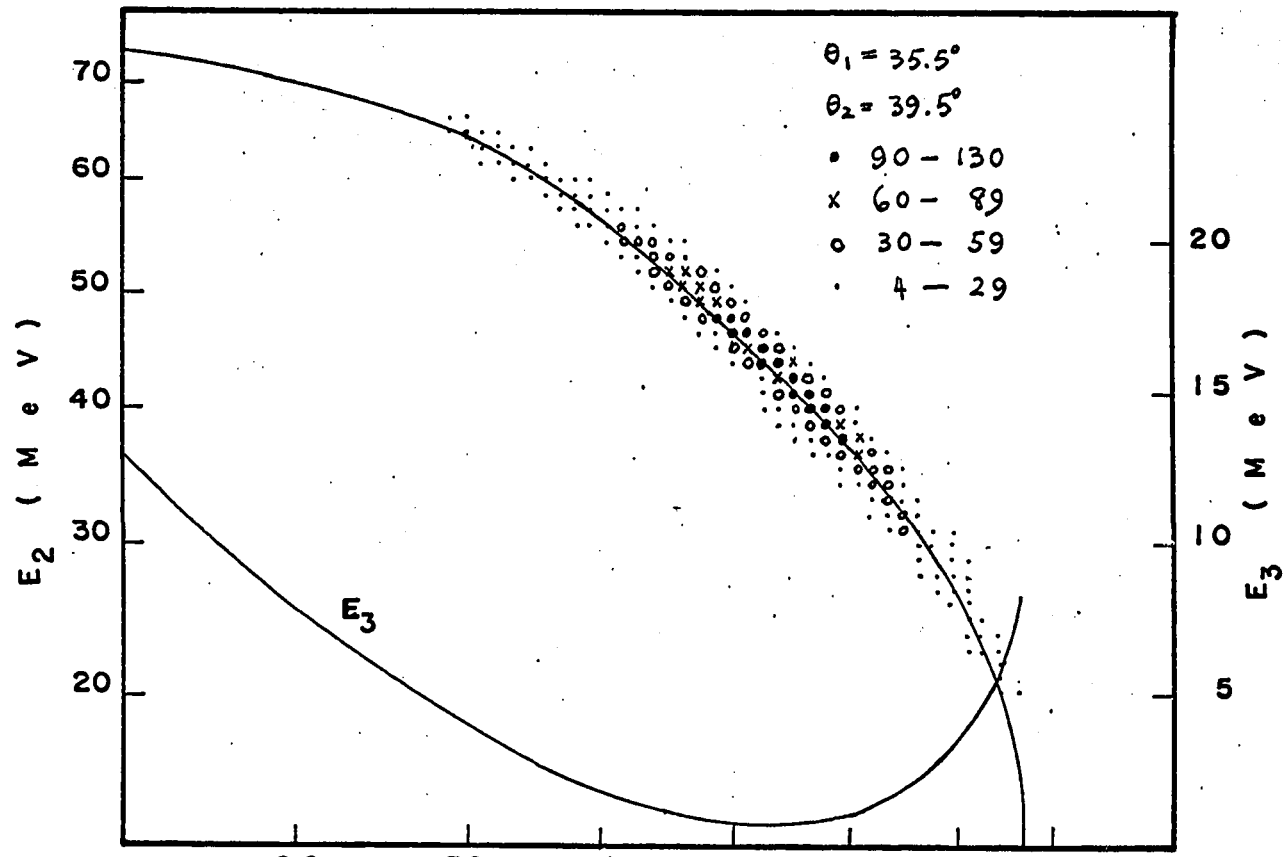
θ1 = 35.5°
θ2 = 39.5°
• 90 – 130
x 60 – 89
o 30 – 59
· 4 – 29
E3
E2 (MeV)
E3 (MeV)
E1 (MeV)
70
60
50
40
30
20
20
30
40
50
60
70
80
10
15

(d)

(e)

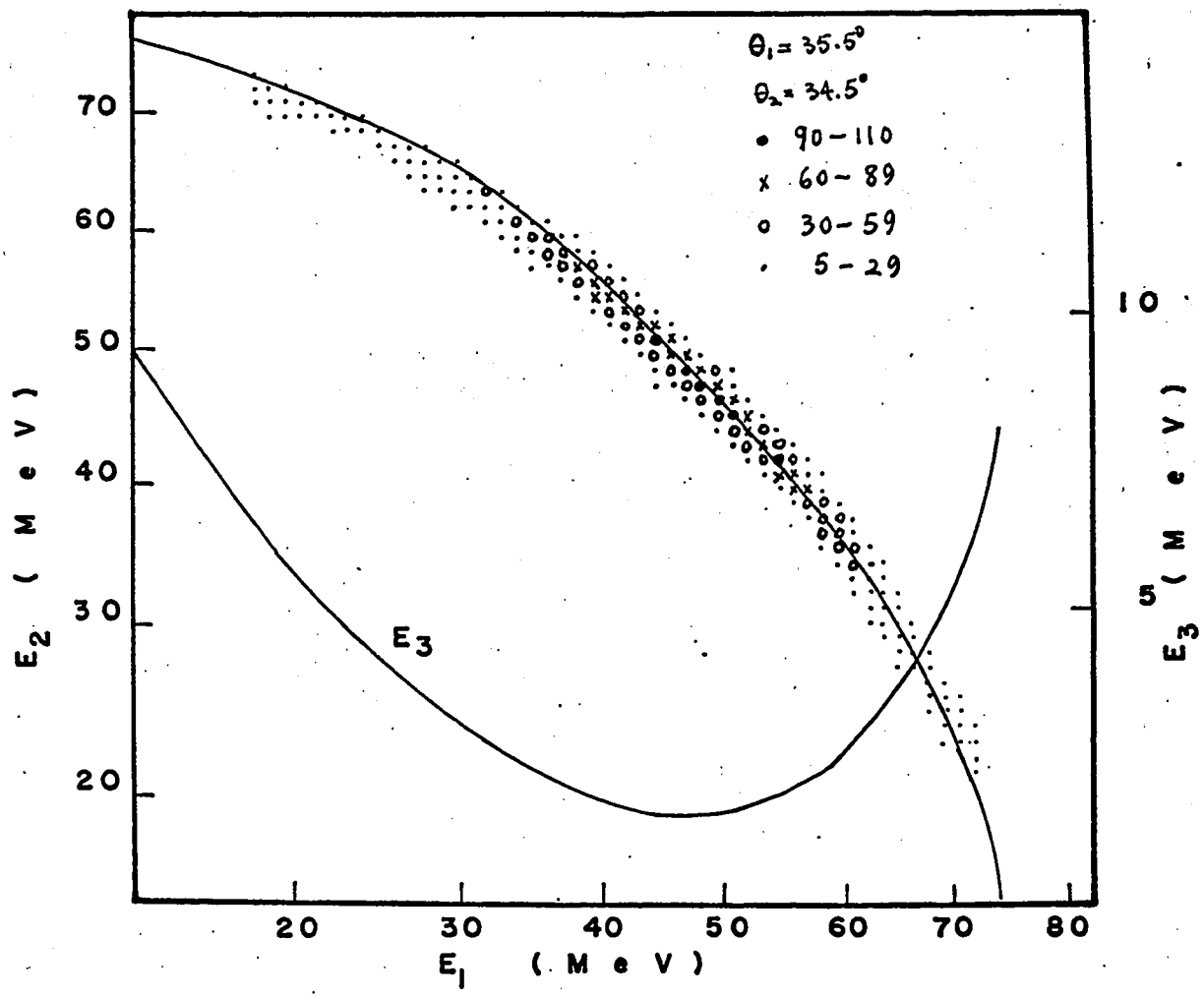
θ1 = 35.5°
θ2 = 34.5°
• 90 – 110
x 60 – 89
o 30 – 59
· 5 – 29
E3
70
60
50
40
30
20
10
5
E2 (M e V)
E3 (M e V)
20
30
40
50
60
70
80
E1 (M e V)

FIGURE 15 (a,b,c,d)

FIGURE 15 (a,b,c,d)

Two-parameter spectra for the D(p,2p)n reaction at 100 MeV. The curves labelled E_3 are the same as those in Figure 13, and 14. The curves labelled E^I_{23} represent values for the internal energy of the (23) system when the particle detected by the fixed detector 1 is the first emitted particle. Similarly the curves labelled E^I_{13} represent values for the internal energy of the (13) system when the first emitted particle is detected by detector 2, and the E^I_{12} curves correspond to that of the (12) system when the first emitted particle is the undetected neutron.

On each of diagrams 15c and d, there are two 3-body kinematic loci; one belongs to the reaction D(p,2p)n and the less prominent one belongs to the $^{12}C(p,2p)^{11}B$ reaction. Parts of the two loci on diagram 15d cannot be separated.

(a)

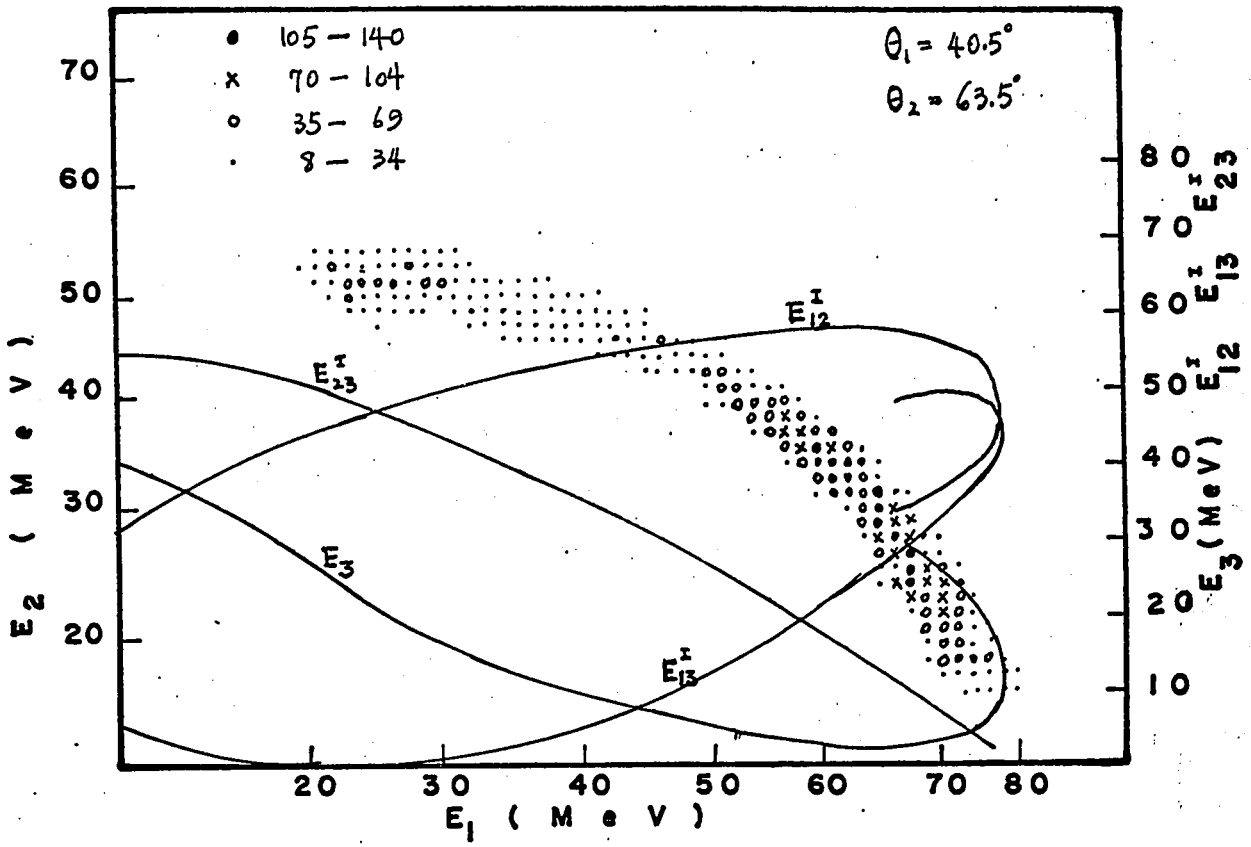
105 – 140
70 – 104
35 – 69
8 – 34
θ1 = 40.5°
θ2 = 63.5°
E12I
E23I
E3
E13I
E2 (MeV)
E3 (MeV) E13I E23I E12I
E1 (MeV)

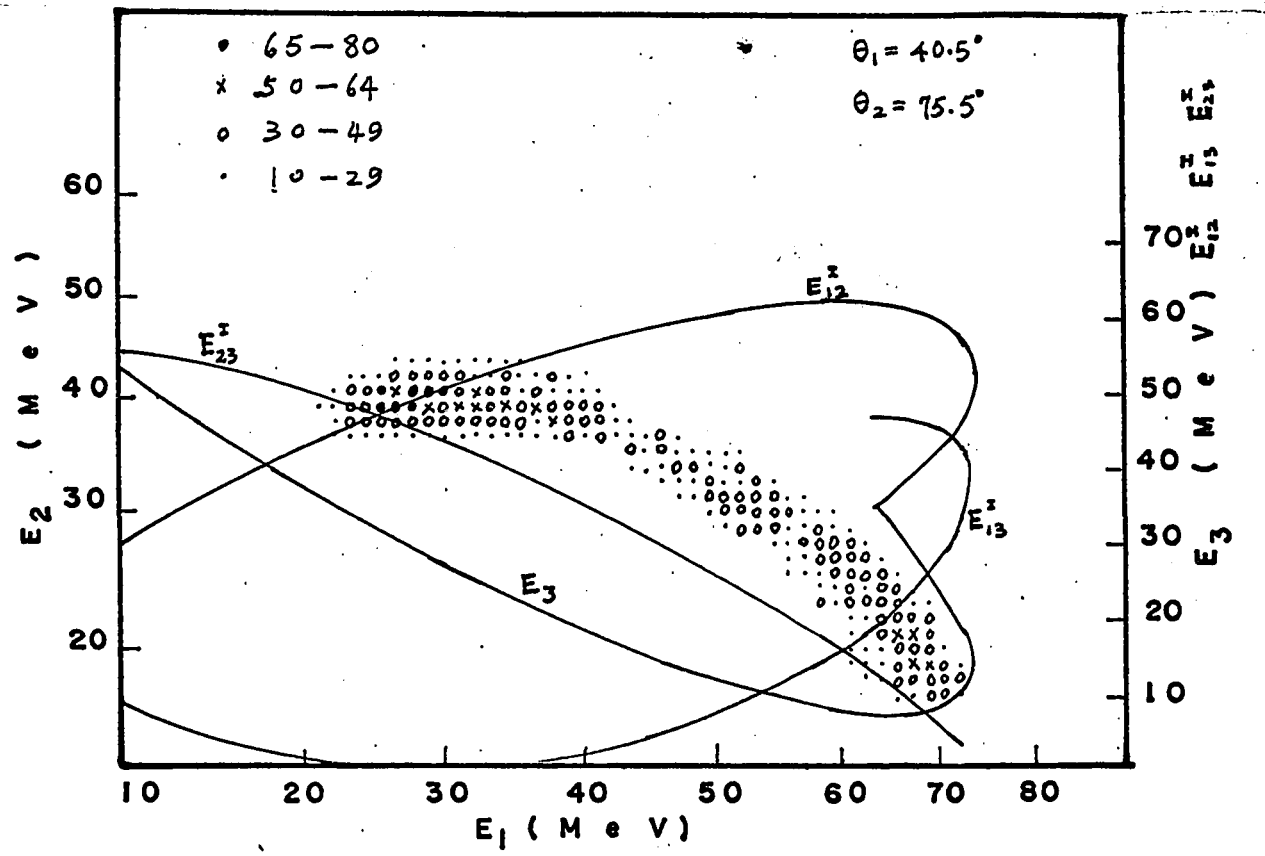
65 – 80
50 – 64
30 – 49
10 – 29
θ1 = 40.5°
θ2 = 75.5°
E12I
E23I
E13I
E3
E2 (MeV)
E3 (MeV) E13I E23I E12I
E1 (MeV)

(b)

(c)

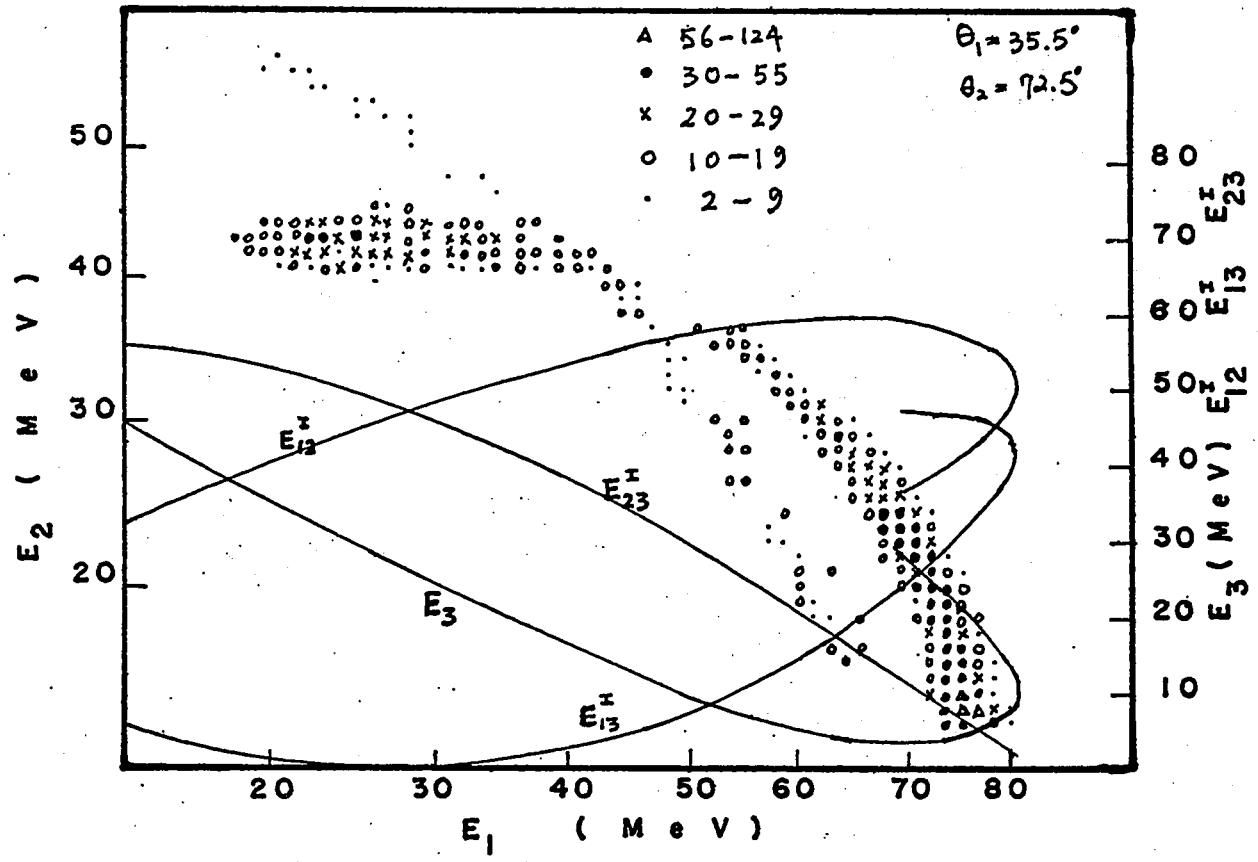
A 56-124
• 30-55
× 20-29
○ 10-19
· 2-9
θ1 = 35.5°
θ2 = 72.5°
E12^x
E23^I
E3
E13^I
E2 (MeV)
E3 (MeV) E12^I E13^I E23^I
E1 (MeV)
20
30
40
50
60
70
80
10

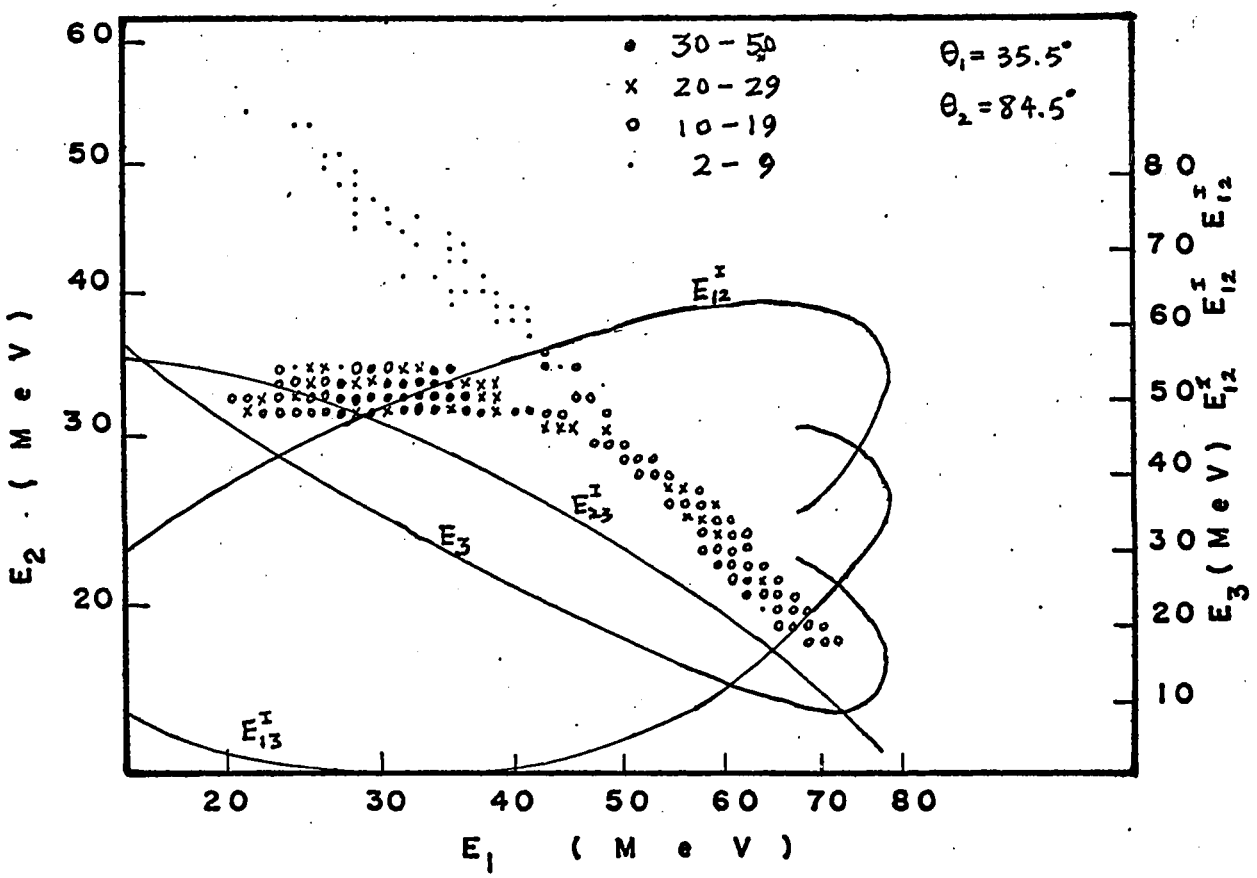
• 30-50
× 20-29
○ 10-19
· 2-9
θ1 = 35.5°
θ2 = 84.5°
E12^x
E23^I
E3
E13^I
E2 (MeV)
E3 (MeV) E12^I E12^x
E1 (MeV)
20
30
40
50
60
70
80
10

(d)

CHAPTER V. THEORETICAL ASPECTS

V - 1. IMPULSE APPROXIMATION AND SPECTATOR MODEL

V - 1a. Introduction.

In treating the scattering of a fast nucleon by a deuteron Chew (Ch-50) applied an approximation which has since been generalized to the scattering of an elementary particle by a complex nucleus (CG-52). This approximation is called the impulse approximation. However, in all the early papers it was used in a more specific sense, in that multiple scattering processes were omitted when the approximation was applied. For the analysis of the experimental data of proton-deuteron inelastic scattering at 145 MeV, Kuckes and his co-workers used the Born approximation to calculate the cross-section derived from the specific impulse approximation, and obtained a simple analytical expression for the differential cross-section (KWC-61). The Chew-Low extrapolation was then applied (CL-59). This procedure will here be called the spectator model. In the paragraphs following, a brief description of the impulse approximation and the spectator model will be given. The original derivations, and details of the approximation can be found in a series of papers contributed by Chew, Wick, Ashkin, Goldberger and Kuckes et al. (Ch-50, Ch-51, CW-52, AW-52, CG-52, KWC-61).

V - 1b. Formalism

Let the total Hamiltonian of the (p,D) system be H, and let

H_o be the "unperturbed" Hamiltonian i.e. the sum of K, the total kinetic energy operator of the system and U, the nuclear potential energy. Mathematically

$$H = H_o + V$$

$$H = K + U$$

where V represents the interaction between the incident proton and the target. Adopting the Lippmann and Schwinger formalism (LS-50), Ψ_a, the exact solution of the equation

$$H \Psi_a = E_a \Psi_a$$

can be written as

$$\Psi_a = \Phi_a + \frac{1}{E_a + i\eta - H_o} V \Psi_a \qquad (\eta>0,\ \eta\to 0) \qquad (1)$$

where Φ_a is the exact solution of

$$H_o \Phi_a = E_a \Phi_a$$

More specifically Φ_a is the product of an incident plane wave in the incident particle's coordinates and a bound state function in the target coordinates. The matrix element of the well known T operator is given by

$$T_{ba} = (\Phi_b , V \Psi_a) = (\Phi_b , T \Phi_a) \qquad (2)$$

between the initial state a and final state b. Its square is essentially the transition probability of interest. From (1) it is evident

that

$$T = V + V \frac{1}{E_a + i\eta - H_o} T \qquad (3)$$

and with some algebraic manipulation of operators, (3) becomes

$$T = V + V \frac{1}{E_a + i\eta - H} V$$

Similarly for the free two body scattering

$$(K + V) \psi_n = E_n \psi_n$$

the exact solution ψ_n is

$$\psi_n = \chi_n + \frac{1}{E_n + i\eta - K} V \psi_n$$

where χ_n is an eigenfunction of the kinetic operator T. The corresponding t operator and its matrix are

$$t = V + V \frac{1}{E_n + i\eta - k - V} V$$

and $$t_{mn} = (\chi_m , V \psi_n)$$

The impulse approximation says that T in (2) is replaced by t, or Ψ_a is replaced by Ψ_a^I, i.e. the transition matrix element becomes

$$M_{ba}^{(I)} = (\Phi_b , t \Phi_a)$$

and

$$\Psi_a^I = \sum_n \psi_n (\chi_n , \Phi_a) \qquad (4)$$

because

$$t \Phi_a = \sum_{m,n} \chi_m t_{mn} (\chi_n , \Phi_a) = V \sum_n \psi_n (\chi_n , \Phi_a)$$

The physical meaning of the approximated wave function Ψ_a^I is very clear: it represents the scattering of an incident wave by a wave packet of the free target particle, which possesses the same momentum distribution as it does when bound in the deuteron. Under such an approximation, the other particle left in the deuteron behaves as a "spectator". If the neutron of the deuteron is a spectator, we can more explicitly write

$$\Psi_a^I = \iint d\vec{p}_2\, d\vec{p}_3\; G_0(\vec{p}_2, \vec{p}_3) e^{\frac{i}{\hbar}\vec{p}_3\cdot\vec{r}_3}\; \psi^{pp}_{\vec{p}_0,\vec{p}_2}(\vec{r}_1, \vec{r}_2)$$

where

$$G_0(\vec{p}_2, \vec{p}_3) = \iint d\vec{r}_2\, d\vec{r}_3\; e^{-\frac{i}{\hbar}(\vec{p}_2\cdot\vec{r}_2 + \vec{p}_3\cdot\vec{r}_3)}\, \varphi_0(\vec{r}_2 - \vec{r}_3)$$

$\psi^{pp}_{\vec{p}_0,\vec{p}_2}(\vec{r}_1,\vec{r}_2)$ represents the free p-p scattering.

$\vec{p}_0, \vec{p}_2, \vec{p}_3$ are the momenta of the incident proton, the target proton and the neutron, respectively.

φ_0 is the deuteron ground state wave function.

Kuckes et al. used plane waves to stand for $\psi^{pp}_{\vec{p}_0,\vec{p}_2}(\vec{r}_1,\vec{r}_2)$ and Φ_b ; the matrix element therefore was written as

$$M^I = \iiint \exp\tfrac{i}{\hbar}(\vec{p}_0 - \vec{p}_1 - \vec{p}_2 - \vec{p}_3)\cdot\vec{r}_2\; d\vec{r}_2\; V(\vec{p}_0 - \vec{p}_1)\,\phi(\vec{p}_3)$$

The cross-section in the laboratory system is then

$$\frac{d^3\sigma}{d\Omega_1 d\Omega_2 dE_1} = \frac{2\pi}{\hbar}\,\frac{m^2}{p_0}\,\frac{1}{(2\pi\hbar)^6}\,|\phi(p_3)|^2\,|V(\vec{p}_0 - \vec{p}_1)|^2 \frac{p_2^2\, p_1}{2p_2 - p_0\cos\theta_2 + p_2\cos\theta_{12}} \qquad (5)$$

which are the eq. (2) and (4) of the reference, (KWC-61). The final analytic expression for the differential cross-section was expressed by them as

$$\frac{d^3\sigma}{d\Omega_1 d\Omega_2 dE_1} = \frac{4\sqrt{2}}{\pi^3}\frac{\sqrt{E_\alpha E_\beta}}{(E_\alpha+2E_3)^2}\frac{(\sqrt{E_\alpha}+\sqrt{E_\beta})^3}{(E_\beta+2E_3)^2}\frac{1}{\sqrt{E_0}}\frac{\sqrt{E_1}\,E_2\left(\frac{d\sigma}{d\Omega}\right)_{free,cm}}{2\sqrt{E_2}-\sqrt{E_0}\cos\theta_2+\sqrt{E_1}\cos\theta_{12}} \qquad (6)^*$$

where E_1, E_2, E_3 are the kinetic energies of the outgoing particles.

E_0 is the kinetic energy of the incident proton.

E_α = 2.226 MeV (the binding energy of the deuteron).

E_β = 59.8 MeV.

$\left(\frac{d\sigma}{d\Omega}\right)_{free,cm}$ = free p-p differential scattering cross-section in the CM system.

Equation (6) was derived by use of the Hulthén wave function and was done non-relativistically.

V - 1c. Assumptions

Chew and Goldberger were able to separate the T operator into three terms: the first one is the operator t, the second term vanishes when U vanishes, and the third term is independent of U (CG-52). The third term vanishes when there is only one target particle instead of two for the case of the deuteron. It is clear that multiple scattering is involved in the third term. The replacement of T by t means that the second and third terms are neglected, and this omission corresponds to three assumptions. The omission of the second term requires an assumption that the binding force has a negligible effect when the incident particle interacts strongly with the target system. The omission of the third term requires two further assumptions:

I, the incident particle interacts strongly with only one of the two target particles at the same time, and

* This expression contained misprints in the original publication; these have been corrected here.

II, the amplitude of the incident particle is not appreciably perturbed by the presence of the target particle other than the one which interacts strongly with the incident particle.

Roughly the validity of the assumption concerning the binding force depends on the short "collision" time. This means that the ratio of the collision time to the period of the deuteron must be small. As a rough estimate of this ratio, one could treat the high energy nucleon-nucleon total scattering cross-section as "geometrical" to define the scattering range, ρ , by $\pi\rho^2 = \sigma^{Total}$. For $\sigma^{Total} = 4 \times 10^{-26} cm^2$ the ratio is about 1/10 at 100 MeV incident proton energy. Assumption I holds when $\bar{R}$, the average distance between the two nucleons of the deuteron is large compared to ρ . For the deuteron $\bar{R} = 3.2 \times 10^{-13}$ cm which is considerably larger than $\rho \simeq 1.1 \times 10^{-13}$cm. The wave length of the incident proton at 100 MeV ($\lambda\!\!\!^{-} = 4.2 \times 10^{-14}$cm) is also small compared to $\bar{R}$; assumption II is then appropriate for a deuteron target.

V - 1d. Chew-Low Extrapolation

In studying how to extract information of the scattering cross-section for a collision between an incident particle and a particle which is contained in a complex target system, Chew and Low (CL-59) pointed out that there is a second order pole of eq. (6) at $E_3 = -\frac{E_\alpha}{2}$. In this unphysical situation there is no binding effect so that there is no uncertainty in the replacement of $\left|V(\vec{P}_o - \vec{P}_1)\right|^2$ by the corresponding free proton-proton scattering potential. They

proposed to plot the ratio of experimental differential cross-section to that of eq. (6) vs. $\bar{E}_3$, and then extrapolate the curve to $\bar{E}_3 = -\frac{E_\alpha}{2}$ in the unphysical region. The ratio there should be unity. They suggested keeping the scattering angle in the center of mass system constant. As this cannot be easily carried out experimentally, the laboratory angle θ_1 was kept constant instead for the experiment. Moreover the counting statistics are not good enough to perform an extrapolation on $\frac{d^3\sigma}{dE_1\, d\Omega_1\, d\Omega_2}$, so the procedure was carried out for $\frac{d^2\sigma}{d\Omega_1\, d\Omega_2}$.

The theoretical value of $\frac{d^3\sigma}{dE_1\, d\Omega_1\, d\Omega_2}$ first must be integrated over the finite solid angles subtended by the two collimators of the detector assemblies; then the area under the theoretical curve was taken as $\left(\frac{d^2\sigma}{d\Omega_1\, d\Omega_2}\right)_{theor.}$ The ratio desired, R, is then the value of $\left(\frac{d^2\sigma}{d\Omega_1\, d\Omega_2}\right)_{theor.}$ divided by the area under the experimental curve of $\left(\frac{d^3\sigma}{\Delta E_1\, \Delta\Omega_1\, \Delta\Omega_2}\right)_{exp.}$. Mathematically

$$R = \frac{\int_{E_1}\int_{\Delta\Omega_1}\int_{\Delta\Omega_2} \left(\frac{d^3\sigma}{dE_1\, d\Omega_1\, d\Omega_2}\right)_{theor.} dE_1\, d\Omega_1 d\Omega_2}{\int_{\bar{E}_1} \left(\frac{\Delta^3\sigma}{\Delta E_1\, \Delta\Omega_1\, \Delta\Omega_2}\right)_{exp.} \Delta E_1}$$

The average value of E_3 was obtained by using $\left(\frac{d^3\sigma}{dE_1\, d\Omega_1\, d\Omega_2}\right)_{theor.}$ as a weighting factor. The extrapolation was then performed by extending the curve R v.s. $\bar{E}_3 = -\frac{E_\alpha}{2}$. It is evident that to make the procedure feasible, the values of $\bar{E}_3$ must be as close to zero as possible. The effect caused by folding in the finite solid angles is

significant to spectra of a pair of angles whose sum is close to 90^{o}.

V - 2. THE GENERALIZED DENSITY OF STATES FUNCTION

V - 2a. Introduction

As mentioned in section IV - 1, there are two possible types of reaction mechanism (simultaneous, and sequential) through which a complex target system can be broken up by an incident particle. Besides the transition matrix element, effects caused by the reaction mechanism also contribute to the reaction cross-section. For the purpose of interpreting experimental data their effects should be well understood.

V - 2b. Phase Space

Suppose that the probability of simultaneous break-up is proportional to the total phase space available. The phase space problem has been studied in some respects in detail (B-56, BO-58). Here the differential phase space volume appropriate to our experimental set up will be given. Details are shown in Appendix B.

The relativistic total phase space integral for three particles in the final state is proportional to

$$\iiint \delta(E_o + E_T - E_1 - E_2 - E_3)\ \delta(\vec{p}_o - \vec{p}_1 - \vec{p}_2 - \vec{p}_3)\ d\vec{p}_1\ d\vec{p}_2\ d\vec{p}_3$$

where E_o, E_T are the total energies of the incident particle and the target, respectively.

E_1, E_2, E_3 are the total energies of the outgoing particle 1, 2, and 3, respectively and p_1, p_2, p_3 are their corresponding momenta.

The integrand may be integrated over $\vec{p}_3$ and the magnitude of $\vec{p}_2$, giving the following result:

> The probability of detecting particle 1 in the differential solid angle $d\Omega_1$ with a momentum between p_1 and $p_1 + dp_1$, while particle 2 is accepted within the differential solid angle $d\Omega_2$ is proportional to

$$\frac{E_1 E_2 E_3 P_1 P_2}{(E_2+E_3) + E_2 \frac{(\vec{P}_1 - \vec{P}_0)\cdot\vec{P}_2}{P_2^2}} \qquad (7)$$

All the variables in eq. (7) are expressed in the laboratory system, and are relativistically exact. When eq. (7) is used in the analysis of experimental data, it is integrated over the finite solid angles subtended by the collimators of the detector assemblies. However, it was found that the general features of a phase space curve are not changed by this integration.

V - 2c. Sequential Break-up and Density-of-States Function

Details of this section can be found in a number of references (S-65, PGB-60, PGB-61, SJP-67). Only a brief outline will be given here. The notations of (S-65) are adopted here.

Consider the following reaction, which proceeds in different ways, sequentially:

$$A + B \rightarrow N^* \longrightarrow C + (D,E) \longrightarrow C + D + E \qquad (8)$$

$$\longrightarrow D + (C,E) \longrightarrow C + D + E \qquad (9)$$

$$\longrightarrow E + (C,D) \longrightarrow C + D + E \qquad (10)$$

The systems (D,E), (C,E), and (C,D) represent localized states of radius a_1, a_2, a_3 respectively, with internal energies E_1, E_2, and E_3, respectively. Phillips and his co-workers wrote down the cross section for reaction (8) as

$$\sigma(E_1, a_1) = \frac{\mu_A \mu_c k_c}{4\pi^2 \hbar^4 K_A} \left| \langle (DE) + C, E_1 | H_1 | A + B, E_A \rangle \right|^2 \rho_1(E_1, a_1)$$

where $\rho_1 (E_1, a_1)$ is the generalized density-of-states function. For systems which have only sharp particle-bound states of eigenvalues E_n, ρ_1 reduces to

$$\sum_n \delta (E - E_n)$$

For systems which possess a continuum state as well, they argued that the probability for the first emission of C, to produce a continuum state (D,E) is proportional to the probability that D and E be localized within a nuclear volume of radius a_1. The generalized density-of-states function is defined as

$$\rho_1 (E_1, a_1) = \rho_0 (E_1) N^2 (E_1)$$

where $N(E_1)$ is the normalization constant of the wave function ψ (the final state wave function of the relative motion for the (D,E) system)

$$\psi = N(E_1) \frac{U(E_1, r)}{r} Y_\ell^m (\eta_D^{(1)}, \epsilon_D^{(1)})$$

and $\rho_0 = \frac{\mu R}{\pi \hbar^2 K_1}$ is the usual density-of-states function. R is the radius of normalization for ψ. After ψ has been properly renormalized, the general form of the GDS function for the ℓ^{th} particle wave

is $$\rho_\ell(E_1, a_1) = \frac{\mu_D}{\pi\hbar^2 K_D}\left[\frac{d}{dk_D}(\delta_\ell + \varphi_\ell) - \frac{1}{2}\left(\frac{1}{K_D} - \frac{2\frac{\partial A_\ell}{\partial K_D}}{A_\ell}\right)\sin 2(\delta_\ell+\varphi_\ell)\right.$$
$$\left. - \frac{1}{k_D}\left(A_\ell \frac{\partial^2 A_\ell}{\partial r \partial K_D} - \frac{\partial A_\ell}{\partial r}\cdot\frac{\partial A_\ell}{\partial k_D}\right)\sin^2(\delta_\ell+\varphi_\ell)\right]$$

where $A_\ell = F_\ell^2 + G_\ell^2$ with $F_\ell(E_1, a_1)$ and $G_\ell(E_1, a_1)$ being the regular and irregular wave solutions to the scattering equation of the (D,E) system, and φ_ℓ is the hard core phase shift. For a neutron-proton system with $U(r \leq a_1)$ being independent of the energy

$$\rho_\ell(E_1, a_1) = \frac{2\mu_D a_1}{\pi\hbar^2 \xi^2}\,\frac{\sin^2(\delta_\ell + K_1 r)}{K_1 r}$$

where $\xi = U_\ell(E_1, a_1)$

When the complications of kinematics due to three equal mass particles in the final state and of different systems of reference are taken into account, the differential cross-section of interest is written as

$$\frac{d^3\sigma}{d\Omega_1 d\Omega_2 dE_1} = \frac{1}{2\pi}\left\{ A_1^2 \rho_1(E_1, a_1)\frac{M_A M_C K_C}{4\pi^2\hbar^4 K_A}\left|\langle (DE)+C, E_1 | H_1 | A+B, E_A\rangle\right|^2 J_1\right.$$
$$+ A_2^2 \rho_2(E_2, a_2)\frac{M_A M_D K_D}{4\pi^2\hbar^4 K_A}\left|\langle (CE)+D, E_2 | H_2 | A+B, E_A\rangle\right|^2 J_2 \quad (11)$$
$$\left. + A_3^2 \rho_3(E_3, a_3)\frac{M_A M_E K_E}{4\pi^2\hbar^4 K_A}\left|\langle (CD)+E, E_3 | H_3 | A+B, E_A\rangle\right|^2 J_3\right\} J_L$$

where the angular distributions in the recoil two-nucleon system are taken to be $\frac{1}{4\pi}$ — i.e. isotropic. J_1, J_2, and J_3 are the Jacobians for transformation from the two-nucleon recoil center-of-mass system (RCM) to the total center-of-mass system, (SCM) and J_L is the transformation Jacobian from the SCM to the laboratory system. A_1^2, A_2^2, A_3^2 are the angular distributions in the SCM system.

The description above has ignored the interference between the various mechanisms and that between different ways of the same mechanism, i.e. the sequential mechanism.

V - 2d. Numerical Calculation

The generalized density-of-states functions were calculated for the singlet and triplet neutron-proton systems for relative energies below 2.5 MeV. They are shown in Fig. 15, and 16. The phase shift needed was calculated from the effective range theory (Be-49). For an actual experimental spectrum there is always some portion where the corresponding internal energies of an (n,p) system are too high to apply the effective range theory. As some of the latest data on singlet and triplet nucleon-nucleon phase shifts (Pe-67, Ho-67, KLJ-67, Br-67) agree with those of Yale's YRBI search (BHLP-60) and Yale's YLAN3 search (HLRB-61), the latter were used for high internal energies and extrapolated back to the low energy region to match with the phase shifts calculated by the effective range theory.

The explicit forms for the Jacobians in eq. (11) are written below

$$J_1 = \frac{\partial(E_{1\text{-}23}, \Omega_{1\text{-}23}, \Omega_{2\text{-}3})}{\partial(E_1^c, \Omega_1^c, \Omega_2^c)} = \frac{M}{m_2} \frac{(P_2^c)^2}{P_{2\text{-}3}} \frac{1}{A P_2^c + P_1^c \cos\theta_{12}^c}$$

$$J_2 = \frac{\partial(E_{2\text{-}13}, \Omega_{2\text{-}13}, \Omega_{1\text{-}3})}{\partial(E_1^c, \Omega_1^c, \Omega_2^c)} = \frac{M}{m_2} \frac{P_1^c P_2^c}{P_{1\text{-}3}} \frac{1}{\frac{1}{A} P_2^c + P_1^c \cos\theta_{12}^c} \qquad (12)$$

$$J_3 = \frac{\partial(E_{3\text{-}21}, \Omega_{3\text{-}21}, \Omega_{2\text{-}1})}{\partial(E_1^c, \Omega_1^c, \Omega_2^c)} = \frac{M}{m_3} \frac{P_1^c (P_2^c)^2}{P_3^c P_{2\text{-}1}} \frac{1}{\frac{1}{m_1+m_2}(m_1 P_2^c - m_2 P_1^c \cos\theta_{12}^c)}$$

$$J_4 = \frac{\partial(E_1^c, \Omega_1^c, \Omega_2^c)}{\partial(E_1^d, \Omega_1^d, \Omega_2^d)} = \frac{P_1^d (P_2^d)^2}{P_1^c (P_2^c)^2} \frac{A P_2^c + P_1^c \cos\theta_{12}^c}{A P_2^d + P_1^d \cos\theta_{12}^d - P^d \cos\theta_2^d}$$

where $A = \frac{m_1 + m_2}{m_2}$, $M = m_1 + m_2 + m_3$

P_{i-jk} is the momentum of the first outgoing i^{th} particle with respect to the recoil center of mass system of (j,k); (ijk) = permutation of (123)

P_{j-k} is the relative momentum of the (j,k) system in their center of mass system.

E_{i-jk} and E_{j-k} are the corresponding kinetic energies of P_{i-jk} and P_{j-k}

P_i^c is the momentum of the i^{th} particle in the total center-of-mass system.

P_i^g is the momentum of the i^{th} particle in the laboratory system.

θ_{12}^c is the sum of the scattering angles of particle 1 and 2 in their total center-of-mass system.

θ_{12}^g is that corresponding to θ_{12}^c, but in the laboratory system.

More details of (12) will be given in Appendix C. In deriving eq. (12) some basic formula were used from (Oh-65).

FIGURE 16

FIGURE 16

Density-of-states for the singlet neutron-proton system. The parameters used are shown in the diagram.

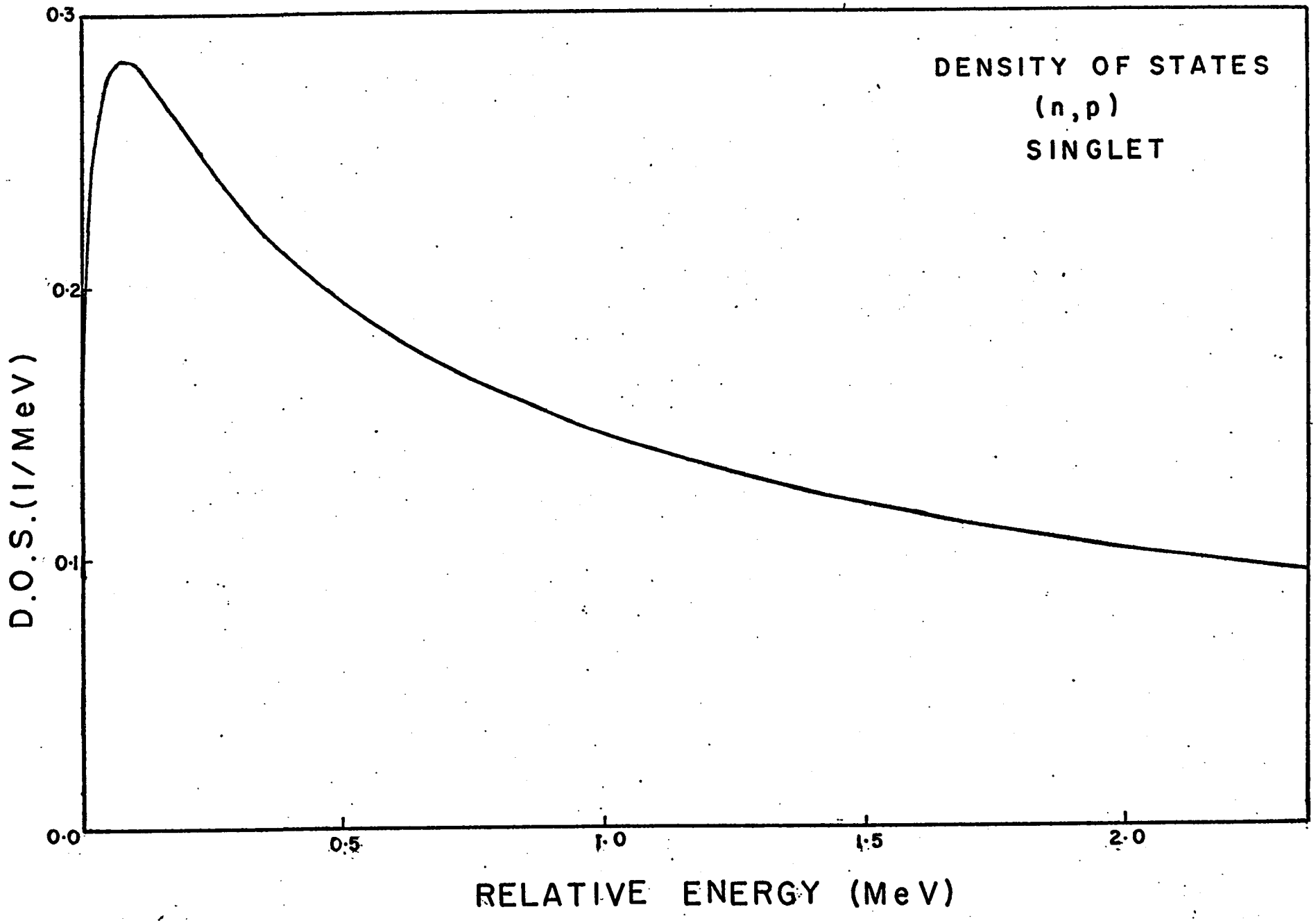
DENSITY OF STATES
(n,p)
SINGLET
0·3
0·2
0·1
0·0
D.O.S.(1/MeV)
0·5
1·0
1·5
2·0
RELATIVE ENERGY (MeV)

FIGURE 17

FIGURE 17

Density-of-states function for the triplet neutron-proton system. The parameters used are indicated on the diagram.

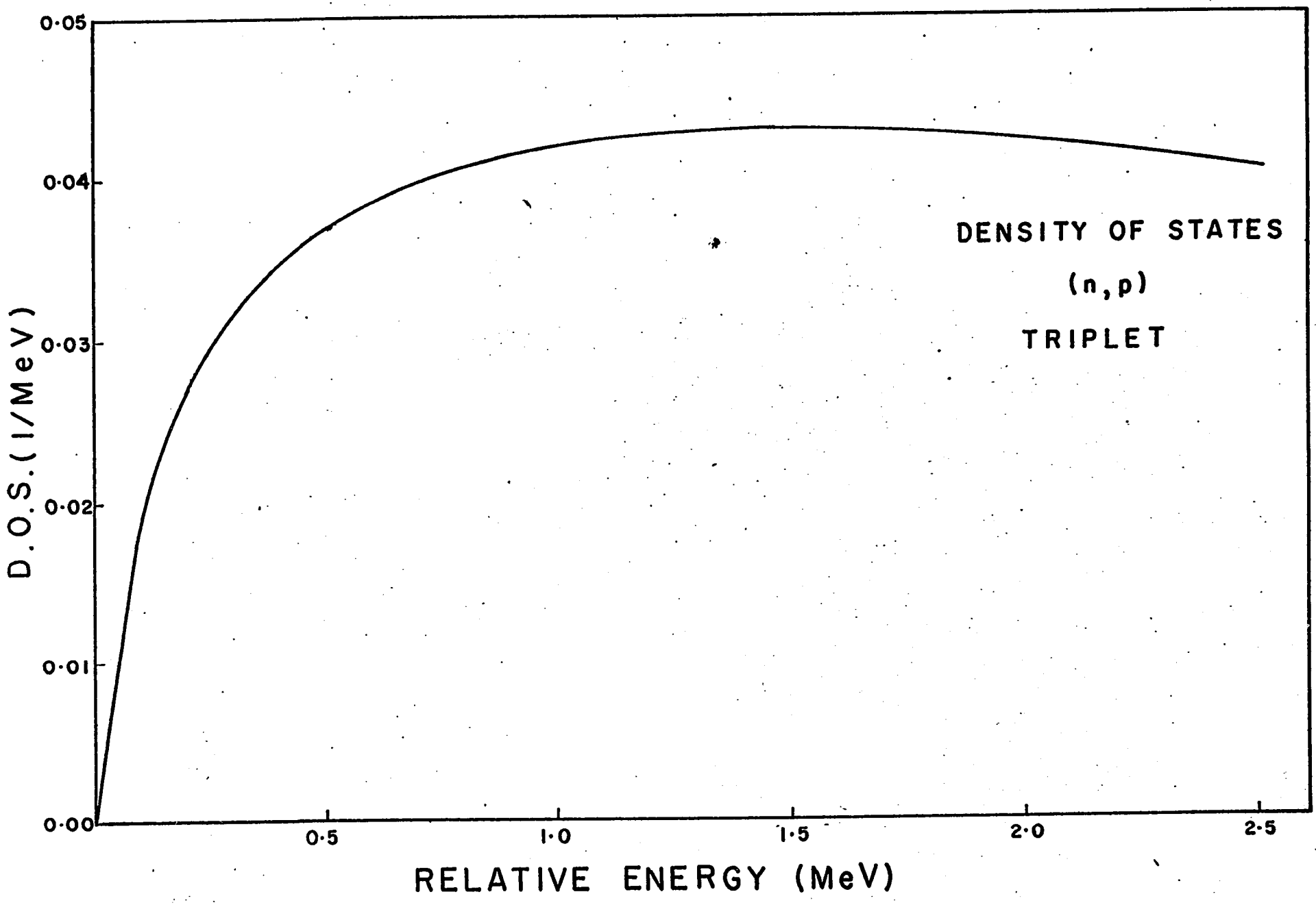
0·05
0·04
0·03
0·02
0·01
0·00
D.O.S.(1/MeV)
0·5
1·0
1·5
2·0
2·5
RELATIVE ENERGY (MeV)
DENSITY OF STATES
(n,p)
TRIPLET

CHAPTER VI. RESULTS AND CONCLUSION

All the spectra shown in Figs. 13 and 14 must be integrated over E_2 to compare the experimental results with the theoretical spectator model predictions. The integrated spectra are shown in Figs. 18 and 19. The theoretical curves have also been normalized to the same peak height of the experimental curves so that their shape can be compared with those of the experimental results. It is clear that the spectator model based on the simple impulse approximation cannot reproduce the differential cross-section. The shapes of the theoretical and the experimental curve are much alike, except for a few pairs of angles, and the positions of the maximum values of the cross-sections do not exactly coincide. The shifts of the peaks are about 2 to 3 MeV. In Table VI-1, the values of the full-width at half-maximum of the theoretical curves and the experimental curves are listed for comparison. It is obvious that the experimental FWHM is always smaller than or equal to the theoretical FWHM.

At first sight one might think that the energy shift of the experimental peak with respect to the theoretical one is probably due to gain shifts of the photomultiplier tubes and associated electronic circuits. If this had been the case, a larger experimental FWHM would have been expected rather than a smaller one for those spectra of smaller cross-sections. In fact the widths of the theoretical curves listed in Table VI-1 are smaller than they should be, because the experimental energy resolution caused by factors other than finite solid

FIGURE 18

FIGURE 18

The two parameter spectra on Fig. 13 are projected on the E_1 axis and shown here. Detector 1 is fixed at 40.5°, and θ_2, the angles of the movable detector are labelled on the diagrams. The solid lines are the spectator model predictions into which energy resolution due to the finite solid angles of detection have been folded. The dotted lines show the theoretical curves normalized to the same peak height as the experimental results. The error bars indicate only the relative uncertainty in cross-section - i.e. the error contributed by those variables which can differ from run to run with the same experimental arrangement.

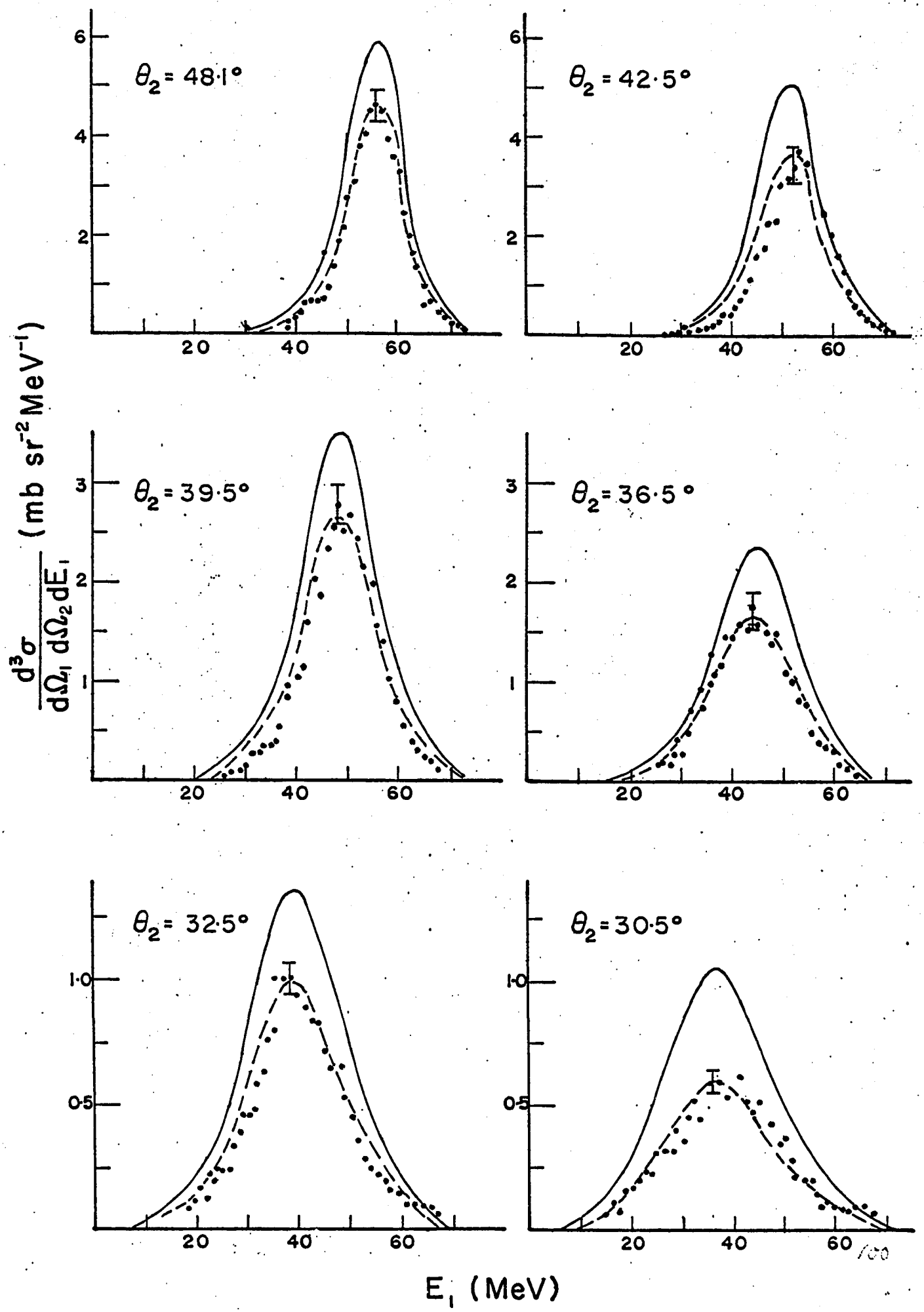
θ2 = 48·1°
θ2 = 42·5°
θ2 = 39·5°
θ2 = 36·5°
θ2 = 32·5°
θ2 = 30·5°
d³σ / dΩ1 dΩ2 dE1 (mb sr⁻² MeV⁻¹)
E1 (MeV)
20
40
60
100

FIGURE 19

FIGURE 19

See the caption of Figure 18. In these experiments, detector 1 is fixed at 35.5^{o}.

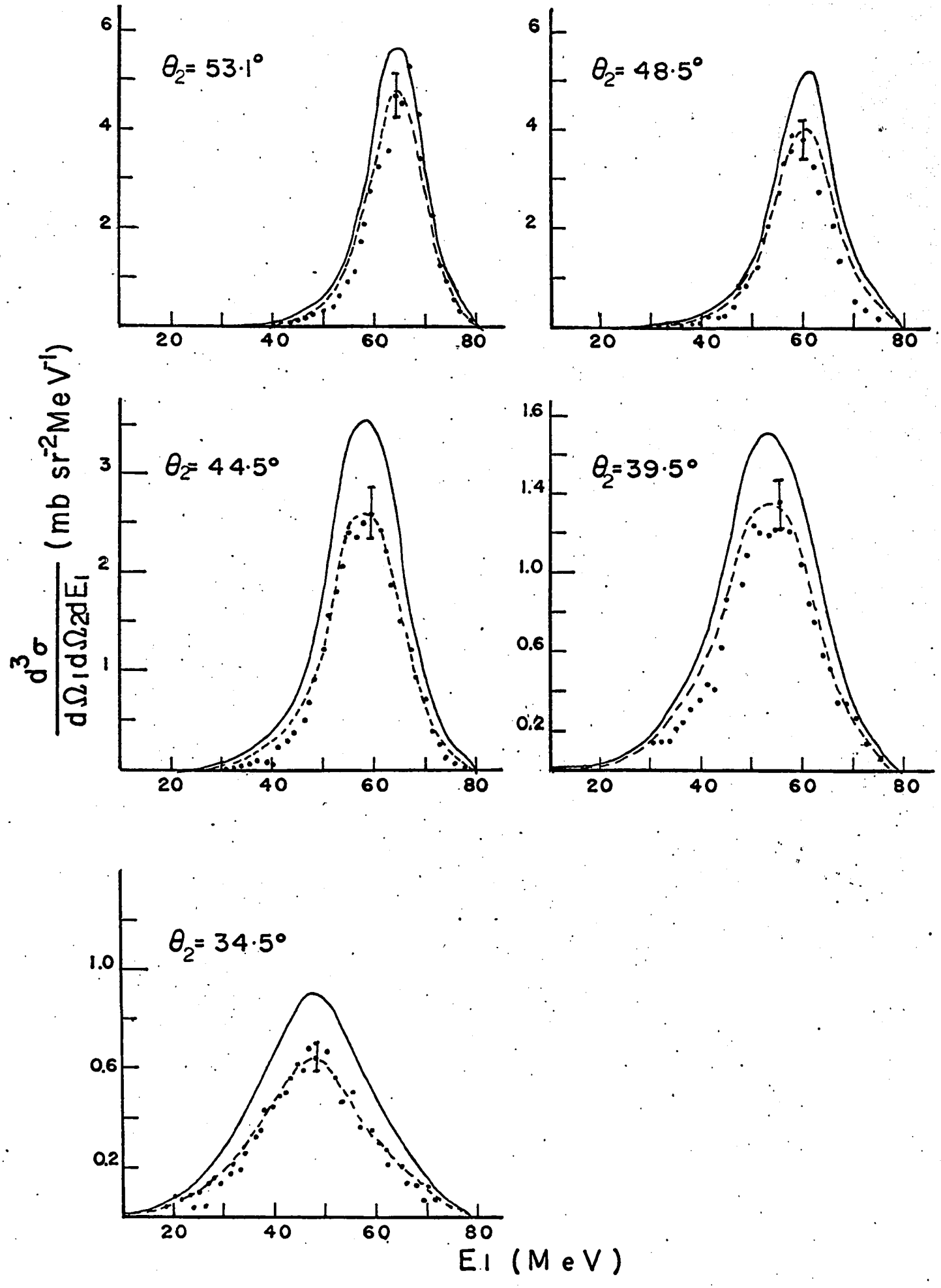
θ2= 53·1°
θ2= 48·5°
θ2= 44·5°
θ2= 39·5°
θ2= 34·5°
d³σ / dΩ1 dΩ2 dE1 (mb sr⁻² MeV⁻¹)
E1 (MeV)

angles of the detectors has not been folded into the theoretical curves. The lack of agreement in theoretical and experimental peak positions was observed for the D(p,2p)n reaction at 18.2 MeV, 46 MeV, and 50 MeV incident proton energies (W-63, SV-66, GK-64). The differential cross-sections at 18.2 MeV are at least 4 times smaller than the prediction of the spectator model; those at 46 MeV and 50 MeV are about 2 to 3 times smaller; in the present work and that at 145 MeV (KWC-61) the experimental values are closer to the predicted ones - i.e. less than a factor of 2 smaller.

As mentioned in section V-1d, the Chew-Low extrapolation will be applied to $\frac{d^2\sigma}{d\Omega_1\, d\Omega_2}$ instead of $\frac{d^3\sigma}{dE_1\, d\Omega_1\, d\Omega_2}$. With this method we have better counting statistics, and the inaccuracies associated with the quantity dE_1 are eliminated. The ratios of the experimental values of $\frac{d^2\sigma}{d\Omega_1\, d\Omega_2}$ to the theoretical ones, R, are listed in Table VI-1. The extrapolations for $\theta_1 = 40.5^\circ$, and $\theta_1 = 35.5^\circ$ are shown in Figs. 20-a and 20-b. Both curves can be extrapolated back to R =1 at $\bar{E}_3 = 1.1$ MeV within the experimental error, though the extrapolations are difficult due to the relatively long extrapolation distance compared to the experimentally feasible range of $\bar{E}_3$.

FIGURES 20a, b.

FIGURES 20 a, b.

Diagram a shows the Chew-Low extrapolation for detector 1 held at 40.5^{o}, while diagram b is for 35.5^{o}. The error bars indicate only relative uncertainty (as in Figure 18).

(a)

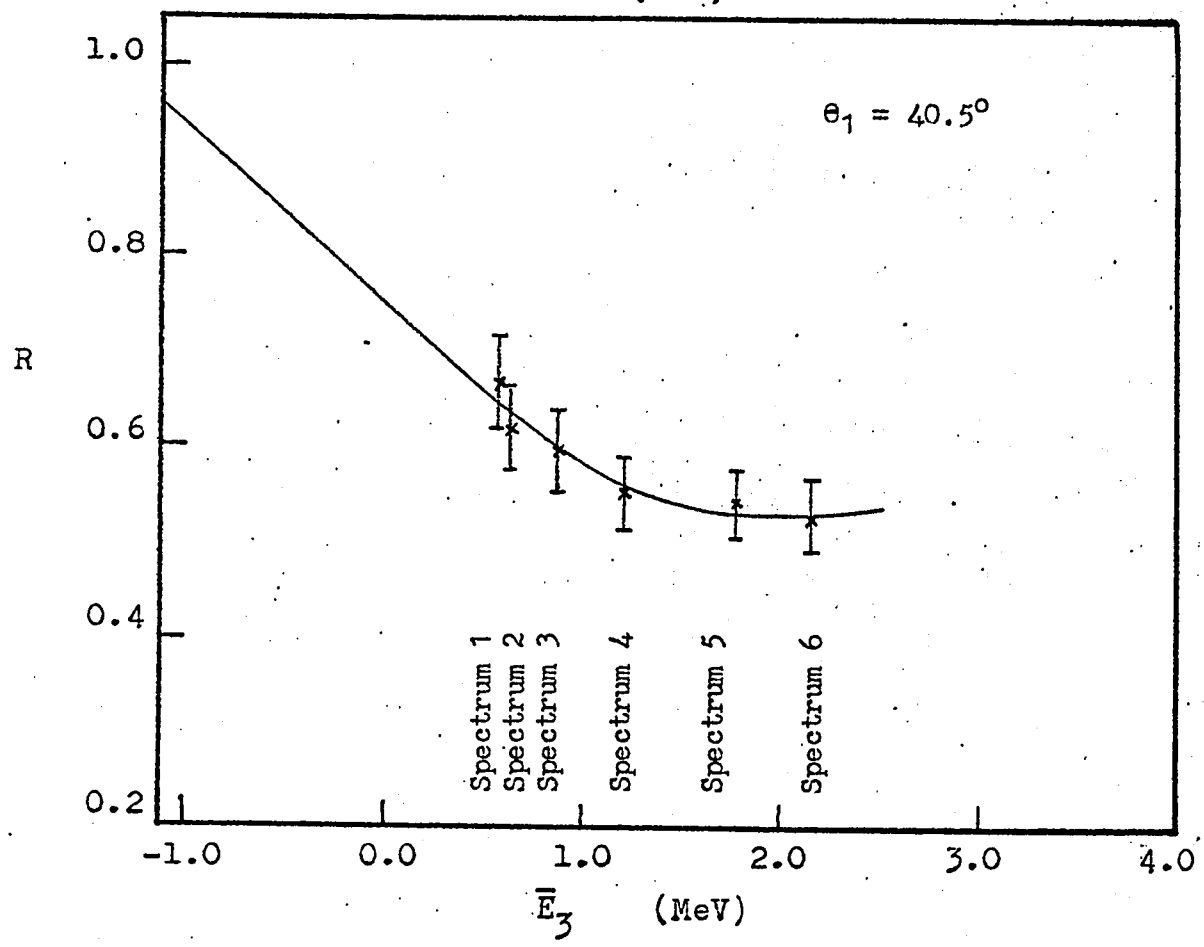
1.0
0.8
0.6
0.4
0.2
R
θ_1 = 40.5°
Spectrum 1
Spectrum 2
Spectrum 3
Spectrum 4
Spectrum 5
Spectrum 6
-1.0
0.0
1.0
2.0
3.0
4.0
$\bar{E}_3$ (MeV)

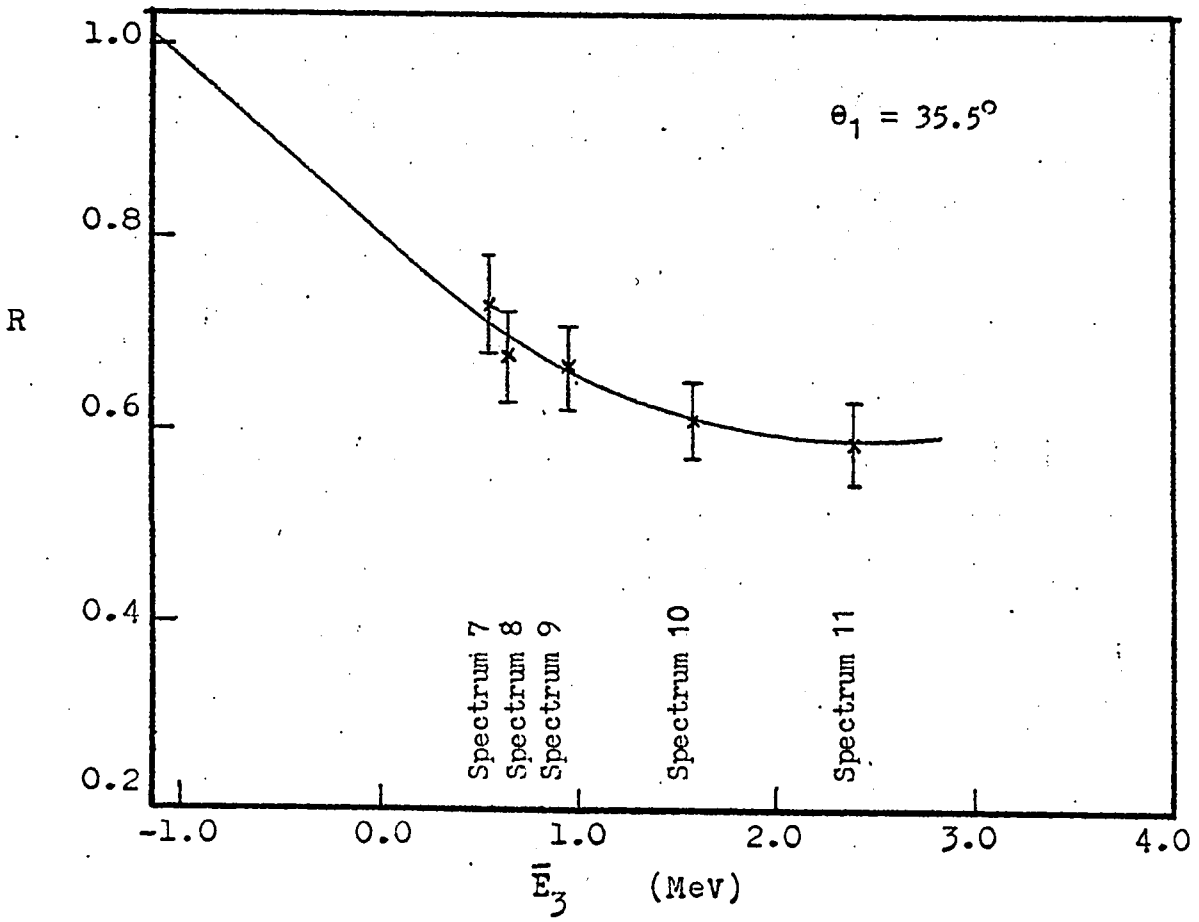
1.0
0.8
0.6
0.4
0.2
R
θ_1 = 35.5°
Spectrum 7
Spectrum 8
Spectrum 9
Spectrum 10
Spectrum 11
-1.0
0.0
1.0
2.0
3.0
4.0
$\bar{E}_3$ (MeV)

(b)

TABLE VI - 1

Values of R and widths of energy distribution for $\frac{d^3\sigma}{dE_1\, d\Omega_1\, d\Omega_2}$

θ_1 degree	θ_2 degree	R	FWHM (theor.) (MeV)	FWHM (exp.) (MeV)
40.5°	48.0°	0.666	12.7	12.0 ± 0.5
	42.5°	0.618	13.5	13.6 ± 0.5
	39.5°	0.589	16.3	15.6 ± 0.5
	36.5°	0.550	19.0	18.4 ± 0.8
	32.5°	0.539	21.2	18.8 ± 1.0
	30.5°	0.526	25.0	25.0 ± 1.4
35.5°	53.1°	0.737	12.5	12.5 ± 0.5
	48.6°	0.671	13.6	13.7 ± 0.5
	44.5°	0.666	16.2	14.8 ± 0.8
	39.5°	0.607	20.5	20.1 ± 1.0
	34.5°	0.588	26.3	22.3 ± 0.7

In the two-parameter spectra of Fig. 15 (a,b,c,d) enhanced yields are apparent on the portions of the kinematic locus where the values of E_3 are small, and where the internal energies between the neutron-proton pair are low (See Fig. 15 a,b,c,d,). After integration over E_2 they are shown in Figs. 21a, 22a, 23a, and 24a. In order to exclude the effect due to the available phase space, the differential cross-sections or the number of counts are divided by the calculated

phase space, and the results shown in Figs. 21b, 22b, 23b, and 24b, together with their phase space curves. Though the ratios thus obtained suppress the high energy peaks and elevate the low energy peaks corresponding to the (n,p) system with low internal energies, the peaks are definitely not wholly caused by the phase space effect.

The predictions of the spectator model can only roughly reproduce the shape of the higher energy peaks on Figs. 21a, 22a, and 23a. The higher energy peak in Fig. 24a is due to two different reactions: $^{12}C(p,2p)^{11}B$ and D(p,2p)n. From the disagreement in the prediction of position and shape of the peak and the experimental result, it is very likely that the $^{12}C(p,2p)^{11}B$ reaction is the main contribution to the peak. Though the theoretical prediction of differential cross-section is not accurate, the general trend of its dependence on the movable detector angle is qualitatively reliable. The maximum value of the spectator model prediction for spectrum 15 (Fig. 24a) is about one sixth that of spectrum 14 (Fig. 23a). Therefore the high energy peak of spectrum 15 is essentially due to the reaction $^{12}C(p,2p)^{11}B$.

The theory of the generalized density-of-states function developed by Phillips and his co-workers was also applied to these spectra (See section V-2c). It is not surprising that the theory cannot reproduce the higher energy peak for each spectrum at all, because in the calculation the effect of quasi-free scattering has not been taken into consideration by Phillips et al. Besides this the

assumption of isotropic angular distribution of first emission in the total center of mass system is obviously unrealistic because the first emitted particle favours the forward direction in the RCM system. The predictions of the generalized density-of-states function shown in Figs. 22-24 are purely idealized calculations, for the experimental energy resolutions have not been folded into the theoretical curves. Except for spectrum 14 (Fig. 23) all the theoretical peaks occur at lower energies than those of the experimental ones, and all of them show peaks much narrower than the experimental ones which correspond to low internal energies of the (n,p) system. The differences in the FWHM of the peaks could be lessened by taking the experimental energy resolution into account, but it is doubtful if the difference in the peak positions could be improved significantly by the same procedure.

In summary the study shows

(i) The spectator model can reproduce the shape of the spectra at forward angles. Quantitatively the prediction of the spectator model is higher than the experimental values of cross section.

(ii) Final state interactions between a neutron and a proton were observed for an incident proton energy of 100 MeV. The theory of the generalized density-of-states function does not successfully reproduce the spectra where final state interactions were observed.

However through this experiment the mechanism of the D(p,2p)n reaction

for various incident energies is clear. Since both the spectra featuring the spectator effect, and those showing the effects of final state interactions are observed at high and low incident particle energies (e.g. KWC-61, SJP-67, and this work), whether the reaction proceeds through quasi-free or quasi-sequential processes does not depend much on the incident particle energy, but is essentially determined by the reaction kinematics.

Besides the theories applied to the experimental results or the modified Born approximation (GB-51,WA-48), the final state interaction theory of Watson and Migdal has also been extensively applied. Except for the high energy polarization experiments (e.g. CS-57, TW-61) all of them have gained little success in the explanation of related information such as the scattering length of the two nucleon system (e.g. BA-67, BW-68, MG-68). Such a situation indicates plainly that three-particle systems are too complicated to be dealt with by physical intuition. One should turn to some more mathematically exact theories of these systems. Recently two methods of this kind of theory have been developed. They are the method of summation of non-relativistic diagrams (e.g. KP-65) and the Faddeev-Lovelace method. (e.g. Fa-60, LO-64). However further calculations must be carried out, and applications to scattering experiments still await investigation.

FIGURES 21, 22, 23, AND 24.

FIGURES 21, 22, 23, and 24.

Diagram (a)

Energy distributions of the differential cross-sections are shown. The broken curves are the predictions of the spectator model normalized to the height of the high energy peaks of the experimental curves. The solid lines are the predictions of the theory of the generalized density-of-state function normalized to the height of the low energy peaks of the experimental curves. In the calculation of the GDS function the following assumptions have been used:

(1) The radius of the volume of nuclear interaction was taken as 2.5×10^{-13} cm.

(2) Only the singlet interaction of the (n,p) system is considered since the value of the GDS function is significantly smaller for the triplet state than for the singlet.

(3) The singlet scattering length was taken as -23.68×10^{-13} cm and the effective range taken as 2.7×10^{-13} cm.

(4) The distribution in the two-nucleon center-of-mass system was taken as isotropic.

(5) The distribution of the first emitted particle in the total center-of-mass system was taken as isotropic.

(6) The matrix element of the reactions were taken as energy-independent.

The energy resolution has not been folded into the predictions of the GDS theory.

Diagram (b)

The phase space available (ρ, broken line) is shown, together with the ratio of the differential cross-section on diagram (a) to the phase space, (solid line).

(a)

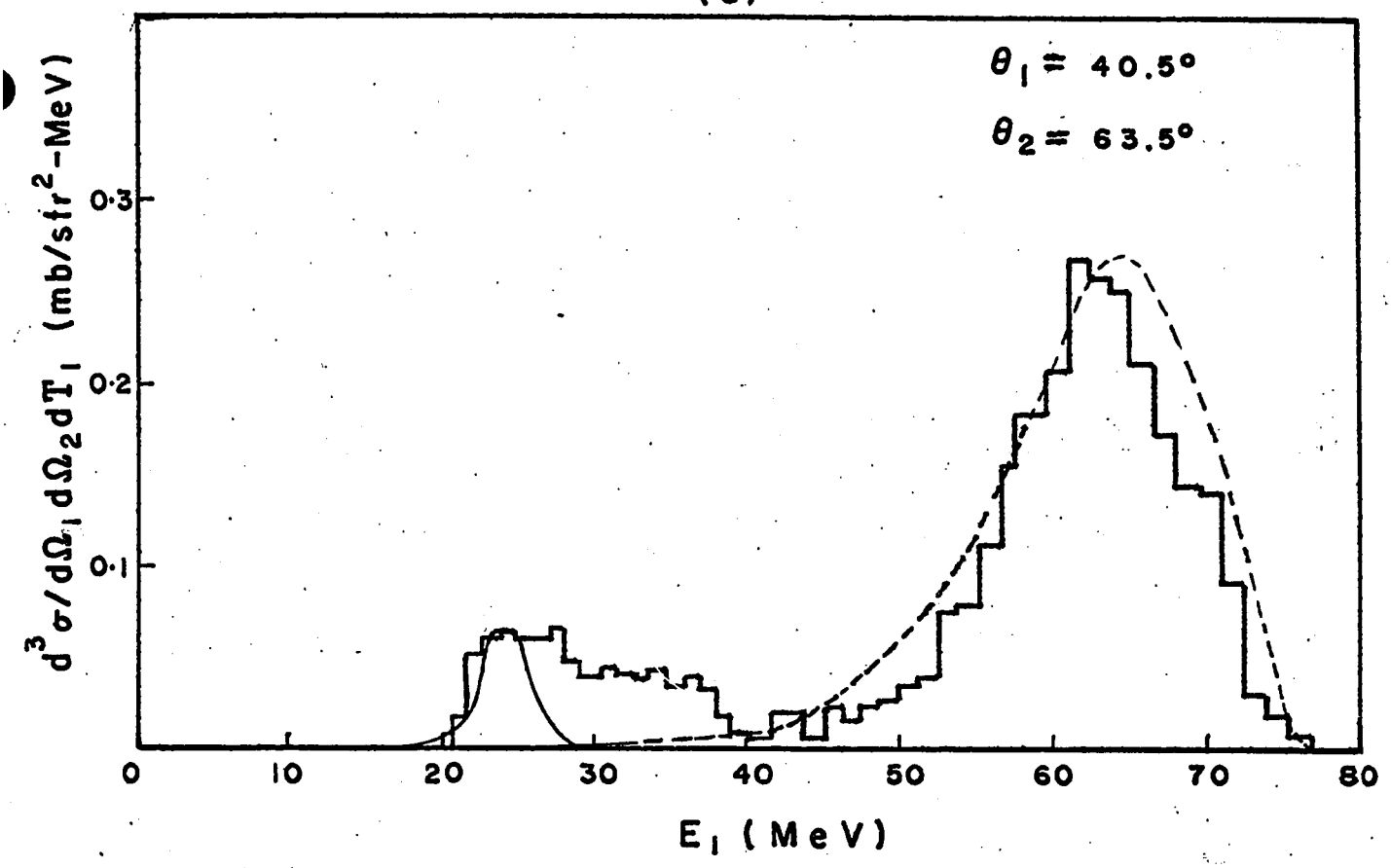
$\theta_1 = 40.5°$
$\theta_2 = 63.5°$
$d^3\sigma/d\Omega_1 d\Omega_2 dT_1$ (mb/str^2-MeV)
0.3
0.2
0.1
0
10
20
30
40
50
60
70
80
E_1 (MeV)

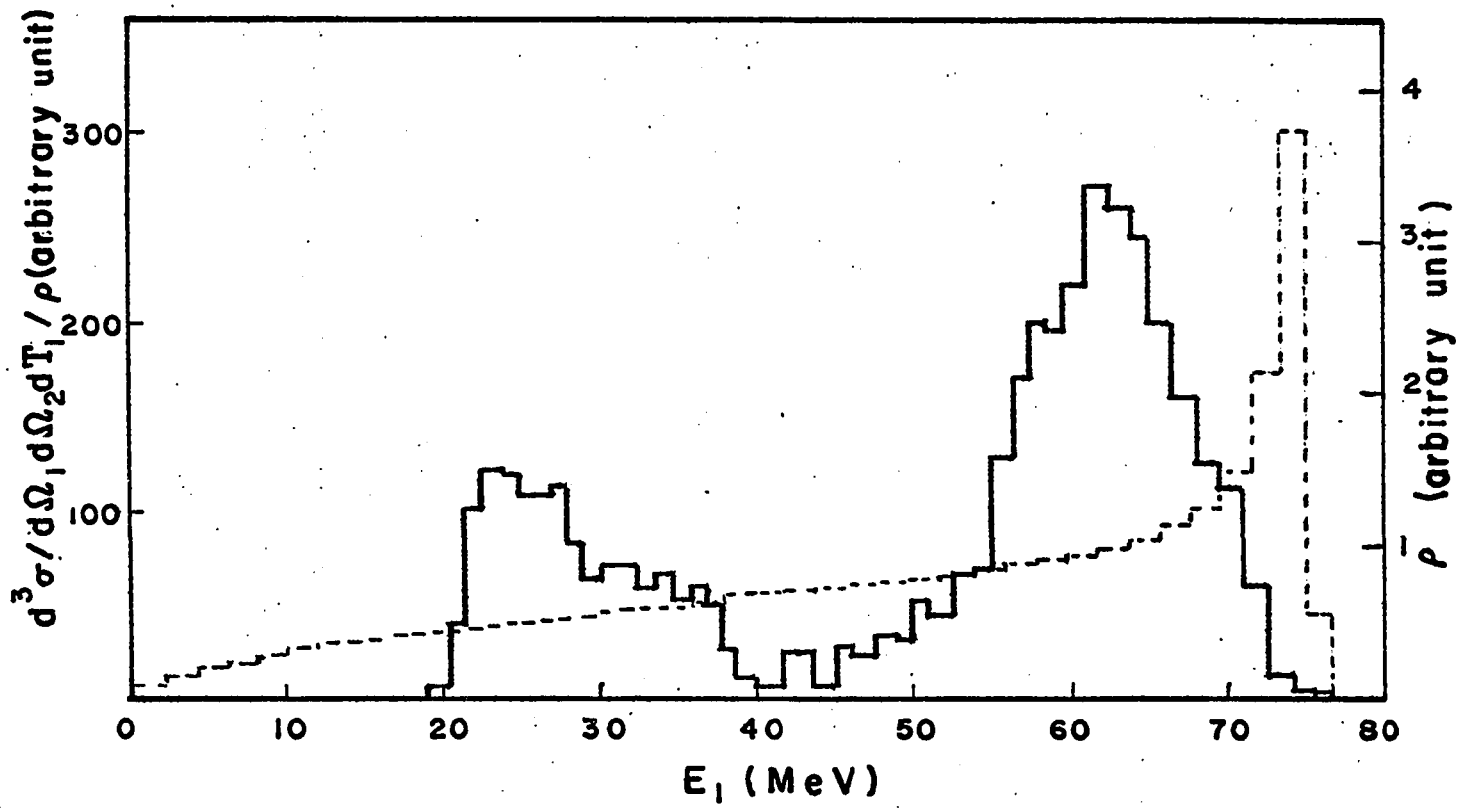
$d^3\sigma/d\Omega_1 d\Omega_2 dT_1 / \rho$(arbitrary unit)
300
200
100
0
10
20
30
40
50
60
70
80
E_1 (MeV)
ρ (arbitrary unit)
4
3
2
1

(b)

FIGURE 21

(a)

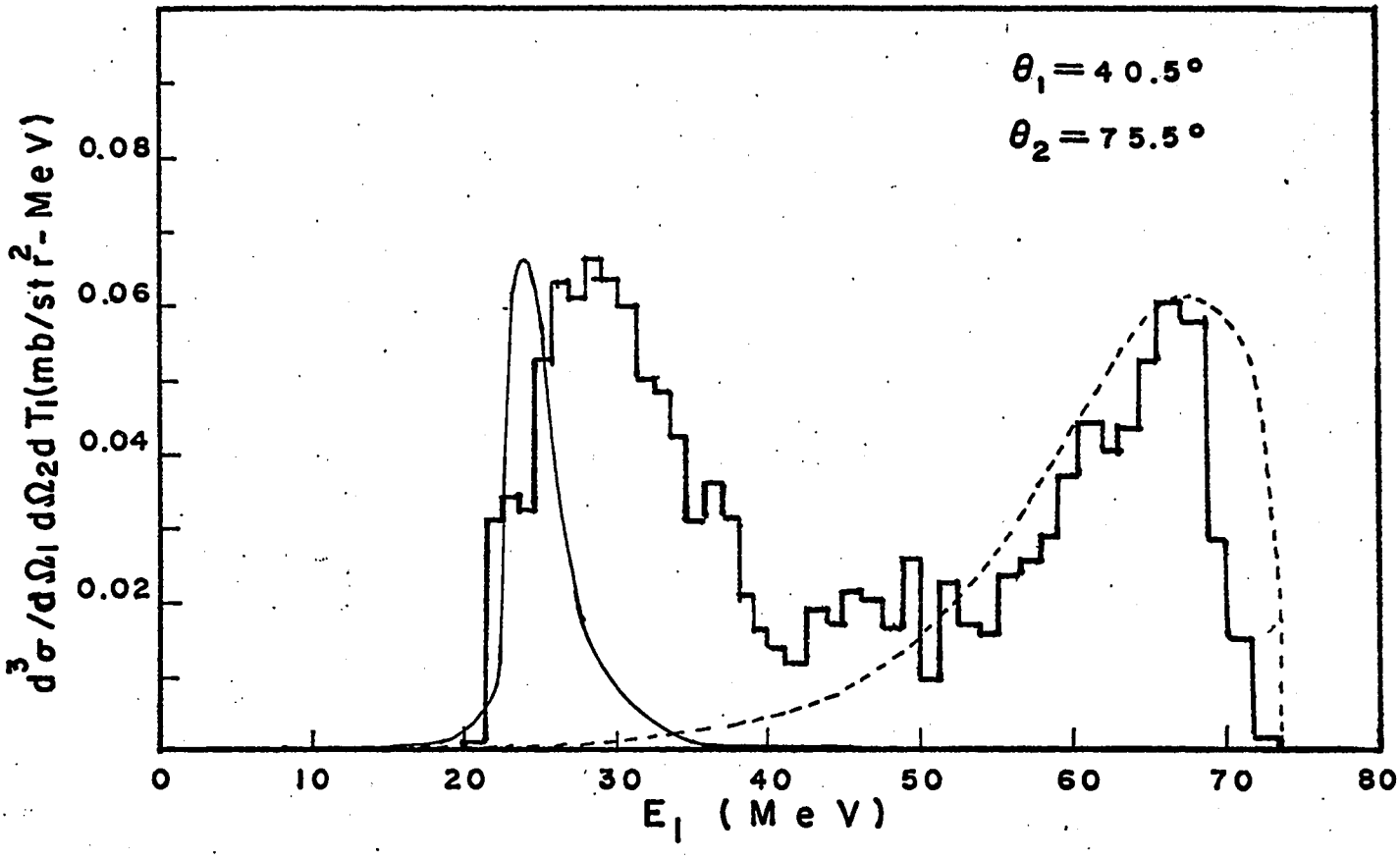
$\theta_1 = 40.5°$
$\theta_2 = 75.5°$
$d^3\sigma/d\Omega_1 d\Omega_2 dT_1$ (mb/str^2-MeV)
0.08
0.06
0.04
0.02
0
10
20
30
40
50
60
70
80
E_1 (MeV)

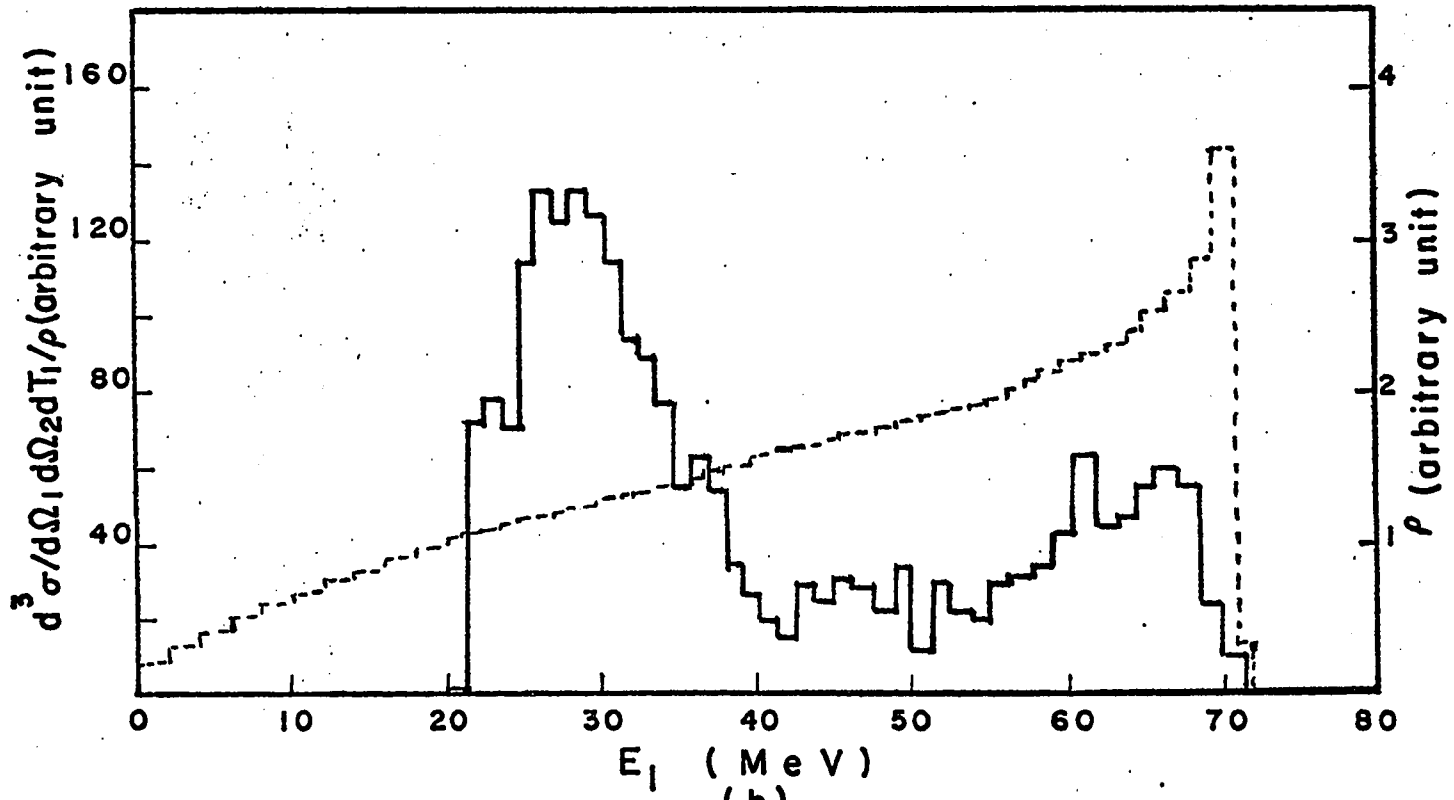
$d^3\sigma/d\Omega_1 d\Omega_2 dT_1/\rho$ (arbitrary unit)
160
120
80
40
ρ (arbitrary unit)
4
3
2
1
0
10
20
30
40
50
60
70
80
E_1 (MeV)

(b)

FIGURE 22

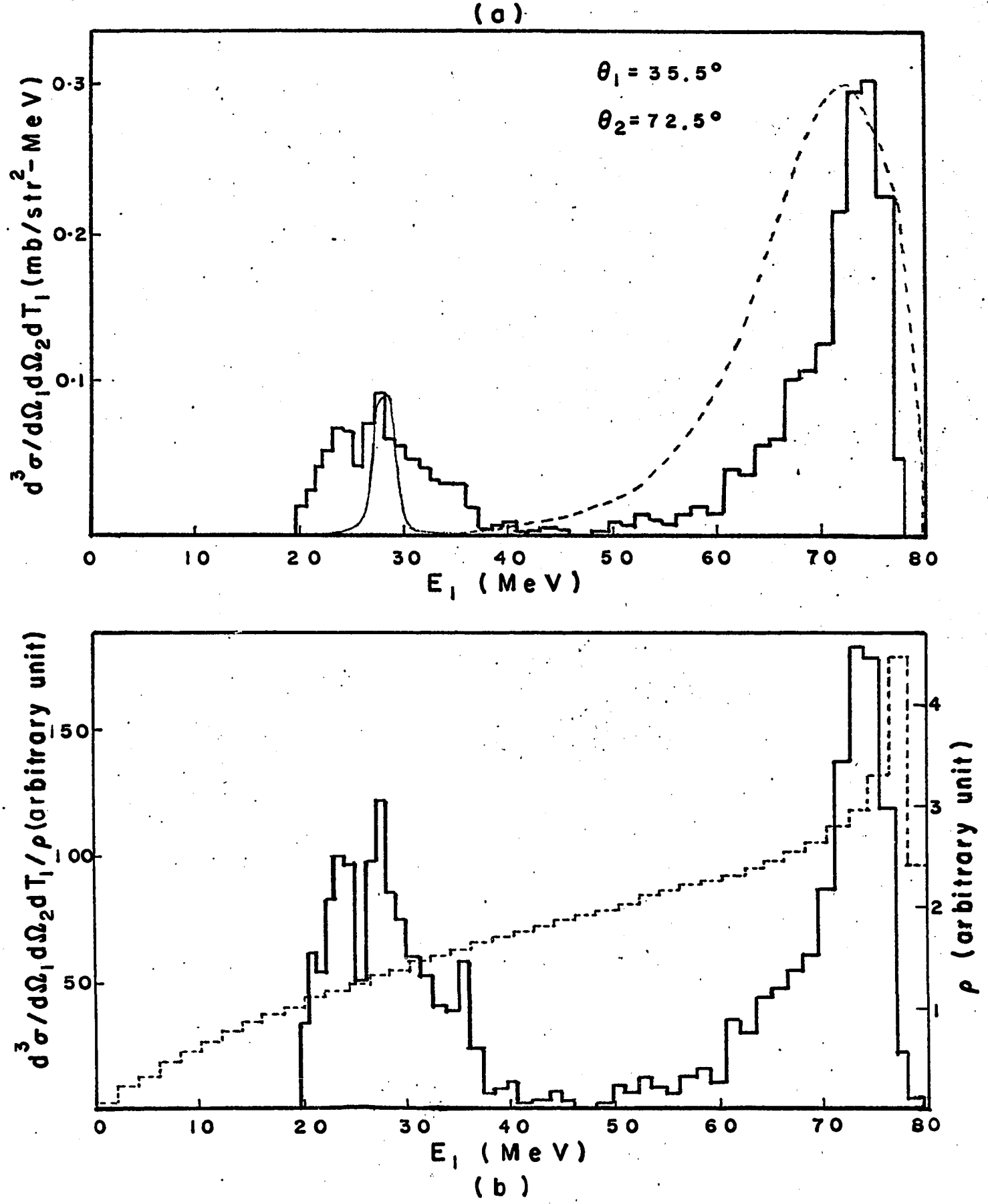
(a)
$\theta_1 = 35.5°$
$\theta_2 = 72.5°$
$d^3\sigma/d\Omega_1 d\Omega_2 dT_1$ (mb/str^2-MeV)
0·3
0·2
0·1
0
10
20
30
40
50
60
70
80
E_1 (MeV)
$d^3\sigma/d\Omega_1 d\Omega_2 dT_1/\rho$ (arbitrary unit)
150
100
50
ρ (arbitrary unit)
4
3
2
1
0
10
20
30
40
50
60
70
80
E_1 (MeV)
(b)

FIGURE 23

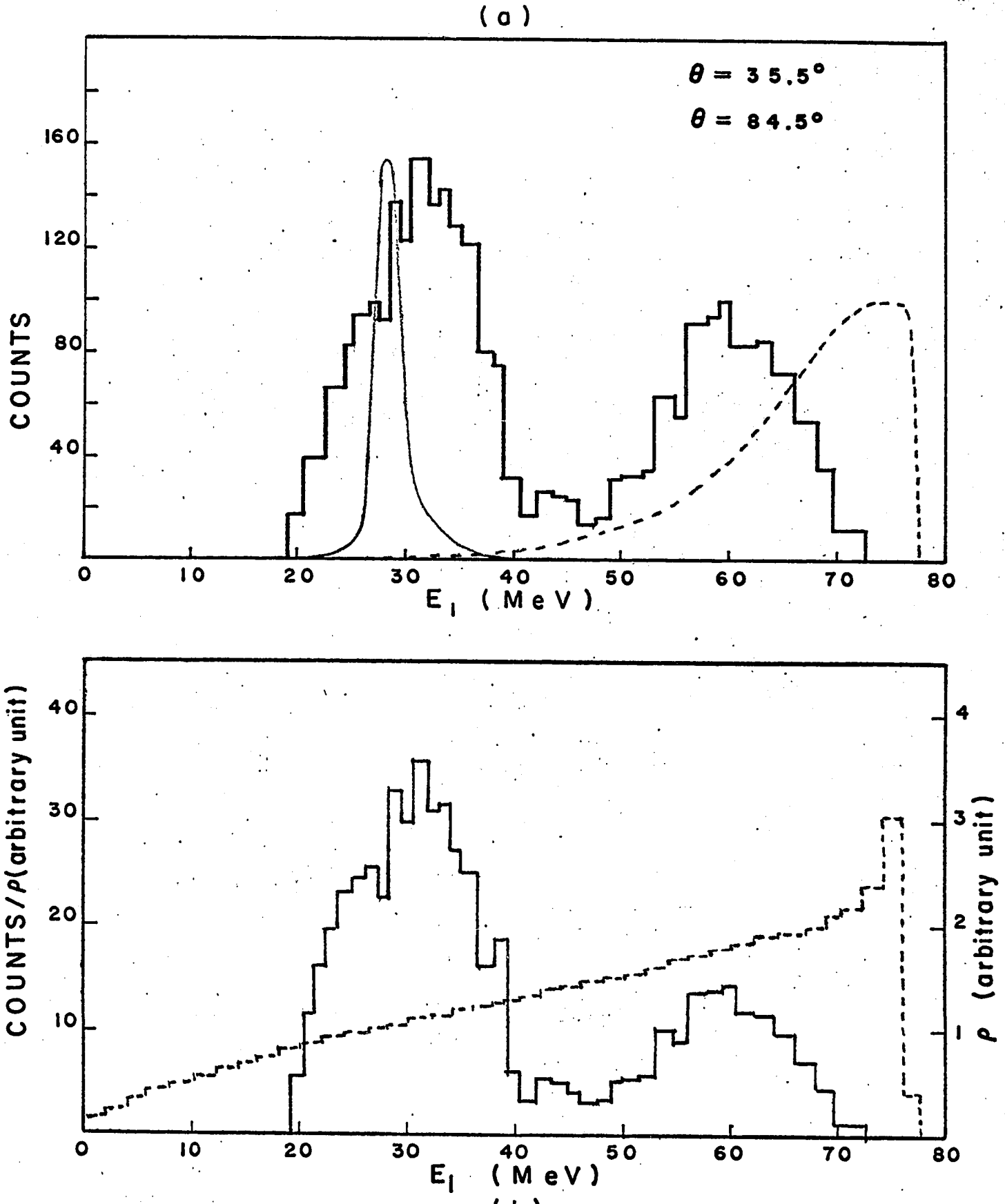
(a)
θ = 35.5°
θ = 84.5°
COUNTS
160
120
80
40
0
10
20
30
40
50
60
70
80
E1 (MeV)
COUNTS/ρ(arbitrary unit)
40
30
20
10
4
3
2
1
ρ (arbitrary unit)
0
10
20
30
40
50
60
70
80
E1 (MeV)
(b)

FIGURE 24

APPENDIX A

RELATIVISTIC DIFFERENTIAL CROSS-SECTION TRANSFORMATION FOR A TWO-BODY SYSTEM.

The relation between differential cross-sections in a center-of-mass system and those in a laboratory system has been discussed by many authors (e.g. WY-63). Though the derivation of the transformation relation is straightforward, many have arrived at an incorrect expression for it. In the following the transformation Jacobian J, in eq. (1) will be expressed in terms of kinematic variables of the center-of-mass system and of the laboratory system.

$$\frac{d\sigma}{d\Omega} = J \frac{d\sigma}{d\bar{\Omega}} = \left(\frac{d\Omega}{d\bar{\Omega}} \right)^{-1} \frac{d\sigma}{d\bar{\Omega}} \qquad (1)$$

The method of the reference (WY-63) will be adopted here. All the "bar" variables are in the center-of-mass system; those without "bar" are in the laboratory system. The velocity of light, c, is taken as 1. Eq. (1) is then the relation between a differential cross-section in the center-of-mass system and that of the laboratory system with

$$J = \frac{d\bar{\Omega}}{d\Omega} = \frac{\partial\bar{\Omega}}{\partial\Omega} + \frac{\partial\bar{\Omega}}{\partial E} \cdot \frac{\partial E}{\partial\Omega} \qquad (2a)$$

$$J^{-1} = \frac{d\Omega}{d\bar{\Omega}} = \frac{\partial\Omega}{\partial\bar{\Omega}} + \frac{\partial\Omega}{\partial\bar{E}} \cdot \frac{\partial\bar{E}}{\partial\bar{\Omega}} \qquad (2b)$$

where $\bar{E}$ and E are the total energies of the scattered particle in the CM system and the LAB system, respectively. Because in the CM system $\bar{E}$ does not depend on the scattering angle $\bar{\theta}$, it is more convenient

to work on eq. (2b) rather than eq. (2a). Eq. (2b) then becomes

$$\frac{d\Omega}{d\bar{\Omega}} = \frac{\partial\Omega}{\partial\bar{\Omega}} = \frac{d\ \mathrm{Cos}\ \theta}{d\ \mathrm{Cos}\ \bar{\theta}} \tag{3}$$

If eq. (2a) is preferred, one must not drop the second term of eq. (2a) because E is a function of θ; this is the point most often overlooked.

The law of conservation of momentum states that

$$\vec{P}_p + \vec{P}_T = 0 = \vec{P} + \vec{P}' \tag{4a}$$

$$\vec{P}_p + \vec{P}_T = \vec{P}_o = \vec{P} + \vec{P}' \tag{4b}$$

where $\vec{P}_p$, $\vec{P}_T$, $\vec{P}$, $\vec{P}'$ are the momenta of the projectile, the target, the scattered particle, and the recoil residual particle in the LAB system, respectively.

$\vec{P}_o$ is defined by (4b) and its corresponding total energy is E_o.

$$\vec{V} = \frac{\vec{P}_o}{E_o} \tag{5}$$

The direction of $\vec{P}_o$ is chosen as the x-axis, so that the transverse direction is y-axis, for this is the coplanar problem. The Lorentz transformations of momentum and energy between the two coordinate systems are

$$\begin{aligned} \bar{P}_x &= \gamma\ (P_x - VE) \\ \bar{P}_y &= P_y \\ \bar{E} &= \gamma\ (E - VP_x) \end{aligned} \tag{6}$$

$$P_x = \gamma (\bar{P}_x + V\bar{E})$$
$$P_y = \bar{P}_y \qquad (7)$$
$$E = \gamma (\bar{E} + V\bar{P}_x)$$

with $\gamma = \dfrac{1}{\sqrt{1 - V^2}}$

(i) Express J in terms of variables in the CM system.

By the use of eq. (7)

$$\text{Cos } \theta = \frac{P_x}{P}$$

$$= \frac{P_x}{\sqrt{P_x^2 + P_y^2}} = \frac{\gamma (\bar{P}_x + V\bar{E})}{\sqrt{\bar{P}_y^2 + \gamma^2(\bar{P}_x + V\bar{E})^2}}$$

$$= \frac{\gamma(\text{Cos } \bar{\theta} + V \bar{E}/\bar{P})}{\sqrt{\sin^2 \bar{\theta} + \gamma^2(\bar{P}_x/\bar{P})^2 + \gamma^2(2\bar{P}_x V\bar{E}/\bar{P}^2) + \gamma^2(\bar{E}/\bar{P})^2}}$$

$$= \frac{\text{Cos } \bar{\theta} + \bar{\rho}}{\sqrt{1 + 2\bar{\rho} \text{ Cos } \bar{\theta} + \bar{\rho}^2 - V^2 \text{Sin}^2 \bar{\theta}}} \quad \text{with } \bar{\rho} = \frac{V}{\bar{v}} \quad , \ \bar{v} = \frac{\bar{P}}{\bar{E}}$$

$$= \frac{\text{Cos } \bar{\theta} + \bar{\rho}}{\sqrt{\bar{A}}} \quad \text{with } \bar{A} = 1 + 2\bar{\rho} \text{ Cos } \bar{\theta} + \bar{\rho}^2 - V^2 \text{Sin}^2 \bar{\theta} \qquad (8)$$

Substitute (8) into (3)

$$J^{-1} = \frac{d\Omega}{d\bar{\Omega}} = \frac{d}{d\bar{\mu}} \frac{\bar{\mu} + \bar{\rho}}{\sqrt{1 + 2\bar{\rho}\bar{\mu} + \bar{\rho}^2 + V^2(1-\bar{\mu}^2)}} \quad \text{where } \bar{\mu} = \text{Cos } \bar{\theta}$$

$$= \frac{1 + \bar{\mu}\bar{\rho}}{\gamma^2 \bar{A}^{3/2}} \qquad (9)$$

The explicit expression of (1) in terms of variables in the CM system is then

$$\frac{d\sigma}{d\Omega} = J\frac{d\sigma}{d\Omega} = \frac{\gamma^2 \bar{A}^{3/2}}{1 + \bar{\mu}\bar{\rho}} \cdot \frac{d\sigma}{d\bar{\Omega}} \qquad (10)$$

(ii) Express J in terms of variables in the LAB system,

Similarly by using eq. (6)

$$\text{Cos}\ \bar{\theta} = \frac{\bar{P}_x}{\sqrt{\bar{P}_x^2 + \bar{P}_y^2}} = \frac{\text{Cos}\ \theta - \rho}{\sqrt{A}} \qquad \text{with} \quad \nu = \frac{P}{E}, \quad \rho = \frac{V}{\nu}, \quad A = 1 - 2\rho\,\text{Cos}\ \theta + \rho^2 - V^2\text{Sin}^2\theta \qquad (11)$$

$$\bar{\rho} = \frac{V}{\bar{\nu}} = \frac{V\bar{E}}{\sqrt{A}\,\gamma\,P} = \frac{\rho}{\sqrt{A}}(1 - V\nu\,\text{Cos}\ \theta) \qquad (12)$$

$$\bar{A} = 1 + 2\bar{\rho}\,\text{Cos}\ \bar{\theta} + \bar{\rho}^2 - V^2\,\text{Sin}^2\,\bar{\theta} = \frac{(1 - V^2)^2}{A} = \frac{1}{\gamma^4 A} \qquad (13)$$

Substituting equations (11), (12) and (13) into (9), one obtains

$$J^{-1} = \frac{d\Omega}{d\bar{\Omega}} = \frac{1 + \bar{\mu}\bar{\rho}}{\gamma^2 \bar{A}^{3/2}} = \gamma^2 A^{1/2}(1 - \rho\,\text{Cos}\ \theta) \qquad (14)$$

$$J = \frac{1}{\gamma^2 A^{1/2}(1 - \rho\,\text{Cos}\ \theta)} \qquad (15)$$

The explicit expression of (1) in terms of variables in the LAB system is then

$$\frac{d\sigma}{d\Omega} = \frac{1}{\gamma^2 A^{1/2}(1 - \rho\,\text{Cos}\ \theta)} \frac{d\sigma}{d\bar{\Omega}} \qquad (16)$$

APPENDIX B

RELATIVISTIC PHASE-SPACE CALCULATION

The following notations will be adopted for this appendix

E_o, E_T = Total energy of the projectile and the target, respectively.

$\vec{P}_o, \vec{P}_T$ = The 3- momentum of the projectile and the target, respectively.

E_1, E_2, E_3 = Total energy of the outgoing particle 1, 2, 3, respectively.

T_1, T_2, T_3 = Kinetic energy of the particle 1, 2, 3, respectively.

$\vec{P}_1, \vec{P}_2, \vec{P}_3$ = The 3- momentum of particle 1, 2, 3, respectively.

The velocity of light, c, is taken to be 1. All the variables above are subject to the laws of total energy and momentum conservation.

$$\text{Total phase space} \propto \iiint (E_o + E_T - E_1' - E_2' - E_3')\, x \,(\vec{P}_o - \vec{P}_1' - \vec{P}_2' - \vec{P}_3')\, d\vec{P}_1'\, d\vec{P}_2'\, d\vec{P}_3' \quad (1)$$

$$= \iint \delta\left(E_o + E_T - E_1' - E_2' - \sqrt{(\vec{P}_o - \vec{P}_1' - \vec{P}_2')^2 + m_3^2}\right) d\vec{P}_1'\, d\vec{P}_2' \quad (2)$$

$$= \iiint\!\!\int \delta\left[f(P_2')\right]\, (P_1')^2\, dP_1'\, d\Omega_1'\, (P_2')^2\, dP_2'\, d\Omega_2'$$

where
$$f(P_2') = E_o + E_T - E_1' - E_2' - \sqrt{(\vec{P}_o - \vec{P}_1' - \vec{P}_2')^2 + m_3^2} \quad (3)$$

By use of the relation

$$\delta f(P_2') = \Sigma \frac{\delta(P_2' - P_2)}{\left.\frac{df}{dP_2'}\right|_{P_2}} \quad (4)$$

eq. (2) becomes

$$\iiint\!\!\int \frac{\delta(P_2' - P_2)}{\left| -\frac{P_2'}{E_2} - \frac{P_2' + P_1' \cos\theta_{1\,2} - P_o \cos\theta_2}{E_3} \right|_{P_2}} (P_1')^2 dP_1' d\Omega_1' (P_2')^2 dP_2' d\Omega_2' \quad (5)$$

Whenever $\vec{P}_2' = \vec{P}_2$ the laws of total energy conservation and momentum conservation should be satisfied, and the total phase space integral can be written as

$$\iiint \rho(P_1, \Omega_1, \Omega_2)\, dP_1\, d\Omega_1\, d\Omega_2 \tag{6}$$

where

$$\rho(P_1, \Omega_1, \Omega_2) = \frac{P_1^2 P_2^2}{\frac{P_2}{E_2} + \frac{P_2 + P_1 \cos\theta_{12} - P_o \cos\theta_2}{E_3}} \tag{7}$$

$$\rho(T_1, \Omega_1, \Omega_2) = \frac{E_1}{P_1}\rho(P_1, \Omega_1, \Omega_2)$$

$$= \frac{E_1 E_2 E_3 P_1 P_2}{(E_2 + E_3) + E_2 \frac{(\vec{P}_1 - \vec{P}_o)\cdot\vec{P}_2}{P_2^2}} \tag{8}$$

Equation (8) is the differential phase space needed in section V-2. In order to compare the shape with the experimental data $\rho(T_1, \Omega_1, \Omega_2)$ has to be integrated over the energy increment ΔT_1 and the finite solid angles $\Delta\Omega_1$ and $\Delta\Omega_2$, i.e.

$$\int_{\Delta T_1}\int_{\Delta\Omega_1}\int_{\Delta\Omega_2} \rho(T_1, \Omega_1, \Omega_2)\, dT_1\, d\Omega_1\, d\Omega_2 \tag{9}$$

APPENDIX C

DERIVATION OF KINEMATIC JACOBIANS

Consider a two-step reaction non-relativistically

$$a + b \longrightarrow i + (jk) \longrightarrow i + j + k$$

in two kinds of coordinate frame: a coordinate system (abbreviated as the U system) which moves uniformly, and a coordinate system called the recoil center-of-mass system (RCM) which is the relative coordinate system more appropriate for the reaction above - i.e. the i^{th} particle is first emitted. The notation (i, j, k) stands for any permutation of 1, 2, and 3. The schematic representations of the U and RCM systems are shown below for the case of (1, 2, 3).

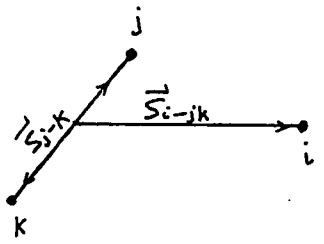

RCM system

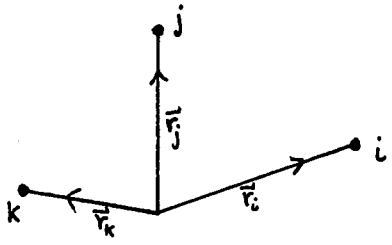

U system

Some of the relations between the two systems are

$$\vec{s}_{i-jk} = \vec{r}_i - \frac{m_j \vec{r}_j + m_k \vec{r}_k}{m_j + m_k} \tag{1a}$$

$$\vec{s}_{j-k} = \vec{r}_j - \vec{r}_k \tag{1b}$$

$$\mu_{i-jk} = \frac{m_i\,(m_j + m_k)}{M}, \quad M = m_i + m_j + m_k \tag{1c}$$

$$\mu_{j-k} = \frac{m_j\, m_k}{m_j + m_k} \tag{1d}$$

where m_1, m_2, and m_3 are the masses of the three particles, and μ_{i-jk}, μ_{j-k} are the reduced masses.

In particular there are two different coordinate systems which belong to the category of the U system. They are the total center-of-mass system, (SCM), and the laboratory system (LAB). For these $\vec{P} = 0$, and $\vec{P} = \vec{P}_T$, respectively,

$$\vec{P} = \vec{P}_1 + \vec{P}_2 + \vec{P}_3 = \vec{P}_o + \vec{P}_T \quad \text{with } \vec{P}_i = m_i \frac{d\vec{r}_i}{dt} \tag{2}$$

where $\vec{P}_o$ and $\vec{P}_T$ are the momenta of the projectile and the target, respectively.

In section B-2c (eq.11) the laboratory differential cross-section is derived from that in the RCM system:

$$\sigma^{(i)}_{RCM} = \frac{d^3\sigma}{dE_{i-jk}\, d\Omega_{i-jk}\, d\Omega^{(i)}_{j-k}} \tag{3}$$

Following the notation in section V-2c, J_i (i = 1, 2, 3) is the Jacobian which transforms $\sigma^{(i)}_{RCM}$ to the SCM system, i.e.:

$$\sigma_{SCM} = \frac{d^3\sigma}{dE_1^{\,c}\, d\Omega_1^{\,c}\, d\Omega_2^{\,c}} = \sigma^{(i)}_{RCM}\, J_i \tag{4}$$

More explicitly

$$J_1 = \frac{\partial(E_{1-23}, \Omega_{1-23}, \Omega_{2-3})}{\partial(E_1^c, \Omega_1^c, \Omega_2^c)}, \quad J_2 = \frac{\partial(E_{2-13}, \Omega_{2-13}, \Omega_{1-3})}{\partial(E_1^c, \Omega_1^c, \Omega_2^c)}, \quad J_3 = \frac{\partial(E_{3-21}, \Omega_{3-21}, \Omega_{2-1})}{\partial(E_1^c, \Omega_1^c, \Omega_2^c)}$$

and J_L is the Jacobian which transforms σ_{SCM} to σ_{LAB}

$$\sigma_{LAB} = \frac{d^3\sigma}{dE_1^l \; d\Omega_1^l \; d\Omega_2^l} \; J_L \tag{5a}$$

$$J_L = \frac{\partial(E_1^c, \Omega_1^c, \Omega_2^c)}{\partial(E_1^l, \Omega_1^l, \Omega_2^l)} \tag{5b}$$

For the case in which the particle detected by detector 1 is first emitted, the Jacobian J which transforms $R_{RCM}^{(i)}$ to a U system is derived in the following way:

From (1a) and (1b), one obtains

$$\vec{P}_{1-23} = \mu_{1-23} \frac{d\vec{S}_{1-23}}{dt} = \frac{\mu_{1-23}}{m_1} \vec{P}_1 - \frac{\mu_{1-23}}{m_2+m_3} (\vec{P}_2 + \vec{P}_3) \tag{6a}$$

$$\vec{P}_{2-3} = \mu_{2-3} \frac{d\vec{S}_{2-3}}{dt} = \frac{\mu_{2-3}}{m_2} \vec{P}_2 - \frac{\mu_{2-3}}{m_3} \vec{P}_3 \tag{6b}$$

and then

$$d\vec{P}_{1-23} \; d\vec{P}_{2-3} = d\vec{P}_1 \; d\vec{P}_2 \tag{7a}$$

i.e. $$P_{1-23}^2 \, dP_{1-23} \, d\Omega_{1-23} \, P_{2-3}^2 \, dP_{2-3} \, d\Omega_{2-3} = P_1^2 dP_1 d\Omega_1 P_2^2 dP_2 d\Omega_2 \tag{7b}$$

By use of the relations

$$P_{1-23} \, dP_{1-23} = \mu_{1-23} \, dE_{1-23}$$

$$P_1 \, dP_1 = m_1 \, dE_1$$

one obtains

$$J = \frac{\partial(E_{1-23}, \Omega_{1-23}, \Omega_{2-3})}{\partial(E_1, \Omega_1, \Omega_2)} = \frac{m_1 P_1 P_2^2}{\mu_{1-23} P_{1-23} P_{2-3}^2} \frac{dP_2}{dP_{2-3}} \tag{8}$$

From the square of (eq. 6b)

$$\frac{P_{2-3}\, dP_{2-3}}{P_2\, dP_2} = 1 + \frac{m_2}{m_2+m_3} \frac{(\vec{P}_1 - \vec{P}) \cdot \vec{P}_2}{P_2^2} \tag{9}$$

then

$$J = \frac{M}{m_2} \frac{P_1 P_2^2}{P_{1-23} P_{2-3}} \frac{1}{A P_2 + P_1 \cos\theta_{12} - P \cos\theta_2} \qquad \text{with } A = \frac{m_2+m_3}{m_2} \tag{10}$$

If the U system is the SCM system ($\vec{P} = 0$)

$$J = J_1 = \frac{\partial(E_{1-23}, \Omega_{1-23}, \Omega_{2-3})}{\partial(E_1^c, \Omega_1^c, \Omega_2^c)} = \frac{M}{m_2} \frac{(P_2^c)^2}{P_{2-3}} \frac{1}{A P_2^c + P_1^c \cos\theta_{12}^c} \tag{11}$$

where θ_{12}^c is the angle between the momenta of particles 1 and 2.

If the U system is the LAB system

$$J = J' = \frac{\partial(E_{1-23}, \Omega_{1-23}, \Omega_{2-3})}{\partial(E_1^l, \Omega_1^l, \Omega_2^l)} = \frac{M}{m_2} \frac{P_1^l (P_2^l)^2}{P_{1-23} P_{2-3}} \frac{1}{A P_2^l + P_1^l \cos\theta_{12}^l - P_T \cos\theta_2^l} \tag{12}$$

then

$$J_L = \frac{\partial(E_1^c, \Omega_1^c, \Omega_2^c)}{\partial(E_1^l, \Omega_1^l, \Omega_2^l)} = \frac{\partial(E_1^c, \Omega_1^c, \Omega_2^c)}{\partial(E_{1-23}, \Omega_{1-23}, \Omega_{2-3})} \frac{\partial(E_{1-23}, \Omega_{1-23}, \Omega_{2-3})}{\partial(E_1^l, \Omega_1^l, \Omega_2^l)}$$

$$= \frac{P_1^l (P_2^l)^2}{P_1^c} \frac{1}{(P_2^c)^2} \frac{A P_2^c + P_1^c \cos\theta_{12}^c}{A P_2^l + P_1^l \cos\theta_{12}^l - P_T \cos\theta_2^l} \tag{13}$$

Similarly for the case in which the particle detected by detector 2 is first emitted:

From the relations

$$\vec{P}_{2-13} = \vec{P}_2 - \frac{m_2 \vec{P}}{M} \tag{14a}$$

$$\vec{P}_{1-3} = \vec{P}_1 + \frac{m_1}{m_1+m_3} (\vec{P}_2 - \vec{P}) \tag{14b}$$

$$d\vec{P}_{2-13}\, d\vec{P}_{1-3} = d\vec{P}_2\, d\vec{P}_1 \tag{15}$$

one can write

$$J_2 = \frac{m_1\, P_1^c\, (P_2^c)^2}{P_{2-13}\, P_{1-3}^2\, \mu_{2-13}} \frac{dP_2^c}{dP_{1-3}} \quad \text{with } \vec{P} = 0$$

$$= \frac{P_1^c\, P_2^c}{P_{1-3}} \frac{M}{m_2} \frac{1}{\frac{1}{A}\, {}^{c}P_2 + P_1^c \cos\theta_{12}^c} \tag{16}$$

For the case in which the undetected particle is first emitted:

From the relations

$$\vec{P}_{3-21} = \frac{m_2 + m_3}{M} \vec{P} \cdot (\vec{P}_1 + \vec{P}_2) \tag{17a}$$

$$\vec{P}_{2-1} = \frac{1}{m_1 + m_2} (m_1 \vec{P}_2 - m_2 \vec{P}_1) \tag{17b}$$

$$d\vec{P}_{3-21}\, d\vec{P}_{2-1} = d\vec{P}_1\, d\vec{P}_2 \tag{18}$$

one is able to write

$$J_3 = \frac{(P_2^c)^2\, P_1^c\, m_1}{\mu_{3-21}\, P_{3-21}\, P_{2-1}^2} \frac{dP_2^c}{dP_{2-1}}$$

$$= \frac{M}{m_3} \frac{P_1^c\, (P_2^c)^2}{P_3^c\, P_{2-1}} \frac{1}{\frac{1}{m_1+m_2} (m_1 P_2^c - m_2 P_1^c \cos\theta_{12}^c)} \tag{19}$$

APPENDIX D

COMPUTER PROGRAMME FOR CALCULATION OF G.D.S. FUNCTION

The computer programme presented below is for the calculation of the prediction of the generalized density of states function. It consists of a main programme and five subroutines. Their functions are listed here:

Main	Controlling the input and out information
Subroutine KINEM3	Three body kinematics
Subroutine INTENG	Internal energy curves calculation
Subroutine LABCMT	Kinematic variables transformed from the LAB system to the SCM and RCM systems
Subroutine J2JL	Calculation of the Jacobian J_2J_L in Appendix C
Subroutine DOSPN	Calculation of the function ρ in Section V-2

The meaning of the input variables and some of the output variables will be given below:

ZMOA	Mass of projectile in AMU
ZMTA	Mass of target in AMU
ZM1A	Mass of the particle detected by detector 1
ZM2A	Mass of the particle detected by detector 2
ZM3A	Mass of the undetected particle
TO	Kinetic energy of the projectile
AMUGM	The ratio of gram to AMU
AMUMEV	The ratio of MEV to AMU
ERGMEV	The ratio of MEV to erg.
HBAR	$\hbar$

AG1D	The angle of detector 1 in degrees
AG2D	The angle of detector 2 in degrees
EX	The excitation energy of the residual nucleus
RPSPN	Effective range of the singlet (n,p) system
ROSPP	Effective range of the singlet (p,p) system
ASPN	Scattering length of the singlet (n,p) system
ASPP	Scattering length of the singlet (p,p) system
A1PN,A1PP	Radius of nuclear interaction volume
E1PNS	Internal energy of the singlet (n,p) system
E1PNT	Internal energy of the triplet (n,p) system
E1PPS	Internal energy of the singlet (p,p) system
T1	Kinetic energy of the particle detected by detector 1
DELT	n,p scattering phase shift
T2+ T2-	The two solutions of the kinetic energy of the particle impinging on detector 2
T3+ T3-	The two solutions for the kinetic energy of the undetected particle
E123	Internal energy of the (2,3) system
E113+ E113-	The two solutions of the internal energy of the (1,3) system
E112+ E112-	The two solutions of the internal energy of the (1,2) system
AG3+ AG3-	The two solutions of the angle of the undetected particle
XN+ XN-	Two branches of prediction of the differential cross-section by the Generalized density-of-states function in arbitrary units.

```
      COMMON R2N(51),S2N(51),U2N(51),ZMU1G,ZMU2G,ZMU3G,ZKZI,DD(51),ZK1,
     1D1,P11,DELTA1,SQP3P(51),SQP3N(51),Q12(51),Q1(51),Q2(51),Q3(51),
     2Q4(51),Q5(51),Q6(51),Q7(51),Q8(51),Q9(51),P2C3P(51),P2C3N(51),
     3Q10(51),Q11(51),PU1C(51),V3NC(51),R2P(51),S2P(51),U2P(51),J2JLP(51
     4),C2(51),C1P(51),C1N(51),C3P(51),C3N(51),C1,C4,C3,F1(51),G1(51),
     5F2P(51),F2N(51),G2P(51),G2N(51),X1(51),X2(51),X3(51),X4(51),X5(51)
     6,X6(51),X7(51),X8(51),X9(51),X10(51),ZMOG,PU2PC(51)
     7,F3P(51),F3N(51),G3P(51),G3N(51)
      COMMON T1(51),ZMO,ZMT,ZM1,ZM2,ZM3,EX,EO,PO,ROOT(51),P1(51),AG1R,AG
     12R,P2P(51),P2N(51),P3P(51),P3N(51),ZM1G,ZM2G,ZM3G,ZMGOT,TO,T2P(51)
     2,T2N(51),T3P(51),T3N(51),VCM,ZMG,P1C3P(51),P2PC(51),P1C3N(51),P2NC
     3(51),P1C(51),E11,AB,Z,PI,RO,A1,XMU,EI13N(51),ERGMEV,HBAR,E3N(51),
     4DELT(100),PU2NC(51),VO,PUO,ELAB(51),THOX(51),J2JLN(51),CC,THO(51),
     5P(51),PD(51),DEL(51),DELTR(51),AG,    ZM13,ZM23,ZM12, EI23(51),
     6EI13P(51),EI12P(51),EI12N(51),E1(51),E2P(51),E2N(51),E3P(51),
     7AG1D,AG2D,AG3RP(51),AG3RN(51),AG1RC(51),AG2RPC(51),AG2RNC(51),
     8AG3DP(51),AG3DN(51),BASE3P(51),BASE3N(51),BPHI3P(51),BPHI3N(51),
     9AG3RPC(51),AG3RNC(51),IIN,IN,I
      DOUBLE PRECISION ZMOA,ZMTA,ZM1A,ZM2A,ZM3A,AMUGM,AMUMEV,TO,EO,PO,ZM
     10,ZMT,ZM1,ZM2,ZM3,ZMOG,ZMTG,ZM1G,ZM2G,ZM3G,ZMAG,ZMG,ZMU1G,ZMU2G,ZM
     2U3G,PI,ROSPN,ROSPP,ERGMEV,HBAR,T1,EX,ROOT,P1,AG1R,AG2R,AG
     3,P2P,P2N,P3P,P3N,ZMGOT,TO,T2P,T2N,T3P,E(51),A1,XMU,ELAB,P,PD,
     4T3N,C,AA,V,VCM,P1C3P,P2PC,P1C3N,P2NC,Z,E1PNS,P1C,  ZM13,ZM23,ZM12,
     5E1PNT,E1PPS,XMUPNG,XMUPPG,RO,  ASPN,ASPP,A1PN,A1PP,DELT,EI13N
     6,DEL,VO,PUO,XN2N,PU2NC,THOX,THO,J2JLN,E1,E2P,E2N,E3P,E3N
     7,CC,DELTR,EI23,EI13P,EI12N,EI12P,XN2N(100),AB,E11,
     8R2N,S2N,U2N,ZKZI,DD,ZK1,D1,P11,DELTA1,XN2P(100),PU2PC
      DOUBLE PRECISION SQP3P,SQP3N,Q12,Q11,Q1,Q2,Q3,Q4,Q5,Q6,Q7,Q8,Q9,
     1P2C3P,P2C3N,Q10,PU1C,V3NC,R2P,S2P,U2P,J2JLP,C2,C1P,C1N,C3P,C3N
     2,C1,C4,C3,F1,G1,F2P,F2N,G2P,G2N,X1,X2,X3,X4,X5,X6,X7,X8,X9,X10
     3,F3P,F3N,G3P,G3N
1000  READ (5,101)ZMOA,ZMTA,ZM1A,ZM2A,ZM3A,TC
 101  FORMAT(5F12.9,F8.3)
      READ (5,102)AMUGM,AMUMEV,ERGMEV,HBAR
 102  FORMAT(D12.4,10X,F7.3,10X,D11.4,10X,D11.4)
      READ (5,103)AG1D,AG2D,EX
 103  FORMAT(2F8.3,F10.3)
      ZMO=ZMOA*AMUMEV
      ZMT=ZMTA*AMUMEV
      ZM1=ZM1A*AMUMEV
      ZM2=ZM2A*AMUMEV
      ZM3=ZM3A*AMUMEV
      ZMOG=ZMOA*AMUGM
      ZMTG=ZMTA*AMUGM
      ZM1G=ZM1A*AMUGM
      ZM2G=ZM2A*AMUGM
      ZM3G=ZM3A*AMUGM
      ZMGOT=ZMOG+ZMTG
      ZM13=ZM1+ZM3
      ZM23=ZM2+ZM3
      ZM12=ZM1+ZM2
      EO=TO+ZMO
      PO=DSQRT(EO**2-ZMO**2)
      VO=PO/ZMOG
```

```
      ZMUAG=(ZMOG/(ZMOG+ZMTG))*ZMTG
      PUO=ZMUAG*VO
      ZMG=ZM1G+ZM2G+ZM3G
      ZMU1G=(ZM1G/ZMG)*(ZM2G+ZM3G)
      ZMU2G=(ZM2G/ZMG)*(ZM1G+ZM3G)
      ZMU3G=(ZM3G/ZMG)*(ZM1G+ZM2G)
      PI=3.1415927
      AG1R=AG1D*1.74533D-2
      AG2R=AG2D*1.74533D-2
      AG=AG1R+AG2R
      READ (5,104)ROSPN,ROSPP
  104 FORMAT(D10.3,10X,D10.3)
      READ (5,105)ASPN,ASPP
  105 FORMAT(D11.3,9X,D11.3)
      READ (5,106)A1PN,A1PP
  106 FORMAT (D10.3,10X,D10.3)
      READ (5,107)IN,N
  107 FORMAT(2I5)
      DO 700 I=1,IN
      T1(I)=0.0
      P2P(I)=0.0
      SQP3P(I)=0.0
      BASE3P(I)=0.0
      BPHI3P(I)=0.0
      P2N(I)=0.0
      SQP3N(I)=0.0
      BASE3N(I)=0.0
      BPHI3N(I)=0.0
      C2(I)=0.0
      C1P(I)=0.0
      C1N(I)=0.0
      C3P(I)=0.0
      C3N(I)=0.0
      P3P(I)=0.0
      P3N(I)=0.0
      EI23(I)=0.0
      T2P(I)=0.0
      EI13P(I)=0.0
      EI12P(I)=0.0
      AG3DP(I)=0.0
      T2N(I)=0.0
      EI13N(I)=0.0
      EI12N(I)=0.0
      AG3DN(I)=0.0
      T3P(I)=0.0
      T3N(I)=0.0
      P2PC(I)=0.0
      P1C3N(I)=0.0
      AG1RC(I)=0.0
      AG2RNC(I)=0.0
      PU2NC(I)=0.0
      P1(I)=0.0
      Q12(I)=0.0
      Q1(I)=0.0
```

```
      Q2(I)=0.0
      AG2RPC(I)=0.0
      Q3(I)=0.0
      Q4(I)=0.0
      AG3RPC(I)=0.0
      AG3RNC(I)=0.0
      Q5(I)=0.0
      Q6(I)=0.0
       Q7(I)=0.0
       Q8(I)=0.0
       Q9(I)=0.0
      P1C3P(I)=0.0
      P2C3P(I)=0.0
      P2C3N(I)=0.0
      Q10(I)=0.0
      Q11(I)=0.0
      PU1C(I)=0.0
      V3NC(I)=0.0
      F1(I)=0.0
      G1(I)=0.0
      F2P(I)=0.0
      F2N(I)=0.0
      G2P(I)=0.0
      G2N(I)=0.0
      P2NC(I)=0.0
      F3N(I)=0.0
      F3P(I)=0.0
      G3N(I)=0.0
      G3P(I)=0.0
      R2N(I)=0.0
      S2N(I)=0.0
      U2N(I)=0.0
      J2JLN(I)=0.0
      R2P(I)=0.0
      S2P(I)=0.0
      U2P(I)=0.0
      J2JLP(I)=0.0
      THO(I)=0.0
      DELTR(I)=0.0
      P(I)=0.0
      ELAB(I)=0.0
      DEL(I)=0.0
      PD(I)=0.0
      XN2N(I)=0.0
      DD(I)=0.0
  700 CONTINUE
      READ (5,108)(T1(I),I=1,IN)
  108 FORMAT( 10F7.2)
      READ (5,112)(DELT(I),I=1,N)
  112 FORMAT(10F7.2)
      C=2.99793D10
      AA=DSQRT((TO+ZMO)**2-ZMO**2)
      V=AA/(TO+ZMO+ZMT)
      VCM=V*C
```

```
      Z=1.6020D-6/C
      READ (5,109)E1PNS,E1PNT,E1PPS
  109 FORMAT(3F7.3)
      XMUPNG=ZM1G*(ZM3G/(ZM1G+ZM3G))
      XMUPPG=ZM1G*(ZM2G/(ZM1G+ZM2G))
      E11=E1PNS
      WRITE(6,606)AG1R,AG2R,AG
  606 FORMAT(1H ,1PD13.5,5H=AG1R,D13.5,5H=AG2R,D13.5,3H=AG)
       WRITE(6,607)
  607 FORMAT(1H1,50HT1,P2P,SQP3P,BASE3P,BPHI3P,P2N,SQP3N,BASE3N,BPHI3N )
      DO 610 I=1,IN
      CALL KINEM3
      WRITE(6,608)T1(I),P2P(I),SQP3P(I),BASE3P(I),BPHI3P(I),P2N(I),SQP3N
     1(I),BASE3N(I),BPHI3N(I)
  608 FORMAT(1H ,F8.3,2(1PD13.5),2(1PE13.5),4(1PD13.5))
  610 CONTINUE
      WRITE(6,609)
  609 FORMAT(1H1,21HT1,C2,C1P,C1N,C3P,C3N,16H,P2P,P2N,P3P,P3N)
      DO 611 I=1,IN
      CALL INTENG
      WRITE(6,612)T1(I),C2(I),C1P(I),C1N(I),C3P(I),C3N(I),P2P(I),P2N(I),
     1P3P(I),P3N(I)
  612 FORMAT(1H ,F8.3,9(1PD13.5))
  611 CONTINUE
      WRITE(6,116)AG1D,EX
  116 FORMAT(1H1,7HTHETA1=,F6.2,5X,          5X,3HEX=,F8.4,5X,8HD(P,2P)N)
      WRITE(6,117)AG2D,E11
  117 FORMAT(1H ,7HTHETA2=,F6.2,5X,16HINTERNAL ENERGY=,F7.3,5H(MEV))
      WRITE(6,118)
  118 FORMAT(16X,2HT1,8X,4HEI23,6X,3HT2&,7X,5HEI13&,5X,5HEI12&,5X,4HAG3&
     1,6X,3HT2-,7X,5HEI13-,5X,5HEI12-,5X,4HAG3-,5X,3HT3&,7X,3HT3-)
      DO 119 I=1,IN
      IF (ROOT(I))120,121,121
  120 WRITE(6,122)T1(I)
  122 FORMAT(10X,F10.3,9(6X,4HIMAG))
      GO TO 119
  121 WRITE(6,123)T1(I),EI23(I),T2P(I),EI13P(I),EI12P(I),AG3DP(I),T2N(I)
     1,EI13N(I),EI12N(I),AG3DN(I),T3P(I),T3N(I)
  123 FORMAT (10X,12F10.3)
  119 CONTINUE
      WRITE(6,124)ZMT,ZMO,ZM1,ZM2,ZM3,TC
  124 FORMAT (1H ,4HZMT=,F12.5,6X,4HZMO=,F12.5,6X,4HZM1=,F12.5,6X,4HZM2=
     1,F12.5,6X,4HZM3=,F12.5,6X,3HTC=,F12.3)
      WRITE(6,131)
  131 FORMAT(1H1,39HT1,P2PC,P1C3N,AG1RC,AG2RNC,PU2NC,P1,P2N)
      WRITE(6,613)
  613 FORMAT(1H ,5X,42HQ12,Q1,Q2,AG2RPC,Q3,Q4,AG3RPC,AG3RNC,Q5,Q6   )
      WRITE(6,614)
  614 FORMAT(1H ,10X,44HQ7,Q8,Q9,P1C3P,P2C3P,P2C3N,Q10,Q11,PU1C,V3NC    )
      WRITE(6,619)
  619 FORMAT(1H ,30HF1,G1,F2P,F2N,G2P,G2N,P2P,P2NC)
      WRITE(6,621)
  621 FORMAT(1H ,15HF3N,F3P,G3N,G3P)
      DO 130 I=1,IN
```

```
      CALL LABCMT
      WRITE(6,132)T1(I),P2PC(I),P1C3N(I),AG1RC(I),AG2RNC(I),PU2NC(I),
     1P1(I),P2N(I)
  132 FORMAT(1H ,F8.3,2(1PD13.5),2(1PE13.5),3(1PD13.5))
      WRITE(6,615)Q12(I),Q1(I),Q2(I),AG2RPC(I),Q3(I),Q4(I),AG3RPC(I),
     1AG3RNC(I),Q5(I),Q6(I)
  615 FORMAT(1H ,5X,10(1PD12.4))
      WRITE(6,616)Q7(I),Q8(I),Q9(I),P1C3P(I),P2C3P(I),P2C3N(I),Q10(I),Q
     111(I),PU1C(I),V3NC(I)
  616 FORMAT(1H ,8X,10(1PD12.4))
      WRITE(6,620)F1(I),G1(I),F2P(I),F2N(I),G2P(I),G2N(I),P2P(I),P2NC(I)
  620 FORMAT(1H ,8X,8(1PD12.4))
      WRITE(6,622)F3N(I),F3P(I),G3N(I),G3P(I)
  622 FORMAT(1H ,8X,4(1PD12.4))
  130 CONTINUE
      WRITE(6,617)
  617 FORMAT(1H ,8HC1,C4,C3)
      WRITE(6,618)C1,C4,C3
  618 FORMAT(1H ,3(1PD13.5))
      WRITE(6,133)
  133 FORMAT(1H1,38HT1,R2N,S2N,U2N,J2JLN,R2P,S2P,U2P,J2JLP    )
      DO 134 I=1,IN
      CALL J2JL
      WRITE(6,135)T1(I),R2N(I),S2N(I),U2N(I),J2JLN(I),R2P(I),S2P(I),U2P(
     1I),J2JLP(I)
  135 FORMAT(1H ,F8.3,8(1PD13.5))
  134 CONTINUE
      RO=ROSPN
      AB=ASPN
      A1=A1PN
      E11=E11*ERGMEV
      XML=XMUPNG
      WRITE(6,605)XMUPNG,XMU,ZM1G,ZM3G,AMUGM
  605 FORMAT(1H ,7HXMUPNG=,1PD13.5,5X,4HXMU=,D13.5,5X,5HZM1G=,D13.5,5X,
     15HZM3G=,D13.5,5X,6HAMUGM=,D13.5)
      WRITE(6,127)
  127 FORMAT(1H1,10HEI13-(MEV),2X,10HTHO(1/MEV), 2X,13HDELTA(RADIAN),3X,
     111HPHI(RADIAN), 2X,9HELAB(MEV),7X,10HDELTA(DEG),5X,8HPHI(DEG),12X,
     23HXN-,12X,3HXN&)
      CONST2=(ZMUAG/((2.0D0*PI)**3*HBAR))*(ZMU2G/HBAR)
      DO 115 I=1,IN
      CALL DOSPN
      XN2P(I)=CONST2*(PU2PC(I)/PUO)*J2JLP(I)*THOX(I)
      XN2N(I)=CONST2*(PU2NC(I)/PUO)*J2JLN(I)*THOX(I)
      WRITE(6,129)EI13N(I),THO(I),DELTR(I),P(I),ELAB(I),DEL(I),PD(I),
     1XN2N(I),XN2P(I)
  129 FORMAT(1H ,F6.3,5X,1PD10.3,2X,1PD13.5,2X,1PD13.5,2X,0PF8.3,5X,1PD1
     113.5,3X,D13.5,D16.6,2X,D16.6)
  115 CONTINUE
      WRITE(6,125)RO,AB,A1,CONST2,PUO
  125 FORMAT(1H ,3HRO=,1PD12.4,4H(CM),5X,2HA=,1PD12.4,4H(CM),5X,3HA1=,1P
     1D12.4,4H(CM),5X,7HCONST2=, D13.5,5X,4HPUC=, D13.5)
      WRITE(6,126)ZM2A,HBAR,CC,ZKZI
  126 FORMAT(1H ,5HZM2A=,F11.8,5H(AMU),5X,5HHBAR=,1PD11.4,9H(ERG-SEC),5X
```

```
     1,3HCC=,1PD11.4,5X,5HZKZI=,D11.4)
       WRITE (6,603)
603    FORMAT(1H ,17HZK1,D1,P11,DELTA1          )
       WRITE(6,602)ZK1,D1,P11,DELTA1
602    FORMAT(1H ,4(1PD13.5))
       WRITE(6,604)XMU,E11
604    FORMAT (1H ,4HXMU=,1PD13.5,4HE11=,1PD13.5)
       DO 601 I=1,IN
       WRITE (6,600)DD(I)
600    FORMAT(1H ,9(1PD13.5))
601    CONTINUE
       GO TO 1000
       END
```

AL MEMORY REQUIREMENTS 0023B2 BYTES

```
      SUBROUTINE KINEM3
      COMMON R2N(51),S2N(51),U2N(51),ZMU1G,ZMU2G,ZMU3G,ZKZI,DD(51),ZK1,
     1D1,P11,DELTA1,SQP3P(51),SQP3N(51),Q12(51),Q1(51),Q2(51),Q3(51),
     2Q4(51),Q5(51),Q6(51),Q7(51),Q8(51),Q9(51),P2C3P(51),P2C3N(51),
     3Q10(51),Q11(51),PU1C(51),V3NC(51),R2P(51),S2P(51),U2P(51),J2JLP(51
     4),C2(51),C1P(51),C1N(51),C3P(51),C3N(51),C1,C4,C3,F1(51),G1(51),
     5F2P(51),F2N(51),G2P(51),G2N(51),X1(51),X2(51),X3(51),X4(51),X5(51)
     6,X6(51),X7(51),X8(51),X9(51),X10(51),ZMOG,PU2PC(51)
     7,F3P(51),F3N(51),G3P(51),G3N(51)
      COMMON T1(51),ZMO,ZMT,ZM1,ZM2,ZM3,EX,EO,PC,RCOT(51),P1(51),AG1R,AG
     12R,P2P(51),P2N(51),P3P(51),P3N(51),ZM1G,ZM2G,ZM3G,ZMGOT,TO,T2P(51)
     2,T2N(51),T3P(51),T3N(51),VCM,ZMG,P1C3P(51),P2PC(51),P1C3N(51),P2NC
     3(51),P1C(51),E11,AB,Z,PI,RO,A1,XMU,EI13N(51),ERGMEV,HBAR,E3N(51),
     4DELT(100),PU2NC(51),VO,PUO,ELAB(51),THOX(51),J2JLN(51),CC,THO(51),
     5P(51),PD(51),DEL(51),DELTR(51),AG,    ZM13,ZM23,ZM12, EI23(51),
     6EI13P(51),EI12P(51),EI12N(51),E1(51),E2P(51),E2N(51),E3P(51),
     7AG1D,AG2D,AG3RP(51),AG3RN(51),AG1RC(51),AG2RPC(51),AG2RNC(51),
     8AG3DP(51),AG3DN(51),BASE3P(51),BASE3N(51),BPHI3P(51),BPHI3N(51),
     9AG3RPC(51),AG3RNC(51),IIN,IN,I
      DIMENSION PHI3RP(51),PHI3DP(51),PHI3RN(51),PHI3DN(51)
      DOUBLE PRECISION AG,E1,AG ,A(51),B(51),C(51),D(51),F(51),G(51),
     1T1,ZMO,ZMT,ZM1,ZM2,ZM3,EX,EO,PO,RCOT,P1,AG1R,AG2R,P2P,P2N,P3P,P3N,
     2ZM1G,ZM2G,ZM3G,ZMGOT,TO,T2P,T2N,T3P,T3N,VCM,ZMG,P1C3P,P2PC,P1C3N,
     3P2NC,P1C,E11, Z,PI,RO,  A1,E, XMU,EI13N,ERGMEV,HBAR,DELT,PU2NC,VO,
     4PUO,ELAB,THOX,J2JLN,CC,THO,P,PD,DEL,DELTR,AB,ZM13,ZM23,ZM12,EI23,E
     5I12P,EI12N,EI13P,      H(51),E2P,SQP3P     ,E3P,E2N,SQP3N     ,E3N,
     6R2N,S2N,U2N,ZMU1G,ZMU2G,ZMU3G,ZKZI,DD,ZK1,D1,P11,DELTA1,ZMOG
      DOUBLE PRECISION Q12,Q1,Q2,Q3,Q4,Q5,Q6,Q7,Q8,Q9,P2C3P,P2C3N,Q10,
     1Q11,PU1C,V3NC,R2P,S2P,U2P,J2JLP,C2,C1P,C1N,C3P,C3N
     2,C1,C4,C3,F1,G1,F2P,F2N,G2P,G2N,X1,X2,X3,X4,X5,X6,X7,X8,X9,X10
     3,F3P,F3N,G3P,G3N,PU2PC
      E1(I)=T1(I)+ZM1
      P1(I)=DSQRT(E1(I)**2-ZM1**2)
      A(I)=P1(I)*DCOS(AG)-PO*DCOS(AG2R)
      B(I)=PO**2+P1(I)**2+ZM3**2-2.0DO*PO*P1(I)*DCOS(AG1R)
      C(I)=ZM2**2+(ZMT+EO-E1(I)-EX)**2-B(I)
      D(I)=-2.0DO*(ZMT+EO-E1(I)-EX)
      F(I)=4.0DO*A(I)**2-D(I)**2
      G(I)=-2.0DO*C(I)*D(I)
      H(I)=-4.0DO*A(I)**2*ZM2**2-C(I)**2
      ROOT(I)=G(I)**2-4.0*F(I)*H(I)
      IF (ROOT(I))1,2,2
    2 E2P(I)=(-G(I)+DSQRT(G(I)**2-4.0DO*F(I)*H(I)))/(2.0DO*F(I))
      T2P(I)=E2P(I)-ZM2
      IF (T2P(I))3,4,4
    4 P2P(I)=DSQRT(E2P(I)**2-ZM2**2)
      SQP3P(I)=PO**2+P1(I)**2+P2P(I)**2-2.0DO*PO*(P1(I)*DCOS(AG1R)+P2P(I
     1)*DCOS(AG2R))+2.0*DO*P1(I)*P2P(I)*DCOS(AG)
      P3P(I)=DSQRT(SQP3P(I))
      E3P(I)=DSQRT(SQP3P(I)+ZM3**2)
      T3P(I)=E3P(I)-ZM3
      BASE3P(I)=SNGL((PC-P1(I)*DCOS(AG1R)-P2P(I)*DCOS(AG2R))/P3P(I))
      IF (ABS(BASE3P(I))-1.0)5,5,6
    5 AG3RP(I)=ARCCS(BASE3P(I))
```

```
AN IV G LEVEL 1, MOD 1          KINEM3          DATE = 68202          01/01/14

      AG3DP(I)=AG3RP(I)*57.2957795
      BPHI3P(I)=SNGL((-P1(I)*DSIN(AG1R)+P2P(I)*DSIN(AG2R))/(P3P(I)*DSIN(
     1DBLE(AG3RP(I))))
    6 IF (ABS(BPHI3P(I))-1.0)7,7,3
    7 PHI3RP(I)=ARSIN(BPHI3P(I))
      PHI3DP(I)=PHI3RP(I)*57.2957795
    3 E2N(I)=(-G(I)-DSQRT(G(I)**2-4.0D0*F(I)*H(I)))/(2.0D0*F(I))
      T2N(I)=E2N(I)-ZM2
      IF (T2N(I))1,8,8
    8 P2N(I)=DSQRT(E2N(I)**2-ZM2**2)
      SQP3N(I)=P0**2+P1(I)**2+P2N(I)**2-2.0D0*P0*(P1(I)*DCOS(AG1R)+P2N(I
     1)*DCOS(AG2R))+2.0D0*P1(I)*P2N(I)*DCOS(AG)
      P3N(I)=DSQRT(SQP3N(I))
      E3N(I)=DSQRT(SQP3N(I)+ZM3**2)
      T3N(I)=E3N(I)-ZM3
      BASE3N(I)=SNGL((P0-P1(I)*DCOS(AG1R)-P2N(I)*DCOS(AG2R))/P3N(I))
      IF (ABS(BASE3N(I))-1.0)9,9,10
    9 AG3RN(I)=ARCOS(BASE3N(I))
      AG3DN(I)=AG3RN(I)*57.2957795
      BPHI3N(I)=SNGL((-P1(I)*DSIN(AG1R)+P2N(I)*DSIN(AG2R))/(P3N(I)*DSIN(
     1DBLE(AG3RN(I))))
   10 IF (ABS(BPHI3N(I))-1.0)11,11,1
   11 PHI3RN(I)=ARSIN(BPHI3N(I))
      PHI3DN(I)=PHI3RN(I)*57.2957795
    1 RETURN
      END

AL MEMORY REQUIREMENTS 001A2A BYTES
```

```
      SUBROUTINE INTENG
      COMMON R2N(51),S2N(51),U2N(51),ZMU1G,ZMU2G,ZMU3G,ZKZI,DD(51),ZK1,
     1D1,P11,DELTA1,SQP3P(51),SQP3N(51),Q12(51),Q1(51),Q2(51),Q3(51),
     2Q4(51),Q5(51),Q6(51),Q7(51),Q8(51),Q9(51),P2C3P(51),P2C3N(51),
     3Q10(51),Q11(51),PU1C(51),V3NC(51),R2P(51),S2P(51),U2P(51),J2JLP(51
     4),C2(51),C1P(51),C1N(51),C3P(51),C3N(51),C1,C4,C3,F1(51),G1(51),
     5F2P(51),F2N(51),G2P(51),G2N(51),X1(51),X2(51),X3(51),X4(51),X5(51)
     6,X6(51),X7(51),X8(51),X9(51),X10(51),ZMOG,PU2PC(51)
     7,F3P(51),F3N(51),G3P(51),G3N(51)
      COMMON T1(51),ZMO,ZMT,ZM1,ZM2,ZM3,EX,EO,PO,ROOT(51),P1(51),AG1R,AG
     12R,P2P(51),P2N(51),P3P(51),P3N(51),ZM1G,ZM2G,ZM3G,ZMGOT,TO,T2P(51)
     2,T2N(51),T3P(51),T3N(51),VCM,ZMG,P1C3P(51),P2PC(51),P1C3N(51),P2NC
     3(51),P1C(51),E11,AB,Z,PI,RO,A1,XMU,EI13N(51),ERGMEV,HBAR,E3N(51),
     4DELT(100),PU2NC(51),VO,PUO,ELAB(51),THOX(51),J2JLN(51),CC,THO(51),
     5P(51),PD(51),DEL(51),DELTR(51),AG,    ZM13,ZM23,ZM12, EI23(51),
     6EI13P(51),EI12P(51),EI12N(51),E1(51),E2P(51),E2N(51),E3P(51),
     7AG1D,AG2D,AG3RP(51),AG3RN(51),AG1RC(51),AG2RPC(51),AG2RNC(51),
     8AG3DP(51),AG3DN(51),BASE3P(51),BASE3N(51),BPHI3P(51),BPHI3N(51),
     9AG3RPC(51),AG3RNC(51),IIN,IN,I
      DOUBLE PRECISION C2    ,C1P    ,E,  EI23,EI13P,EI12P,EI12N,T1,ZMO,
     1ZMT,ZM1,ZM2,ZM3,EX,EO,PO,ROOT,P1,AG1R,AG2R,P2P,P2N,P3P,P3N,ZM1G,
     2ZM2G,ZM3G,ZMGOT,TO,T2P,T2N,T3P,T3N,VCM,ZMG,P1C3P,P2PC,P1C3N,P2NC,
     3P1C,E11, Z,PI,RO,  A1,   XMU,EI13N,ERGMEV,HBAR,DELT,PU2NC,VO,PUO,
     4ELAB,THOX,J2JLN,CC,THO,P,PD,DEL,DELTR,AB,ZM13,ZM23,ZM12,AG,
     5EI23,EI12P,EI12N,EI13P,C1N    ,C3P    ,C3N    ,E1,E2P,E2N,E3P,E3N,
     6R2N,S2N,U2N,ZMU1G,ZMU2G,ZMU3G,ZKZI,DD,ZK1,D1,P11,DELTA1,ZMOG
      DOUBLE PRECISION SQP3P,SQP3N,Q12,Q11,Q1,Q2,Q3,Q4,Q5,Q6,Q7,Q8,Q9,
     1P2C3P,P2C3N,Q10,PU1C,V3NC,R2P,S2P,U2P,J2JLP,C2,C1P,C1N,C3P,C3N
     2,C1,C4,C3,F1,G1,F2P,F2N,G2P,G2N,X1,X2,X3,X4,X5,X6,X7,X8,X9,X10
     3,F3P,F3N,G3P,G3N,PU2PC
      IF (ROOT(I))20,21,21
   21 X1(I)=P1(I)**2+PO**2
      X2(I)=2.0D0*PO*P1(I)*DCOS(AG1R)
      C2(I)=DSQRT(X1(I)-X2(I)+ZM23**2)
      X3(I)=PO**2+P2P(I)**2
      X4(I)=2.0D0*PO*P2P(I)*DCOS(AG2R)
      C1P(I)=DSQRT(X3(I)-X4(I)+ZM13**2)
      X5(I)=PO**2+P2N(I)**2
      X6(I)=2.0D0*PO*P2N(I)*DCOS(AG2R)
      C1N(I)=DSQRT(X5(I)-X6(I)+ZM13**2)
      X7(I)=P3P(I)**2+PO**2
      X8(I)=2.0D0*PO*P3P(I)*COS(AG3RP(I))
      C3P(I)=DSQRT(X7(I)-X8(I)+ZM12**2)
      X9(I)=P3N(I)**2+PO**2
      X10(I)=2.0D0*PO*P3N(I)*COS(AG3RN(I))
      C3N(I)=DSQRT(X9(I)-X10(I)+ZM12**2)
      EI23(I)=EO-E1(I)-C2(I)+ZMT
      EI13P(I)=EO-E2P(I)-C1P(I)+ZMT
      EI13N(I)=EO-E2N(I)-C1N(I)+ZMT
      EI12P(I)=EO-E3P(I)-C3P(I)+ZMT
      EI12N(I)=EO-E3N(I)-C3N(I)+ZMT
   20 RETURN
      END
```

```
      SUBROUTINE LABCMT
      COMMON R2N(51),S2N(51),U2N(51),ZMU1G,ZMU2G,ZMU3G,ZKZI,DD(51),ZK1,
     1D1,P11,DELTA1,SQP3P(51),SQP3N(51),Q12(51),Q1(51),Q2(51),Q3(51),
     2Q4(51),Q5(51),Q6(51),Q7(51),Q8(51),Q9(51),P2C3P(51),P2C3N(51),
     3Q10(51),Q11(51),PU1C(51),V3NC(51),R2P(51),S2P(51),U2P(51),J2JLP(51
     4),C2(51),C1P(51),C1N(51),C3P(51),C3N(51),C1,C4,C3,F1(51),G1(51),
     5F2P(51),F2N(51),G2P(51),G2N(51),X1(51),X2(51),X3(51),X4(51),X5(51)
     6,X6(51),X7(51),X8(51),X9(51),X10(51),ZMOG,PU2PC(51)
     7,F3P(51),F3N(51),G3P(51),G3N(51)
      COMMON T1(51),ZMO,ZMT,ZM1,ZM2,ZM3,EX,EC,PC,ROOT(51),P1(51),AG1R,AG
     12R,P2P(51),P2N(51),P3P(51),P3N(51),ZM1G,ZM2G,ZM3G,ZMGOT,TO,T2P(51)
     2,T2N(51),T3P(51),T3N(51),VCM,ZMG,P1C3P(51),P2PC(51),P1C3N(51),P2NC
     3(51),P1C(51),E11,AB,Z,PI,RG,A1,XMU,EI13N(51),ERGMEV,HBAR,E3N(51),
     4DELT(100),PU2NC(51),VO,PUO,ELAB(51),THOX(51),J2JLN(51),CC,THO(51),
     5P(51),PD(51),DEL(51),DELTR(51),AG,    ZM13,ZM23,ZM12, EI23(51),
     6EI13P(51),EI12P(51),EI12N(51),E1(51),E2P(51),E2N(51),E3P(51),
     7AG1D,AG2D,AG3RP(51),AG3RN(51),AG1RC(51),AG2RPC(51),AG2RNC(51),
     8AG3DP(51),AG3DN(51),BASE3P(51),BASE3N(51),BPHI3P(51),BPHI3N(51),
     9AG3RPC(51),AG3RNC(51),IIN,IN,I
      DIMENSION AG1DC(51),AG2DPC(51),AG2DNC(51),
     1AG3DPC(51),AG3DNC(51)
      DOUBLE PRECISION C1,C4,C3,F1    ,F2P    ,F2N    ,G2P    ,AG, P2PC,
     1G2N    ,F3P    ,F3N    ,G3P    ,G3N    ,P3PC(51),P3NC(51),P1C3P,P
     21C3N,P2C3N    ,P2C3P    ,P1C2P(51),P1C2N(51),V1C(51),PU1C    ,E
     3,AG1R,AG2R,P2P,P2N,P3P,P3N,ZM1G,ZM2G,ZM3G,ZMGOT,TO,T2P,T2N,T3P,T3N
     4,VCM,ZMG,P1C3P,P2PC,P1C3N,P2NC,P1C,E11, Z,PI,RG,  A1,T1,XMU,EI13N,
     5ERGMEV,HBAR,DELT,PU2NC,VO,PUO,ELAB,THOX,J2JLN,CC,THO,P,PD,DEL,
     6DELTR,   ZM13,ZM23,ZM12,   EI23,EI12P,EI12N,EI13P,V2PC(51),V2NC(51
     7),PU2PC    ,V3PC(51),V3NC    ,PU3PC(51),PU3NC(51),G1    ,Q1    ,
     8ZMO,ZMT,ZM1,ZM2,ZM3,EX,EO,PC,ROOT,P1,AB,E3N,E1,E2P,E2N,E3P,Q2    ,
     9Q3,Q4,Q5,Q6,Q7,Q8,Q9,Q10,Q11
      DOUBLE PRECISION R2N,S2N,U2N,Q12    ,ZMU1G,ZMU2G,ZMU3G,ZKZI,DD,ZK1
     1,D1,P11,DELTA1,SQP3P,SQP3N,R2P,S2P,U2P,J2JLP,C2,C1P,C1N,C3P,C3N
     2,X1,X2,X3,X4,X5,X6,X7,X8,X9,X10,ZMOG
      C1=DSQRT(ZM1G)*DSQRT(ZMOG*TO)/ZMGOT
      C4=DSQRT(ZM2G)*DSQRT(ZMOG*TO)/ZMGOT
      C3=DSQRT(ZM3G)*DSQRT(ZMOG*TO)/ZMGOT
      IF (ROOT(I))30,31,31
   31 F1(I)=DSQRT(T1(I))*DCOS(AG1R)-C1
      Q12(I)=T1(I)-2.0D0*C1*DSQRT(T1(I))*DCOS(AG1R)+C1**2
      IF(Q12(I))83,83,84
   84 G1(I)=DSQRT(Q12(I))
      AG1RC(I)=ARCOS(SNGL(F1(I)/G1(I)))
      AG1DC(I)=AG1RC(I)*57.2957795
   83 F2P(I)=DSQRT(T2P(I))*DCOS(AG2R)-C4
      F2N(I)=DSQRT(T2N(I))*DCOS(AG2R)-C4
      Q1(I)=T2P(I)-2.0D0*C4*DSQRT(T2P(I))*DCOS(AG2R)+C4**2
      IF(Q1(I))32,33,33
   33 G2P(I)=DSQRT(Q1(I))
   32 Q2(I)=T2N(I)-2.0D0*C4*DSQRT(T2N(I))*DCOS(AG2R)+C4**2
      IF(Q2(I))34,35,35
   35 G2N(I)=DSQRT(Q2(I))
   34 IF(G2P(I))75,75,76
   76 AG2RPC(I)=ARCOS(SNGL(F2P(I)/G2P(I)))
```

```
   75 IF(G2N(I))77,77,78
   78 AG2RNC(I)=ARCOS(SNGL(F2N(I)/G2N(I)))
   77 AG2DPC(I)=AG2RPC(I)*57.2957795
      AG2DNC(I)=AG2RNC(I)*57.2957795
      F3P(I)=DSQRT(T3P(I))*DBLE(COS(AG3RP(I)))-C3
      F3N(I)=DSQRT(T3N(I))*DBLE(COS(AG3RN(I)))-C3
      Q3(I)=T3P(I)-2.0D0*C3*DSQRT(T3P(I))*DBLE(COS(AG3RP(I)))+C3**2
      IF(Q3(I))36,37,37
   37 G3P(I)=DSQRT(Q3(I))
   36 Q4(I)=T3N(I)-2.0D0*C3*DSQRT(T3N(I))*DBLE(COS(AG3RN(I)))+C3**2
      IF(Q4(I))38,39,39
   39 G3N(I)=DSQRT(Q4(I))
   38 IF(G3P(I))82,82,79
   79 AG3RPC(I)=ARCOS(SNGL(F3P(I)/G3P(I)))
   82 IF(G3N(I))80,80,81
   81 AG3RNC(I)=ARCOS(SNGL(F3N(I)/G3N(I)))
   80 AG3DPC(I)=AG3RPC(I)*57.2957795
      AG3DNC(I)=AG3RNC(I)*57.2957795
      Q5(I)=(P1(I)*Z)**2+(ZM1G*VCM)**2-2.0D0*P1(I)*Z*ZM1G*VCM*DCOS(AG1R)
      IF(Q5(I))60,61,61
   61 P1C(I)=DSQRT(Q5(I))
   60 Q6(I)=(P2P(I)*Z)**2+(ZM2G*VCM)**2-2.0D0*P2P(I)*Z*ZM2G*VCM*DCOS(AG2
     1R)
      IF(Q6(I))62,63,63
   63 P2PC(I)=DSQRT(Q2(I))
   62 Q7(I)=(P2N(I)*Z)**2+(ZM2G*VCM)**2-2.0D0*P2N(I)*Z*ZM2G*VCM*DCOS(AG2
     1R)
      IF(Q7(I))64,65,65
   65 P2NC(I)=DSQRT(Q7(I))
   64 Q8(I)=(P3P(I)*Z)**2+(ZM3G*VCM)**2-2.0D0*P3P(I)*Z*ZM3G*VCM*DBLE(COS
     1(AG3RP(I)))
      IF(Q8(I))66,67,67
   67 P3PC(I)=DSQRT(Q8(I))
   66 Q9(I)=(P3N(I)*Z)**2+(ZM3G*VCM)**2-2.0D0*P3N(I)*Z*ZM3G*VCM*DBLE(COS
     1(AG3RN(I)))
      IF(Q9(I))68,69,69
   69 P3NC(I)=DSQRT(Q9(I))
   68 P1C3P(I)=DSQRT(P1C(I)**2+(ZM1G*P2PC(I)/(ZM1G+ZM2G))**2+2.0D0*P1C(I
     1)*P2PC(I)*(ZM1G/(ZM2G+ZM1G))*DCOS(AG1RC(I)+DBLE(AG2RPC(I))))
      P1C3N(I)=DSQRT(P1C(I)**2+(ZM1G*P2NC(I)/(ZM1G+ZM2G))**2+2.0D0*P1C(I
     1)*P2NC(I)*(ZM1G/(ZM2G+ZM1G))*DCOS(AG1RC(I)+DBLE(AG2RNC(I))))
      P2C3P(I)=DSQRT(P2PC(I)**2+(ZM2G*P1C(I)/(ZM2G+ZM3G))**2+2.0D0*P1C(I
     1)*P2PC(I)*(ZM2G/(ZM2G+ZM3G))*DCOS(AG1RC(I)+DBLE(AG2RPC(I))))
      P2C3N(I)=DSQRT(P2NC(I)**2+(ZM2G*P1C(I)/(ZM2G+ZM3G))**2+2.0D0*P1C(I
     1)*P2NC(I)*(ZM2G/(ZM2G+ZM3G))*DCOS(AG1RC(I)+DBLE(AG2RNC(I))))
      Q10(I)=ZM1G**2*P2PC(I)**2+ZM2G**2*P1C(I)**2-2.0D0*ZM1G*ZM2G*P2PC(I
     1)*P1C(I)*DCOS(AG1RC(I)+DBLE(AG2RPC(I)))
      IF(Q10(I))70,71,71
   71 P1C2P(I)=(1.0D0/(ZM1G+ZM2G))*DSQRT(Q10(I))
   70 Q11(I)=ZM1G**2*P2NC(I)**2+ZM2G**2*P1C(I)**2-2.0D0*ZM1G*ZM2G*P2NC(I
     1)*P1C(I)*DCOS(AG1RC(I)+DBLE(AG2RNC(I)))
      IF(Q11(I))72,73,73
   73 P1C2N(I)=(1.0D0/(ZM1G+ZM2G))*DSQRT(Q11(I))
   72 V1C(I)=P1C(I)/ZM1G
```

```
      PU1C(I)=ZMU1G*V1C(I)
      V2PC(I)=P2PC(I)/ZM2G
      V2NC(I)=P2NC(I)/ZM2G
      PU2PC(I)=ZMU2G*V2PC(I)
      PU2NC(I)=ZMU2G*V2NC(I)
      V3PC(I)=P3PC(I)/ZM3G
      V3NC(I)=P3NC(I)/ZM3G
      PU3PC(I)=V3PC(I)*ZMU3G
      PU3NC(I)=V3NC(I)*ZMU3G
   30  RETURN
      END
```

AL MEMORY REQUIREMENTS 002AFC BYTES

```
      SUBROUTINE J2JL
      COMMON R2N(51),S2N(51),U2N(51),ZMU1G,ZMU2G,ZMU3G,ZKZI,DD(51),ZK1,
     1D1,P11,DELTA1,SQP3P(51),SQP3N(51),Q12(51),Q1(51),Q2(51),Q3(51),
     2Q4(51),Q5(51),Q6(51),Q7(51),Q8(51),Q9(51),P2C3P(51),P2C3N(51),
     3Q10(51),Q11(51),PU1C(51),V3NC(51),R2P(51),S2P(51),U2P(51),J2JLP(51
     4),C2(51),C1P(51),C1N(51),C3P(51),C3N(51),C1,C4,C3,F1(51),G1(51),
     5F2P(51),F2N(51),G2P(51),G2N(51),X1(51),X2(51),X3(51),X4(51),X5(51)
     6,X6(51),X7(51),X8(51),X9(51),X10(51),ZMOG,PU2PC(51)
     7,F3P(51),F3N(51),G3P(51),G3N(51)
      COMMON T1(51),ZMO,ZMT,ZM1,ZM2,ZM3,EX,EC,PC,ROOT(51),P1(51),AG1R,AG
     12R,P2P(51),P2N(51),P3P(51),P3N(51),ZM1G,ZM2G,ZM3G,ZMGOT,TO,T2P(51)
     2,T2N(51),T3P(51),T3N(51),VCM,ZMG,P1C3P(51),P2PC(51),P1C3N(51),P2NC
     3(51),P1C(51),E11,AB,Z,PI,RO,A1,XMU,EI13N(51),ERGMEV,HBAR,E3N(51),
     4DELT(100),PU2NC(51),VC,PUO,ELAB(51),THOX(51),J2JLN(51),CC,THO(51),
     5P(51),PD(51),DEL(51),DELTR(51),AG,    ZM13,ZM23,ZM12, EI23(51),
     6EI13P(51),EI12P(51),EI12N(51),E1(51),E2P(51),E2N(51),E3P(51),
     7AG1D,AG2D,AG3RP(51),AG3RN(51),AG1RC(51),AG2RPC(51),AG2RNC(51),
     8AG3DP(51),AG3DN(51),BASE3P(51),BASE3N(51),BPHI3P(51),BPHI3N(51),
     9AG3RPC(51),AG3RNC(51),IIN,IN,I
      DOUBLE PRECISION Q22,R2P,S2P,ZMC,ZMT,E,
     1ZM1,ZM2,ZM3,EX,EO,PC,ROOT,P1,AG1R,AG2R,P2P,P2N,P3P,P3N,ZM1G,ZM2G,
     2ZM3G,ZMGOT,TO,T2P,T2N,T3P,T3N,VCM,ZMG,P1C3P,P2PC,P1C3N,P2NC,P1C,
     3Z,PI,RO,A1,E11, XMU,EI13N,ERGMEV,HBAR,DELT,PU2NC,VO,PUO,ELAB,THOX,
     4J2JLN,CC,THO,P,PD,DEL,DELTR,AG,ZM13,ZM23,ZM12,EI23,EI13P,EI12P,T1,
     5EI12N,AB,E1,E2P,E2N,E3P,E3N,U2P,J2JLP,
     6R2N,S2N,U2N,ZMU1G,ZMU2G,ZMU3G,ZKZI,DD,ZK1,D1,P11,DELTA1
      DOUBLE PRECISION SQP3P,SQP3N,Q12,Q1,Q2,Q3,Q4,Q5,Q6,Q7,Q8,Q9,P2C3P,
     1P2C3N,Q10,Q11,PU1C,V3NC,C2,C1P,C1N,C3P,C3N,X1,X2,X3,X4,X5,X6,X7,
     2X8,X9,X10,C1,C4,C3,F1,G1,F2P,F2N,G2P,G2N,ZMOG
     3,F3P,F3N,G3P,G3N ,PU2PC
      IF (ROOT(I))40,41,41
   41 Q22=ZMG/ZM2G
      R2P(I)=(P1(I)*Z/P1C3P(I))*((P2P(I)*Z)**2/P2PC(I))
      R2N(I)=(P1(I)*Z/P1C3N(I))*((P2N(I)*Z)**2/P2NC(I))
      S2P(I)=(((ZM2G+ZM3G)/ZM2G)*P2PC(I)+P1C(I)*DCOS(DBLE(AG1RC(I)+AG2RP
     1C(I))))/((ZM1G/(ZM1G+ZM3G))*P2PC(I)+P1C(I)*DCOS(DBLE(AG1RC(I)+AG2R
     2PC(I))))
      S2N(I)=(((ZM2G+ZM3G)/ZM2G)*P2NC(I)+P1C(I)*DCOS(DBLE(AG1RC(I)+AG2RN
     1C(I))))/((ZM1G/(ZM1G+ZM3G))*P2NC(I)+P1C(I)*DCOS(DBLE(AG1RC(I)+AG2R
     2NC(I))))
      U2P(I)=1.0D0/((((ZM2G+ZM3G)/ZM2G)*P2P(I)+P1(I)*DCOS(AG1R+AG2R)-PO*
     1DCOS(AG2R))*Z)
      U2N(I)=1.0D0/((((ZM2G+ZM3G)/ZM2G)*P2N(I)+P1(I)*DCOS(AG1R+AG2R)-PO*
     1DCOS(AG2R))*Z)
      J2JLP(I)=   R2P(I)*S2P(I)*U2P(I)*Q22
      J2JLN(I)=   R2N(I)*S2N(I)*U2N(I)*Q22
   40 RETURN
      END
```

AL MEMORY REQUIREMENTS 00051A BYTES

```
      SUBROUTINE DOSPN
      COMMON R2N(51),S2N(51),U2N(51),ZMU1G,ZMU2G,ZMU3G,ZKZI,DD(51),ZK1,
     1D1,P11,DELTA1,SQP3P(51),SQP3N(51),Q12(51),Q1(51),Q2(51),Q3(51),
     2Q4(51),Q5(51),Q6(51),Q7(51),Q8(51),Q9(51),P2C3P(51),P2C3N(51),
     3Q10(51),Q11(51),PU1C(51),V3NC(51),R2P(51),S2P(51),U2P(51),J2JLP(51
     4),C2(51),C1P(51),C1N(51),C3P(51),C3N(51),C1,C4,C3,F1(51),G1(51),
     5F2P(51),F2N(51),G2P(51),G2N(51),X1(51),X2(51),X3(51),X4(51),X5(51)
     6,X6(51),X7(51),X8(51),X9(51),X10(51),ZMOG,PU2PC(51)
     7,F3P(51),F3N(51),G3P(51),G3N(51)
      COMMON T1(51),ZMO,ZMT,ZM1,ZM2,ZM3,EX,EO,PO,ROOT(51),P1(51),AG1R,AG
     12R,P2P(51),P2N(51),P3P(51),P3N(51),ZM1G,ZM2G,ZM3G,ZMGOT,TO,T2P(51)
     2,T2N(51),T3P(51),T3N(51),VCM,ZMG,P1C3P(51),P2PC(51),P1C3N(51),P2NC
     3(51),P1C(51),E11,AB,Z,PI,RO,A1,XMU,E(51)     ,ERGMEV,HBAR,E3N(51),
     4DELT(100),PU2NC(51),VO,PUO,ELAB(51),THOX(51),J2JLN(51),CC,THO(51),
     5P(51),PD(51),DEL(51),DELTR(51),AG,     ZM13,ZM23,ZM12, EI23(51),
     6EI13P(51),EI12P(51),EI12N(51),E1(51),E2P(51),E2N(51),E3P(51),
     7AG1D,AG2D,AG3RP(51),AG3RN(51),AG1RC(51),AG2RPC(51),AG2RNC(51),
     8AG3DP(51),AG3DN(51),BASE3P(51),BASE3N(51),BPHI3P(51),BPHI3N(51),
     9AG3RPC(51),AG3RNC(51),IIN,IN,I
      DOUBLE PRECISION ZK1,D1,DELTA1,P11,ZKZI,CC,     T1,ZMO,ZMT,ZM1,ZM2
     1,ZM3,EX,EO,PO,ROOT,P1,AG1R,AG2R,P2P,P2N,P3P,P3N,ZM1G,ZM2G,ZM3G,
     2ZMGOT,TO,T2P,T2N,T3P,T3N,VCM,ZMG,P1C3P,P2PC,P1C3N,P2NC,P1C,
     3Z,PI,RO,A1,E11, XMU,EI13N,ERGMEV,HBAR,DELT,PU2NC,VO,PUO,ELAB,THOX,
     4J2JLN,CC,THO,P,PD,DEL,DELTR,AB,ZM13,ZM23,ZM12,EI23,EI13P,EI12N,
     5EI12P,ZK(51),     E1,E2P,E2N,E3P,E3N,E,AG,DD,
     6R2N,S2N,U2N,ZMU1G,ZMU2G,ZMU3G,ZMCG
      DOUBLE PRECISION SQP3P,SQP3N,Q12,Q11,Q1,Q2,Q3,Q4,Q5,Q6,Q7,Q8,Q9,
     1P2C3P,P2C3N,Q10,PU1C,V3NC,R2P,S2P,U2P,J2JLP,C2,C1P,C1N,C3P,C3N
     2,X1,X2,X3,X4,X5,X6,X7,X8,X9,X10,C1,C4,C3,F1,G1,F2P,F2N,G2P,G2N
     3,F3P,F3N,G3P,G3N,PU2PC
      ZK1=(DSQRT(2.0D0*XMU*E11))/HBAR
      D1=-1.0D0/AB+5.0D-1*RO*ZK1**2
        DELTA1=DATAN(ZK1/D1)
      P11=ZK1*A1
      ZKZI=DSQRT(2.0D0/A1)*DSIN(DELTA1+P11)
      CC=(2.0D0/PI)*(XMU/HBAR)*(A1/ZKZI)*(1.0D0/HBAR)*(1.0D0/ZKZI)
      IF (ROOT(I))50,52,52
   52 IF(E(I)-0.8D1)51,53,53
   51 ZK(I)=(DSQRT(2.0D0*XMU*E(I)*ERGMEV))/HBAR
      DD(I)=-1.0D0/AB+5.0D-1*RO*ZK(I)**2
      DELTR(I)=DATAN(ZK(I)/DD(I))
      P(I)=ZK(I)*A1
      THOX(I)=CC*(DSIN(DELTR(I)+P(I)))**2/P(I)
      THO(I)=THOX(I)*ERGMEV
      ELAB(I)=2.0D0*E(I)
      DEL(I)=DELTR(I)*5.72957795D1
      PD(I)=P(I)*5.72957795D1
      GO TO 50
   53 ZK(I)=(DSQRT(2.0D0*XMU*E(I)*ERGMEV))/HBAR
      P(I)=ZK(I)*A1
      J=E(I)
      IF(SNGL(E(I))-FLOAT(J)-0.5)54,55,55
   54 KK=E(I)
      GO TO 56
```

```
     55 KK=E(I)
        KK=KK+1
     56 DELTR(I)=DELT(KK)*1.74522D-2
        DEL(I)=DELT(KK)
        THOX(I)=CC*(DSIN(DELTR(I)+P(I)))**2/P(I)
        THO(I)=THOX(I)*ERGMEV
        ELAB(I)=2.0D0*E(I)
        PD(I)=P(I)*5.72957795D1
     50 RETURN
        END
```

AL MEMORY REQUIREMENTS 000798 BYTES

REFERENCES

AGK-66	Nucl. Phys. 81 (1966) 305	P.A. Assimakopoulos, N.H.Gangas, S. Kossionides
AW-52	Phys. Rev. 85(1952) 686	J. Ashkin, G.C. Wick
B-56	Phys. Rev. 101(1956) 796	M. M. Block
B-66	Nucl. Instr. & Meth. 42 (1966) 211	R. E. Bell
BA-67	Nucl. Phys. B1(1967) 49	E. Bar-auraham, R.Fox, Y. Porath, G.Adam, G. Frieder
Be-49	Phys. Rev. 76(1949) 38	H.A. Bethe
BHLP-60	Phys. Rev. 120(1960) 2227	G.Breit, M.H. Hull,Jr., K.E. Lassila, K.D. Pyatt
BKF-65	Rev. Mod. Phys. 37(1965) 528	S.M.Bunch, C.C.Kim, H.H.Forster
BO-58	Nucl. Phys. 5(1958) 669	T.H. Berin, G.E. Owen
Br-67	Rev. Mod. Phys. 39(1967)560	G. Breit
BW-68	Can. J. Phys.46(1968) 233	E.W.Blackmore, J.B. Warren
C-51	Phys. Rev. 84(1951) 710	G. F. Chew
C-62	Nucl. Inst. & Meth. 15(1962)268	A. M. Cormack
Ca-65	Rev. Mod. Phys. 37(1965) 531	R. F. Carlson
CG-52	Phys. Rev. 87 (1952) 778	G.F. Chew, M.L. Goldberger
Ch-50	Phys. Rev. 80 (1950)196	G.F. Chew

CL-59	Phys. Rev. 113(1959)1640	G.F. Chew, F.E. Low
Cr-66	Private Communication	J.E. Crawford
CS-57	Phys. Rev. 105(1957) 288	O. Chamberlain, E. Segre, R.D. Tripp, C. Wiegand, T. Ypsilantis
CS-59	Phys. Rev. 113(1959)587	L. Cranberg, R. K. Smith
CW-52	Phys. Rev. 85(1952) 636	G.F.Chew, G.C. Wick
DKZ-64	Phys. Rev. 135(1964) B61	P.F. Donovan, J.V.Kane, Č.Zupančič, C.P.Baker, J.F. Mollenauer
EJ-54	Phys.Rev. 96(1954) 911	F.S. Eby, W.K. Jentschke
F-65	Ph.D. thesis, McGill University (1965)	J.P. Felvinci
Fa-60	J. Exp.Theor. Phys. (USSR) 12 (1960) 1014	L.D. Faddeev
FG-54	Phys.Rev. 93(1954) 463	R.M. Frank, J.L. Gammel
G-67	Ph.D. thesis, McGill University (1967)	N.P. Goldstein
GB-51	Phys. Rev. 81 (1951)761	R.L. Gluckstern, H.A. Bethe
GK-64	Nucl. Phys. 54(1964) 56	R.J. Griffiths, K.M. Knight
GV-67	Nucl.Instr. & Meth. 49(1967)55	R.B. Galloway, D.G. Vass
HLR-61	Phys.Rev. 122(1961) 1606	M.H. Hull,Jr., K.E. Lassila, H.M. Ruppel, F.A. McDonald, G. Breit.

HM-58	Phys. Rev. 111(1958) 593	W.Heckrotte, M. MacGregor
Ho-67	Rev. Mod. Phys. 39(1967)548	N. Hoshizaki
KLJ-67	Rev. Mod. Phys. 39(1967). 571	Y.M. Kazarinov, F. Lehar, Z. Janout
KP-60	J. Exp. Theor. Phys. (USSR) 11 (1960) 1123	V.V. Komarov, A.W. Popova
KP-65	Nucl. Phys. 69(1965)253	V.V.Komarov, A.W. Popova
KS-60	J. Phys. Soc. Japan 15 (1960) 748	S.Kikuchi, J.Sanada, Shigeki, Suwa, I.Hayashi, K. Nisimura K. Fukuraga
KWC-61	Ann. of Phys. 15(1961) 193	A.F. Kuckes, R. Wilson, P.F. Cooper
Lo-64	Phys. Rev. 135(1964) B1225	C. Lovelace
LS-50	Phys. Rev. 79(1950) 469	B.A. Lippmann, J. Schwinger
M-65	Nucl.Instr.& Meth. 34 (1965) 353	D.F. Measday
Ma-65	Ph.D. thesis, McGill University (1965)	S.K. Mark
NB-65	"α,β,γ Ray Spectroscopy" Vol.1 (North Holland Publishing Co. 1965)	J.H. Beiler, P.R. Bell (K. Siegbahn)
O-64	Ph.D. Thesis, McGill University (1964)	P. Onno
OH-65	Nucl. Instr. & Meth. 37(1965)240	G.G. Ohlsen

P-67	Ph.D. Thesis, McGill University (1967)	P.M. Portner
PC-58	Ann. Of Phys. 5(1958) 299	J.B. Palmieri, A.M.Cormack, N.F. Ra sey, R. Wilson
Pe-67	Rev.Mod.Phys. 39(1967)550	J.D. Perring
PGB-60	Nucl.Phys. 21(1960) 327	G.C.Phillips, R.A. Griffy, L.C. Biedenharn
PGB-67	Zeit. für Phy. 205(1967) 420	G.C.Phillips, R.A. Griffy, L.C. Biedenharn
RM-54	UCRL-2301 "Range-Energy Tables", March, 1954.	M.Rich, R. Madey
S-65	Ph.D. thesis, Rice University (1965)	W.D. Simpson
SJP-67	Nucl.Phys. A103(1967) 97	W.D.Simpson, W.R. Jackson G.C. Phillips
SVR-66	Phys.Lett. 23(1966)358	I.Slauss, J.W. Verba, J.R. Richardson, L.S. August, E.L. Petersen
TW-61	Phys.Rev. 124(1961) 890	J.H. Tinlot, R.E. Warner
TWB-60	Nucl.Phys. 16(1960) 320	A.E. Taylor, E.Wood, L.Bird
VK-60	J.Exp. Theor.Phys. (USSR)11 (1960) 1251	N.A.Vlasov, S.P. Kalinin, B.V.Rybakov, V.A. Sidorov
W-63	Phys.Rev. 132(1963) 2621	R.E. Warner
W-66	Nucl.Inst.&Meth. 41(1966) 122	H.Willmes

Wa-48	Phys.Rev. 73(1948) 986	T.Y.Wu, J.Ashkin
WAG-59	Phys.Rev. 116(1959) 164	C.Wong, J.D. Anderson, C.C. Gardner, J.W. McClure, M.P. Nakada
WB-68	Nucl.Phys. A114(1968)377	M.R.Wigan, R.A.Bell, P.J.Martin O.N.Jarvis, J.P.Scanlon
WY-63	"Methods of Experimental Physics" Vol.5, Part B. (Academic Press, 1963)	R.M. Sternheimer (C.L. Yuan, C.S. Wu)